First-Principle Studies of Plasma-Catalyst Interactions for Greenhouse Gas Conversion

Amin Jafarzadeh

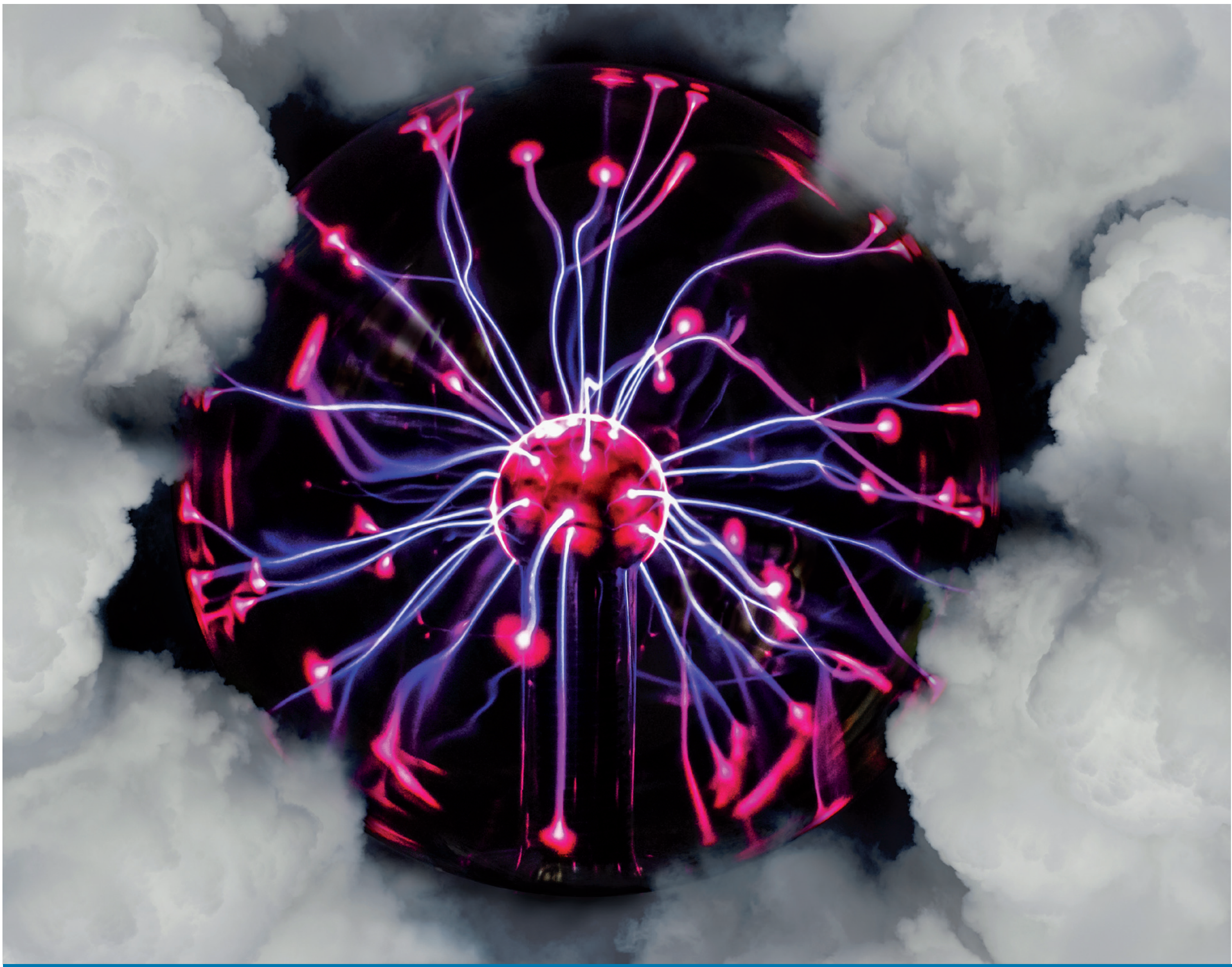

Supervisors **Prof. Dr. Erik Neyts | Prof. Dr. Annemie Bogaerts**

Thesis submitted to the University of Antwerp for the Degree of Doctor of Philosophy in Science
Faculty of Science | Department of Chemistry | Antwerp, 2020

University
of Antwerp

Universiteit Antwerpen

Faculteit Wetenschappen
Departement Chemie

First-Principle Studies of Plasma-Catalyst Interactions for Greenhouse Gas Conversion

Proefschrift voorgelegd tot het behalen van de graad van doctor in de wetenschappen aan de Universiteit Antwerpen te verdedigen door

Amin Jafarzadeh

Promoters:
Prof. dr. Erik Neyts
Prof. dr. Annemie Bogaerts

Antwerpen 2020

Contents

Acknowledgments

Now that my journey as a PhD student has come to an end, I want to thank everyone who has helped me in every possible way to walk along this path.

First of all, I would like to express my highest gratitude to my supervisors, Prof. Erik Neyts and Prof. Annemie Bogaerts for their consistent support and guidance during my PhD. Erik and Annemie, thank you for believing in me and giving me the opportunity to learn and challenge myself with atomistic simulations. I whole-heartedly appreciate your accurate, swift, and encouraging advice towards the success of this study. I have always been inspired by your ideas in research and amiable personalities in my social life. *Heel erg bedankt! Ik hoop dat we in de toekomst met elkaar kunnen blijven samenwerken.*

I am so thankful to Prof. Marcella Iannuzzi and Prof. Jürg Hütter for giving me the opportunity to visit their amazing research group at the University of Zürich. I would like to recognize the kind considerations that I received from Marcella and Giacomo during our scientific discussions. It was also a great honor for me to give a seminar talk in their group presenting my work.

Special thanks go to Luc, Karel, Fabiana, and Ingrid for their invaluable administrative and technical support during my study. Karel helped me a lot upgrading my laptop for the research stay, and I do admire his friendly, knowledgeable, and unpretentious character.

I also want to thank my colleagues in the PLASAMNT research group: Quan-Zhi (for being a good friend as well), Antonin, Neda, Mozhgan, Kristof (for the scientific discussions we had), Samira, Milica, Yannick(s), Georgi, Charlotta, Yanhui & Zhaolun (for the collaborations we started together) and members of our *"Lunch Squad"*: James, Fatme, Kevin, Hamid, Mohammad, and Omar. I especially thank my office mates, Stefan and Mehdi in B2.31 and Maryam, Inne, and Marleen in B2.05. I wish to show my gratitude for Maryam's kind and friendly assistance, especially at the start of my PhD (renting a flat for me prior to my arrival, providing me with the "survival package" for the first weeks, and being an Antwerp encyclopedia!).

My five-week stay in Zürich was fabulous, thanks to the great people I met and accompanied by there. I would like to thank Yasmine, Giacomo, and Vladimir for the interesting discussions we had during the coffee breaks. I also appreciate Augustin and Fabian's great hospitality and making the best Fondue that I have ever had!

I am indebted to the CalcUA HPC core facility at the University of Antwerp as a part of the Flemish Supercomputer Centrum (VSC). I want to thank Kurt, Stefan, and Franky for their great job maintaining Hopper and Leibniz and providing technical assistance.

I wish to express my sincere gratitude to Dr. Korosh Aghayar, the professor of the *"Statistical Mechanics"* and the *"Quantum Mechanics II"* courses during my bachelor studies. Korosh, you introduced me to some of the most fascinating aspects of nature, and you taught me how to enjoy studying physics. You were the best teacher that I could have wished for.

Along with these work-related appreciation notes, I want to express my deep and sincere appreciation to my parents for their non-stop and unparalleled love, and support. I am also grateful to my sister for always being there for me as a friend. My mother has always been a symbol of resilience in the face of difficulties. Her strong, generous, and compassionate character has always been a source of inspiration for the people around her. She never had the chance to go to college, but she persistently did whatever it took to support and encourage me to chase my dreams. I am eternally grateful for having her as my mother.

Further, I'm thankful to my grandparents (especially my grandpa, Aa'jan!), and Nahid (my aunt/friend) for their belief in me and for their support and encouragements.

My gratitude also goes to my friends from my personal life: Mohammad & Fatemeh for the best trips that we went on together and also for providing us a second home in Lausanne; Majid, Maryam, Somaie, Banafsheh, Nariman, Saeid, Sanaz, and Saman for the so many relaxing hours that we spent together; my chess mate, Sander, for the games that we played against each other and also for the everlasting (pseudo)philosophical debates that we had!

Finally, I would like to thank my wife for everything. Ati, during the last 6 years, you have been my best friend. You have brought color to my life by sprinkling it with happiness and your good vibes. I'm so lucky to have you in my life!

Amin
Antwerp, December 2020

List of Figures

List of Tables

Chapter 1

Introduction

“The Earth is a fine place and worth fighting for.”

Ernest Hemingway

1.1 Climate change and the greenhouse effect

“Climate Change”, broadly interpreted, is often used to refer to the long-term variations in weather patterns on the regional or global level with large scale and often long-lasting consequences. There have been continuous fluctuations in the earth’s overall temperature throughout history, mostly attributed to small variations in its orbit, subtly changing the amount of energy received from the sun. During the last 700 millennia, the earth has experienced several cycles of glacial advance and retreat and since the agricultural revolution and human civilization it has entered to a modern climate era [1].

The start of discovering the climate change dates to almost 200 years ago. The “greenhouse effect” concept was first introduced by the French physicist Joseph Fourier back in 1824. He was the first to realize that there might be a link between certain atmospheric gases and the earth’s overall temperature. A few decades later, the Irish physicist John Tyndall investigating the Alpine glaciers, recognized the impact of greenhouse gases on the earth’s climate and hypothesized that small variations in the atmospheric composition could lead to changes in climate patterns. In 1896, Swedish scientist Svante Arrhenius published a paper [2] in which he predicted that the variations in atmospheric CO_2 levels could substantially change the earth’s surface temperature via the greenhouse effect [1]. Figure 1.1 shows the pioneers of climate change research.

Figure 1.1: Pioneers of climate change research.

From the earth's warming trend over the past century shown in Figure 1.2, it is clear that there is a substantial increase in the earth's average temperature during the last four decades. This rise in global temperature coincides with the increase in the greenhouse gas concentration levels due to the unprecedented growth in industrialization and the human population [3].

Greenhouse gases, like CO_2, CH_4, N_2O, chlorofluorocarbons (CFCs), and hydro-chlorofluorocarbons (HCFCs), are known to trap heat in the atmosphere and subsequently increase the earth's average temperature. More than 96% of the actively publishing climate scientists believe that increased levels of greenhouse gases – which result from human activity – are highly likely to be the main reason for the unusual climate variations during the past century [1, 3–7].

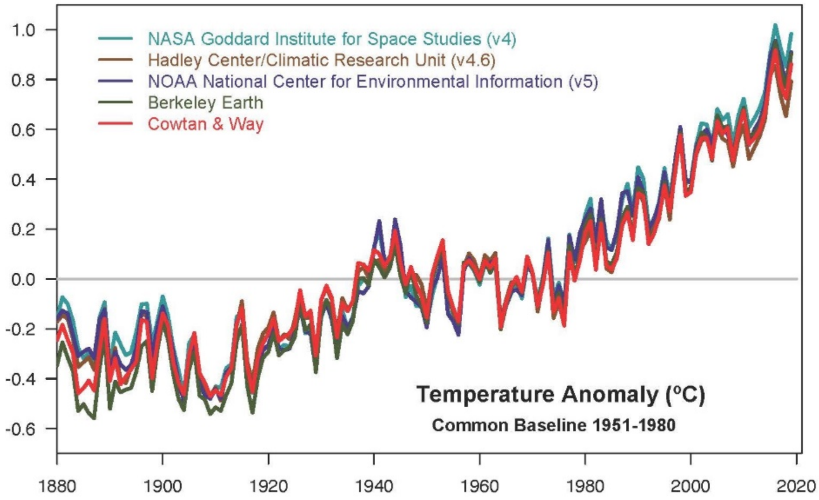

Figure 1.2: Temperature data showing the earth's warming trend in the past few decades. Image credit: NASA/NOAA [8].

Anthropogenic greenhouse gas emissions have several detrimental effects on the planet. The rise of sea levels, melting of ice sheets, and glacial retreat are only some of the evidence of the rapid changes in climate patterns during the last 40 years [9, 10].

1.2 Conversion of greenhouse gases

Due to the far-reaching consequences of greenhouse gas emissions, the need for finding more efficient and novel ways to reduce their release into the atmosphere is felt more than ever. Among the above-mentioned greenhouse gases, CO_2 and CH_4 emissions resulting from fossil fuel consumption and the burning of natural gas are the major contributors to climate change. As reported by the intergovernmental panel on climate change (IPCC) [11] and shown in Figure 1.3, CO_2 and CH_4 contribute to more than 80% of the global greenhouse gas emissions.

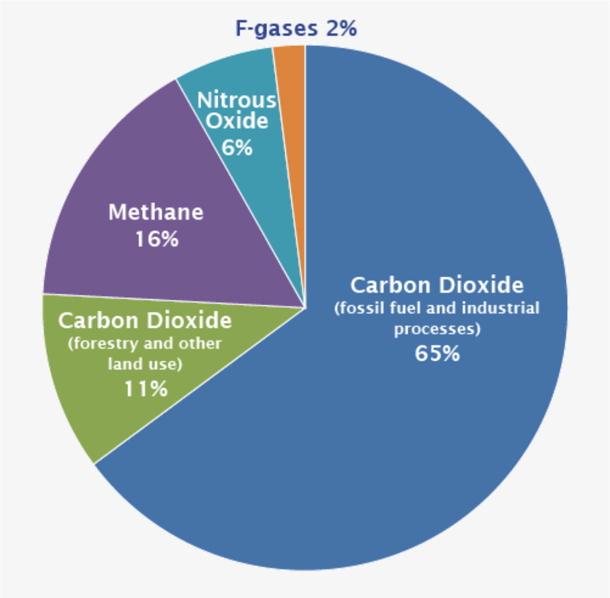

Figure 1.3: Global greenhouse gas emissions- Adapted from [11, 12].

Methane (CH_4) is the major component of natural gas, which consists of various hydrocarbons. Compared to CO_2, CH_4 is 84 times more potent in heat-trapping over the first two decades after release and 28 times more potent after a century [13]. Only 1% of the extracted natural gas is chemically utilized, and the rest is being burned [14]. The oxidation of CH_4 to CO_2 proceeds via a thermodynamically favorable reaction:

$$CH_4\,(g) + 2O_2\,(g) \rightarrow CO_2\,(g) + 2H_2O\,(l) \quad \Delta H_r^0 = -803\ \text{kJ mol}^{-1} \tag{1.1}$$

Efficient conversion of CO_2 and CH_4 to value-added chemicals, such as hydrocarbons and alcohols, would not only facilitate a sustainable way to tackle environmental issues caused by global industrialization but also will help to revamp renewable energy resources [15–17].

1.2.1 Steam and dry reforming of methane

Since CH_4 is a rather inert molecule, there is normally a need for a co-reactant in its conversion process. Steam and dry reforming of CH_4 to syngas, i.e., a mixture of hydrogen (H_2) and carbon monoxide (CO), are common approaches employed to utilize greenhouse gases.

Steam reforming of methane (SRM) is a highly endothermic reaction in which, in the presence of a catalyst, methane reacts with high-temperature steam (700 °C – 1,000 °C) under a pressure of 3-25 bar to produce syngas:

$$\mathrm{CH_4\,(g) + H_2O\,(g) \rightarrow CO\,(g) + 3H_2\,(g) \quad \Delta H^0_{298} = 206\ kJ\ mol^{-1}} \tag{1.2}$$

SRM is typically combined with the Water Gas Shift (WGS) reaction to improve the hydrogen production cycle by adjusting the H_2/CO ratio.

$$\mathrm{CO\,(g) + H_2O\,(g) \rightarrow CO_2\,(g) + H_2\,(g) \quad \Delta H^0_{298} = -41\ kJ\ mol^{-1}} \tag{1.3}$$

Although the SRM reaction is economically beneficial mostly thanks to the use of nickel catalysts instead of expensive catalysts like platinum, there are some challenges such as the need for high energy input, sintering, high carbon formation, and difficulties in catalyst activity maintenance [18, 19].

By replacing water with carbon dioxide, another alternative process for the production of syngas can be achieved. This combined conversion of CH_4 and CO_2 is known as Dry (or CO_2) Reforming of Methane (DRM):

$$\mathrm{CH_4\,(g) + CO_2\,(g) \rightarrow 2CO\,(g) + 2H_2\,(g) \quad \Delta H^0_{298} = 247\ kJ\ mol^{-1}} \tag{1.4}$$

Fischer and Tropsch first studied this method in 1928, and since then, scientists and engineers have been working to adopt the approach to produce value-added chemicals from greenhouse gases. DRM has several advantages, such as the possibility of using biogas as a feedstock and providing a straightforward way to convert CO_2 for further applications [20]. On the other hand, DRM has its inherent limitations, such as coke formation and catalyst deactivation, which have prevented this approach from being employed for industrial purposes. Although there are ongoing attempts towards the use of a modified catalyst to prevent coke formation [21], which was initially also a big issue for its sibling SRM, the inability to transform the attractive profitability of DRM into practice using the traditional methods—among other reasons—has led to the growing interest for alternative reforming technologies, such as plasma catalysis [20].

1.2.2 Ammonia reforming of methane

Methane can also be used in combination with ammonia (NH_3), to form hydrogen cyanide (HCN). HCN is mainly produced via the Andrussow process [22], which is an exothermic reaction (equation 1.5) taking place at atmospheric pressures and high temperatures ($\sim 1,600$ K) employing platinum-based catalysts such as $Pt_{90}Rh_{10}$ gauzes [23]. The combustion of H_2 typically supplies the required energy to maintain the high temperature needed for this process. Generally, about 60% of the HCN yield and 60-70% NH_3 utilization can be obtained by the Andrussow process [24–27].

$$\mathrm{CH_4 + NH_3 + 1.5O_2 \rightarrow\ HCN\ + 3\,H_2O \quad \Delta H = -483\ kJ/mol} \tag{1.5}$$

The high reaction temperature in the Andrussow process usually results in the deactivation of Pt catalysts, and therefore, mixing of Pt by Rh to form a Pt-Rh alloy gauze catalyst is necessary to improve the catalyst's durability. The high temperature also results in a long time needed to feed gas heating and product cooling.

A less popular alternative for HCN formation is the BMA process (BMA; acronym for *Blausäure* (hydrogen cyanide) from *Methan* (methane) and *Ammoniak* (ammonia) in German). In contrast to the Andrussow process, the BMA process is a strongly endothermic reaction between CH_4 and NH_3 (equation 1.6). It is usually operated at atmospheric pressures and yields stoichiometric hydrogen production, which is a significant advantage compared to the Andrussow process.

$$\mathrm{CH_4 + NH_3 \rightarrow\ HCN\ + 3\,H_2 \quad \Delta H = 251\ kJ/mol} \tag{1.6}$$

The BMA process is also called Degussa process, as it was firstly exploited by the Degussa company in Wesseling [26, 27]. In industrial BMA plants, the Pt mesh catalyst is usually placed in parallel columnar reactors. The equilibrium conversion, selectivity and yield as a function of temperature obtained through thermodynamic calculations are shown in Appendix 3. (Figure A3.1). The BMA process for HCN synthesis is typically operated at a temperature of ($\sim 1,600$ K) to balance the HCN yield and cost. On the one hand, the HCN yield increases with reaction temperature, and on the other hand, the high reaction temperature also causes a higher investment of equipment, as well as energy consumption and waste of feed gas. Therefore, a significant amount of NH_3 and CH_4 is decomposed into N_2 and coke, respectively [24–27].

The industrial production of HCN from NH_3 and CH_4 via both Andrussow and BMA-Degussa processes needs commercially expensive Pt or Pt-Rh catalysts and must be operated at very high temperatures (1,600 K). In Chapter 5, we will discuss the applicability of plasma catalysis for ammonia reforming of methane at lower temperatures and using cheaper catalysts.

1.3 Plasma and plasma catalysis

A plasma is an ionized gas consisting of neutral and excited species (i.e., molecules, radicals), ions, electrons, and photons. Plasma is often called the “fourth state of matter” following the sequence of well-known states of solid, liquid, and gas. In addition to important environmental and industrial applications, plasmas make more than 99% of the mass of the visible universe [28].

Plasmas occur in many different forms, both natural and human-made. The sun, lightning, solar winds, nebulae, and flames are some of the well-known examples of the plasmas found in nature. Human-made plasmas can be formed either by increasing the gas’s temperature via heating or by applying strong electric fields for ionizing the gas molecules. Plasmas can be categorized into high-temperature and low-temperature plasmas. The plasma made from nuclear fusion, usually controlled by strong magnetic fields, is an example of hot or high-temperature plasmas. Low-temperature plasmas, depending on the gas temperature, can also be categorized into thermal and non-thermal plasmas.

Three major characteristics of plasmas [28] are:

1. The temperature and energy distribution of plasma species can be much higher in comparison to the temperatures and densities measured in traditional thermal-chemical technologies;
2. Plasmas can induce a high concentration of reactive species; and
3. Plasmas can provide a thermodynamically non-equilibrium environment.

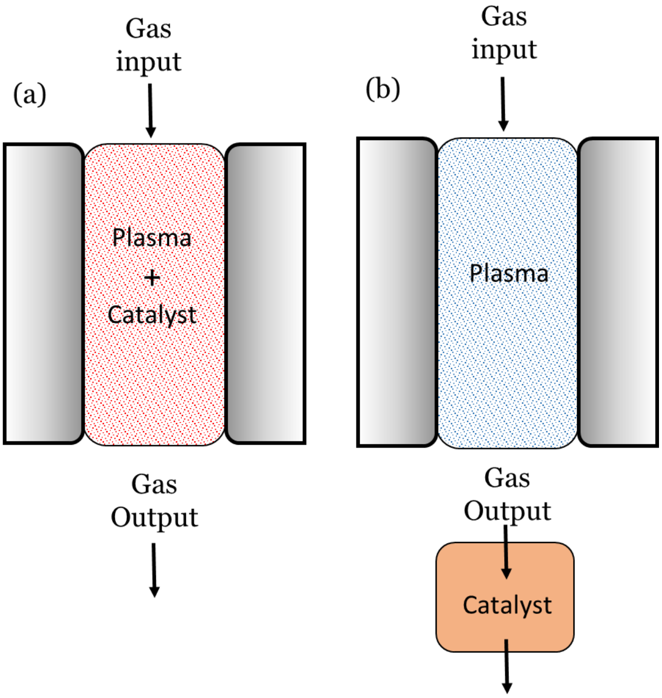

Figure 1.4: Schematic diagram of two major plasma catalysis arrangements: single-stage configuration (a) and two-stage configuration (b).

These properties make the plasma an attractive option for chemical and other related industries [28]. The high reactivity in the plasma environment makes it possible for chemical reactions to proceed at lower temperatures and reduced energy costs. This high reactivity typically comes at a price of low selectivity, which can in principle be addressed using plasma in combination with a proper catalyst [29].

In thermal plasmas, all the species are almost at the same temperature ($\sim 10,000$ K or higher), and the plasma is at the equilibrium temperature. In contrast, when there is an imbalance between the temperatures of electrons and heavy particles, like ions, atoms, or radicals, the plasma is labeled as a non-thermal plasma. This non-equilibrium situation is typically induced by the high mobility of the electrons (resulting from their much smaller mass compared to ions or other heavy particles). Non-thermal plasmas can be generated by several setups, such as dielectric barrier discharge (DBD) reactors, microwave induced plasma tubes, and gliding arcs.

In general, plasma catalysis, also known as plasma-assisted catalysis, refers to any combination of a gaseous discharge or plasma with a material that has catalytic properties. A single-stage plasma catalysis setup is formed when the catalyst is put into direct contact with the plasma environment. Alternatively, a catalyst can be added after the plasma region to make a two-stage plasma catalysis set up (Figure 1.4).

This combination of plasma and catalyst can sometimes lead to improved outcomes that are not achievable by employing only plasma or only catalysis [30]. For instance, reaction promotion in catalytic removal of NO_x [31], higher CO_2 conversion [32], a decrease in the energy barrier for dry reforming of methane (DRM) [33], and increased treatment efficiency on Escherichia coli cells in aqueous media [34] have been reported as a result of synergistic effects in plasma catalysis. Although plasma catalysis holds promise for many environmental [35–40] and industrial [41, 42] applications, the underlying reasons for synergy in plasma catalysis are not yet fully understood.

1.4 Interactions between plasma and catalyst

Combining the (potentially) high selectivity of a catalyst with the plasma's high reactivity into a plasma-catalytic system leads to reciprocal interactions between plasma species and catalyst [43]. Understanding the underlying complex mechanism for these interactions can help to determine the direction of chemical reactions taking place between species adsorbed on the surface of the catalyst with both pre-adsorbed species and species in the gas-phase. As stated by Whitehead [30], *"We could modify a reactive plasma system by the addition of a catalyst and observe any effects that the catalyst produces or we could take a catalytic process and subject the gas (and also the catalyst) to the effect of plasma. We understand each baseline system with a reasonable degree of certainty but the mutual interaction of plasma upon catalysis and vice versa is complex and varied and has still much that is not understood."*

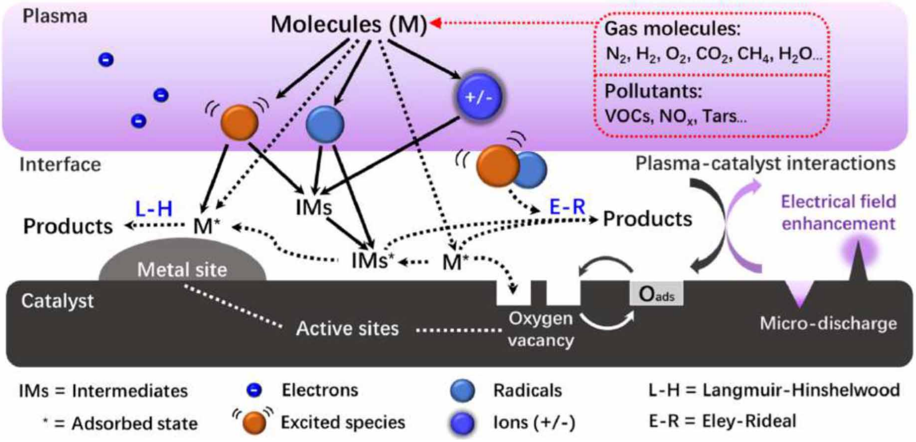

Figure 1.5: Complex network of reciprocal interactions between plasma species and catalyst surface in plasma catalysis. Adapted from [44].

Interactions between catalyst and plasma are quite different from the simpler gas-surface interactions. Depending on the density, flux, and energy of reactive species present in the plasma environment, various processes in a plasma-catalytic system can be induced [45]. Some of these processes that will be later discussed in this thesis are briefly introduced below.

1.4.1 Surface charging and charge transfer

Surface charging happens in plasma catalysis, mostly because of the high mobility of the electrons. On the other hand, depending on the direction of the applied electric field, the catalyst surface can be bombarded with ions. The presence of plasma-induced excess electrons can profoundly impact the deposition of size-selected nanoclusters and charge transfer patterns between the clusters and the supporting materials. Surface charging can also lead to modification of the adsorption properties of the impinging molecules. More details on the surface charging effect are provided in Chapter 3.

1.4.2 Electric field and catalyst surface area enhancement

Addition of a catalyst into a plasma environment is often accomplished by inserting dielectric beads or pellets into the discharge area [46, 47]. The morphology and charge accumulation on the catalyst surface can alter the electric field and electron energy distribution [48]. Reciprocally, the external electric field can change the catalyst surface morphology, altering the catalytic reaction. By disentangling the effect of each parameter and their direct relevance to the surface chemistry in plasma catalysis, fundamental insights into charge-based phenomena, as found in electrochemical systems, can be achieved. A detailed study on the combined effect of surface morphology, plasma-induced surface charging, and the external electric field on activation of CO_2 is reported in Chapter 4.

1.4.3 Modification of gas-phase reactants

In a non-plasma state, gas-phase radicals and molecular species are generally in their ground state electronical and vibrational energy levels. Therefore, their interaction with the catalyst surface is very different from the interaction of electronically or vibrationally excited species produced in the plasma. Both experimental and theoretical findings demonstrated that vibrational excitation could lower the reaction barrier for some reactions [49–57]. Furthermore, formation of reactive species in the plasma can change the reaction mechanisms and consequently, the whole reaction network in plasma catalysis. This complex interdependence interaction between plasma and catalyst is schematically represented in Figure 1.5.

1.5 Aim of this work

The interest in utilizing plasma catalysis for environmental purposes continues to grow. Since a plasma-catalytic reaction can benefit both from the reactivity of the plasma and the high product selectivity induced by the catalyst, it is important to understand the plasma-catalyst interaction at a fundamental level in order to maximize the synergistic effects in practical experiments. Because of the highly complex network of processes happening simultaneously, revealing the entire mechanism is not straightforward. Utilizing computer simulations, we can study each factor separately and obtain detailed information about their effect on the whole reaction network. As part of an integrated multi-scale simulation scheme for understanding plasma catalysis, atomic scale calculations provide valuable insight into the interactions and subsequent changes in the catalyst electronic structure and the reactivity of atoms, molecules, and radical species present in the plasma. In that context, this thesis aims to provide answers to the following questions:

- How can we model plasma-induced surface charging and its impact on the adsorption of size selected catalytic nanoclusters on a support material? (Chapter 3)
- What is the effect of “surface charging” on the activation of molecules, such as CO_2 adsorbed on supported metal clusters? (Chapter 3)
- How can we model the effect of an externally applied electric field in plasma-catalysis? (Chapter 4)
- How does the electric field change the activation and chemisorption properties of CO_2 molecule adsorbed on the Cu surfaces when combined with the effects of excess electrons and surface morphology? (Chapter 4)

- How do plasma-generated radicals affect the plasma-catalytic reactions, especially for the case of ammonia reforming of methane for HCN production? (Chapter 5)
- How can we simulate the reactivity of vibrationally excited species in a plasma-catalytic non-equilibrium environment? (Chapter 6)

The answers to these questions will help to adjust and optimize plasma-catalytic processes towards revamping renewable energy resources and mitigating environmental issues arising from greenhouse gas production.

Chapter 2

Theoretical Models

"I consider that I understand an equation when I can predict the properties of its solutions, without actually solving it."

P. A. M. Dirac

In this chapter, the fundamentals of the first-principle calculations needed for describing the properties of materials and the interactions taking place at the atomic scale are briefly explained. Also, methodologies for treating excess electrons, external electric fields, and reactivity of plasma-generated radicals are discussed.

2.1 The many-body problem

In order to accurately describe the behavior of a system consisting of many electrons and nuclei, we have to deal with the many-body Schrödinger equation [58] to be able to determine the corresponding wavefunction of the system. By setting the electron spin aside for the moment and considering the non-relativistic Hamiltonian of the system in atomic units ($\hbar = m_e = e = 1$) we have:

$$\begin{aligned}\Bigg[&-\sum_i \frac{\nabla_i^2}{2} - \sum_I \frac{\nabla_I^2}{2M_I} - \sum_{i,I} \frac{Z_I}{|\vec{r}_i - \vec{R}_I|} + \frac{1}{2}\sum_{i\neq j} \frac{1}{|\vec{r}_i - \vec{r}_j|} \\ &+ \frac{1}{2}\sum_{I\neq J} \frac{Z_I Z_J}{|\vec{R}_I - \vec{R}_J|}\Bigg] \Psi(\vec{r}, \vec{R}) = E\Psi(\vec{r}, \vec{R})\end{aligned} \tag{2.1}$$

In which,

$$-\sum_i \frac{\nabla_i^2}{2} - \sum_I \frac{\nabla_I^2}{2M_I} \tag{2.2}$$

is the kinetic energy of electrons i of mass $m_e = 1$ and nuclei I of mass M_I,

$$-\sum_{i,I} \frac{Z_I}{|\vec{r}_i - \vec{R}_I|} \tag{2.3}$$

is the Coulomb attraction between electrons and nuclei with nuclear charge Z_I, separated by a distance $|\vec{r}_i - \vec{R}_I|$,

$$\frac{1}{2}\sum_{i\neq j} \frac{1}{|\vec{r}_i - \vec{r}_j|} \tag{2.4}$$

is the repulsive Coulomb contribution between a pair of electrons i and j, separated by a distance $|\vec{r}_i - \vec{r}_j|$, and

$$\frac{1}{2}\sum_{I \neq J} \frac{Z_I Z_J}{|\vec{R}_I - \vec{R}_J|} \tag{2.5}$$

is the Coulomb repulsion between any pair of nuclei I and J, separated by a distance $|\vec{R}_I - \vec{R}_J|$.

If we could solve the Schrödinger equation, we could predict the behavior of any system. Except for a few problems for which there is an exact solution of the Schrödinger equation (e.g., the hydrogen atom, harmonic oscillator, and a particle in a box), most real-life problems are not solvable due to the exceedingly large number of degrees of freedom for the total wavefunction of system $\Psi(\vec{r}, \vec{R})$, which depends on the positions of each electron and each nucleus in the system. For a system consist of N electrons with coordinates $\vec{r}_1, \vec{r}_2, \ldots, \vec{r}_N$ and M nuclei with coordinates $\vec{R}_1, \vec{R}_2, \ldots, \vec{R}_M$, we can write the total wavefunction as:

$$\Psi(\vec{r}, \vec{R}) = \Psi(\vec{r}_1, \vec{r}_2, \ldots, \vec{r}_N; \vec{R}_1, \vec{R}_2, \ldots, \vec{R}_M) \tag{2.6}$$

and the probability of simultaneously finding electron(nucleus) number 1 at point $\vec{r}_1(\vec{R}_1)$, electron(nucleus) number 2 at point $\vec{r}_2(\vec{R}_2)$, and so forth can be obtained from $|\Psi(\vec{r}_1, \ldots, \vec{r}_N; \vec{R}_1, \ldots, \vec{R}_M)|^2$. As one can imagine, equation 2.1 is very complicated and not directly solvable. To approach the formidable task of solving this equation, a series of approximations are needed.

2.2 Born-Oppenheimer approximation

In 1927, Born and Oppenheimer suggested [59] that because of the much higher mobility of electrons in comparison to the nuclei (arising from the difference in their mass: $m_e << m_{nuc}$), we can split the total wavefunction into an electronic and a nuclear part:

$$\Psi(\vec{r}, \vec{R}) = \psi_e(\vec{r}; \vec{R})\psi_n(\vec{R}) \tag{2.7}$$

Using this approximation, we can consider the nuclei as an external potential, $V_{ext}(\vec{R})$, and solve the electronic part of the equation 2.1 at fixed nuclear coordinates. In this case, the ground-state energy of the electronic system is directly dictated by the (fixed) potential of the nuclei. The Born–Oppenheimer (B-O) approximation is also referred to as the adiabatic approximation, as it implicitly assumes that the nuclei move so slowly and electrons always have enough time to evolve and maintain their lowest energy state [60].

By taking the Born-Oppenheimer approximation into account, we can write the electronic part of the Schrödinger equation as:

$$\left[-\sum_i \frac{\nabla_i^2}{2} + V_{ext}(\vec{r}_i, \vec{R}_I) + \frac{1}{2}\sum_{i\neq j}\frac{1}{|\vec{r}_i - \vec{r}_j|}\right]\psi(\vec{r}_i, \vec{R}_I) = E\psi(\vec{r}_i, \vec{R}_I) \tag{2.8}$$

where,

$$V_{ext} = -\sum_{i,I}\frac{Z_I}{|\vec{r}_i - \vec{R}_I|} \tag{2.9}$$

is the Coulomb potential of the nuclei felt by the electrons and it is clearly dependent on the nuclear positions.

Then, for a given nuclear configuration of $\vec{R}_I$ surrounded by N indistinguishable electrons, the $3N$-dimensional electronic wavefunction and the total electron density could be written as:

$$\psi\left(\vec{r}\right) = \psi\left(\vec{r}_1, \ldots \vec{r}_N\right) \tag{2.10}$$

$$\begin{aligned} n(\vec{r}) = \langle\psi|\sum_{i=1}^{N}\delta\left(\vec{r}-\vec{r}_i\right)|\psi\rangle = \int d\vec{r}_2 \ldots \int d\vec{r}_N \left|\psi\left(\vec{r}, \vec{r}_2, \ldots, \vec{r}_N\right)\right|^2 + \\ \cdots + \int d\vec{r}_1 \ldots \int d\vec{r}_{N-1}\left|\psi\left(\vec{r}_1, \ldots, \vec{r}_{N-1}, \vec{r}\right)\right|^2 \\ = N\int d\vec{r}_2 \ldots \int d\vec{r}_N \left|\psi\left(\vec{r}, \vec{r}_2, \ldots, \vec{r}_N\right)\right|^2 \end{aligned} \tag{2.11}$$

in which, $\delta(\vec{r}-\vec{r}_i)$ is the Dirac delta function.

2.3 Hartree-Fock theory

Hartree was the first one who proposed that the total electronic wavefunction of the system can be considered as a product of individual one-electron wavefunctions. Therefore, for a fixed external potential of the nuclei, the Hartree product states $\psi\left(\vec{r}_1, \ldots \vec{r}_N\right) = \phi\left(\vec{r}_1\right)\ldots\phi\left(\vec{r}_N\right)$ and the Schrödinger equation for each electron can be written as:

$$\left[-\frac{\nabla^2}{2}+V_{ext}(\vec{r},\vec{R}_I)\right]\phi_i\left(\vec{r}\right)=\epsilon_i\phi_i\left(\vec{r}\right) \tag{2.12}$$

where ϵ_i is the energy eigenstate of the individual electron i. Now the $3N$-dimensional problem has been simplified into N 3-dimensional wave equations for $\phi_i\left(\vec{r}\right)$. However, equation 2.12 is incomplete as it does not include the effect of other electrons in the system. In order to consider the electrostatic potential that each electron experiences from the presence of an average electron density of $n(\vec{r})$, we need to add an extra term known as the Hartree potential to the one-electron Hamiltonian. The Hartree potential is defined as:

$$V_H(\vec{r})=\int d\vec{r'}\frac{n(\vec{r'})}{|\vec{r}-\vec{r'}|} \tag{2.13}$$

and it represents the Coulomb interaction of an electron with the surrounding electron density $n(\vec{r})=2\sum_i|\phi_i(\vec{r})|^2$ (the sum runs over all occupied states). The factor 2 on the right hand side of the density equation indicates the number of electrons occupying up and down spin states. By including the Hartree potential in the Hamiltonian, the one-electron Schrödinger equation becomes:

$$\left[-\frac{\nabla^2}{2}+V_{ext}(\vec{r},\vec{R}_I)+V_H(\vec{r})\right]\phi_i(\vec{r})=\varepsilon_i\phi_i(\vec{r}) \tag{2.14}$$

This simplification based on the Hartree product violates the Pauli exclusion principle which states that the total electronic wavefunction $\psi(\vec{r})$ must be antisymmetric under the interchange of any two electrons: $\psi\left(\ldots\vec{r}_i,\vec{r}_j,\ldots\right)=-\psi\left(\ldots\vec{r}_j,\vec{r}_i,\ldots\right)$. This flaw in Hartree's approximation later on was resolved in the improved Hartree-Fock (HF) theory [61, 62]. By considering the spin of electrons and employing the Slater determinant [63], which guarantees satisfaction of the Pauli exclusion principle under electron exchange, we can write the total electronic wavefunction as:

$$\psi(\vec{r},\vec{s})=\frac{1}{\sqrt{N!}}\begin{vmatrix}\phi_1\left(\vec{r}_1,\vec{s}_1\right) & \phi_1\left(\vec{r}_2,\vec{s}_2\right) & \ldots & \phi_1\left(\vec{r}_N,\vec{s}_N\right)\\ \phi_2\left(\vec{r}_1,\vec{s}_1\right) & \phi_2\left(\vec{r}_2,\vec{s}_2\right) & \ldots & \phi_2\left(\vec{r}_N,\vec{s}_N\right)\\ \vdots & \vdots & \ddots & \vdots\\ \phi_N\left(\vec{r}_1,\vec{s}_1\right) & \phi_N\left(\vec{r}_2,\vec{s}_2\right) & \ldots & \phi_N\left(\vec{r}_N,\vec{s}_N\right)\end{vmatrix} \tag{2.15}$$

In order to consider the interaction of the electrons with each other, and provide an improved interpretation for their quantum mechanical nature, we need to also include additional terms for electron exchange and correlation effects in the Hamiltonian. It has been exquisitely explained in [60] that by minimization of the ground state energy of the system with respect to the one-electron wavefunctions presented in equation 2.15, and applying the orthogonality and normalization conditions as:

$$\int d\vec{r}\phi_i^*(\vec{r})\,\phi_j(\vec{r}) = \delta_{ij} \tag{2.16}$$

we can obtain the Hartree-Fock equation:

$$\begin{aligned}&\left[-\frac{\nabla^2}{2} + V_{ext}(\vec{r}, \vec{R}_I) + V_H(\vec{r})\right]\phi_i(\vec{r})\\ &-\sum_j \int d\vec{r'}\frac{\phi_j^*(\vec{r'})\phi_j(\vec{r})}{|\vec{r}-\vec{r'}|}\delta_{s_i s_j}\phi_i(\vec{r'}) = \varepsilon_i\phi_i(\vec{r})\end{aligned} \tag{2.17}$$

Equation 2.17 is the same one-electron Schrödinger equation with an additional term called exchange potential that considers the repulsion between electrons of the same spin. In this equation, $\delta_{s_i s_j}$ shows that the exchange term vanishes in case that ϕ_j and ϕ_i have different spins. It is clear that the solution $\phi_i(\vec{r})$ depends on electron density $n(\vec{r'})$ which is reciprocally dependent on the electronic wavefunction. The primary approach to solve the one-particle effective Hamiltonian is to resort to a calculation loop called the self-consistent field (SCF) approach which starts with speculation of the total electron density and then continues to repeat the cycle until reaching to the actual $n(\vec{r})$. The HF approach provides reasonable results for the atomic and molecular total energies. On the other hand, the so-called electron correlation (i.e., a correlation arising from Coulomb repulsion between electrons and affecting their spatial positions) effects are absent in this theory. Shortcomings of the HF method has motivated the development of advanced (and expensive) models such as configuration interaction (CI), coupled cluster (CC), Møller–Plesset perturbation theory (MP), and the quadratic configuration interaction (QCI) approach to include a description of electron correlation and provide a more accurate atomistic description of materials [64].

2.4 Density Functional Theory

2.4.1 Hohenberg-Kohn theorem

In 1964, Hohenberg and Kohn postulated the fundamentals of the modern density functional theory by proposing a new approach [65] to deal with the many-body problem for a system of interacting electrons while considering the effects arising from the electron correlations. This approach is based on two theorems:

1) The total ground-state energy of the system is a unique functional of the electron density.

2) The energy functional $E[n(\vec{r})]$ has its minimum when $n(\vec{r})$ corresponds to the ground-state electron density of the system. Therefore, the minimum of the energy functional is precisely equivalent to the actual ground-state energy.

Hohenberg and Kohn established their theorem by proving that the ground state electron density of the system can determine the external potential V_{ext}, and in return the external potential can uniquely determine the total electronic wavefunction ψ.

Although the Hohenberg-Kohn theorem states that by minimization of the total energy with respect to the electron density we can achieve the ground state energy of the system, it does not provide a framework to construct the corresponding energy functional for such a minimization scheme.

By considering that the external potential of the nuclei is explicitly dependent on the electron density, we can write the supposed energy functional $E[n]$ as:

$$E\left[n\right] = F\left[n\right] + \int V_{ext}(\vec{r}, \vec{R}_I) n(\vec{r}) d\vec{r} \tag{2.18}$$

in which $F\left[n\right]$ is an unknown functional that includes kinetic, Hartree, and the Coulomb energy contributions.

2.4.2 Kohn–Sham equations

In 1965 Kohn and Sham introduced an approach [66] for calculating the unknown part of the energy functional, *viz.* by replacing the system of interacting electrons with an assumed system of independent electrons with the exact same density and writing the $F[n]$ as:

$$F[n] = E_K[n] + E_H[n] + E_{xc}[n] \tag{2.19}$$

in which E_K and E_H are the kinetic and the Hartree energy of the system of non-interacting electrons, respectively. E_{xc} is called the exchange-correlation energy and it represents the difference between the actual electronic system and the fictitious non-interacting system.

In this case, the Hartree energy is given by:

$$E_H[n(\vec{r})] = \frac{1}{2}\iint d\vec{r}d\vec{r'}\frac{n(\vec{r})\,n(\vec{r'})}{|\vec{r}-\vec{r'}|} \tag{2.20}$$

and the kinetic energy of the independent electrons can be obtained from:

$$E_K[n(\vec{r})] = -\frac{1}{2}\sum_i \int d\vec{r}\phi_i^*(\vec{r})\,\nabla^2\phi_i(\vec{r}) \tag{2.21}$$

where the orbitals $\phi_i(\vec{r})$ are the solutions of the one-electron Kohn-Sham equations:

$$\left[-\frac{1}{2}\nabla^2 + V_{ext}(\vec{r},\vec{R}_I) + V_H(\vec{r}) + V_{xc}(\vec{r})\right]\phi_i(\vec{r}) = \epsilon_i\phi_i(\vec{r}) \tag{2.22}$$

and by combining all the components, the total energy can be re-written as:

$$\begin{aligned} E[n] = \int d\vec{r}V_{ext}(\vec{r},\vec{R}_I)n(\vec{r}) - \frac{1}{2}\sum_i\int d\vec{r}\phi_i^*(\vec{r})\nabla^2\phi_i(\vec{r}) \\ + \frac{1}{2}\iint d\vec{r}d\vec{r'}\frac{n(\vec{r})n(\vec{r'})}{|\vec{r}-\vec{r'}|} + E_{xc}[n] \end{aligned} \tag{2.23}$$

The exchange-correlation potential is written as a functional derivative:

$$V_{xc}(\vec{r}) = \left.\frac{\delta E_{xc}[n]}{\delta n}\right|_{n(\vec{r})} \tag{2.24}$$

which accounts for all the remaining "uncertainty" about $F[n]$. In plain text, the exchange-correlation potential contains the exchange part for keeping electrons of the same spin away from each other and the correlation part for separating electrons from each other due to the electrostatic forces. The main challenge here is to find the form of V_{xc} functional. Fortunately, several approximate functionals have been developed since the formulation of Kohn-Sham equations.

2.4.3 Exchange-Correlation functionals

The Local-Density Approximation (LDA)

This is the simplest approximation for the calculation of V_{xc} and it assumes that the electron density varies very slowly in a way that we can treat the electronic system as a homogeneous electron gas. The LDA approximation can be written as:

$$E_{xc}^{LDA}[n] = \int d\vec{r} n(\vec{r}) V_{xc}(n(\vec{r})) \tag{2.25}$$

where $V_{xc}(n(\vec{r}))$ is the XC energy density at point $\vec{r}$. Adopting the homogeneous electron gas approximation, the exact form of $V_{xc}(n(\vec{r}))$ is known from highly accurate Quantum Monte-Carlo (QMC) calculations.

Despite its simplicity, LDA has been a quite successful approach for many applications, specially when the electron density of the system of study is very high. On the other hand, LDA does not consider long-range effects and it gives underestimated correlation energies and overestimated exchange energies.

The Generalized-Gradient Approximation (GGA)

Considering that every real system has a spatially varying electron density, it can be expected that considering these density variations could make improvements over the LDA approximation. Therefore, by considering the local electron density and its gradient, we can get the GGA functional as:

$$E_{xc}^{GGA}[n] = \int d\vec{r} n(\vec{r}) V_{xc}(n(\vec{r}), \nabla n(\vec{r})) \tag{2.26}$$

In comparison to the LDA, GGA yields better results for the regions that the electron density is small. However, same as the LDA, long-range effects such as Van der Waals interactions are missing in GGA and there is a need for additional dispersion corrections. Interested readers are referred to some of the papers published by Stefan Grimme (and his colleagues)[67–69].

A multitude of GGA functionals have been developed, including the famous Becke exchange functional [70]:

$$E_x^{B88} = E_x^{LDA} - \beta \int d\vec{r} n^{4/3} \frac{\beta x^2}{1 + 6\beta \sinh^{-1} x} \tag{2.27}$$

where $x = \frac{|\nabla n|}{n^{4/3}}$ is the dimensionless ratio and $\beta = 0.0042$ is a constant.

And Lee, Yang, Parr (LYP) correlation functional [71]:

$$E_c^{LYP} = -a \int d\vec{r} \frac{n + bn^{-2/3} \left(C_F n^{5/3} - \frac{17}{9} t_W + \frac{1}{18} \nabla^2 n \right) e^{-cn^{-1/3}}}{1 + dn^{-1/3}} \tag{2.28}$$

in which $a = 0.049$, $b = 0.132$, $c = 0.2533$, and $d = 0.349$ and $t_W = \frac{1}{8} \frac{|\nabla n|^2}{n} - \frac{1}{8} \nabla^2 n$ is a local "Weizsacker" kinetic energy density [71].

There has been continuous improvement in the formulation of GGA functionals after LYP, which has resulted in the development of *a.o.* PW91 [72], PBE [73], RPBE [74], and PBEsol [75] functionals for different applications.

Hybrid Functionals

A hybrid functional is constructed by combining orbital-dependent HF with the explicit density functional approach (LDA/GGA). Hybrid functionals are the most accurate functionals available (as far as energetics are concerned), but they are much more expensive than pure GGA functionals. Hybrid functionals are normally used to perform single-point energy calculations on medium-sized systems.

2.4.4 Atomic forces

For the calculation of interatomic forces, we need to focus on the nuclear part of the total wavefucntion $\Psi(\vec{r}, \vec{R})$, by writing the corresponding Hamiltonian as:

$$\hat{H}_{nuc} = -\sum_I \frac{\nabla_I^2}{2M_I} + E_{N-N}(\vec{R}_I) + E(\vec{R}_I) \tag{2.29}$$

The first term on the right hand side of this equation is the kinetic energy of nuclei, E_{N-N} is the interatomic Coulomb potential energy and $E(\vec{R}_I)$ represents the total energy of electrons when the nuclei are located in positions $\vec{R}_1, \ldots, \vec{R}_M$.

The force acting on the atomic nuclei can be obtained by the derivative of the total potential energy ($E_{N-N}(\vec{R}_I)+E(\vec{R}_I)$) with respect to the nuclear positions:

$$F_I = -\frac{dE}{d\vec{R}_I} = -\frac{dE_{N-N}}{d\vec{R}_I} - \frac{dE(\vec{R}_I)}{d\vec{R}_I} \tag{2.30}$$

One can imagine that the calculation of the derivatives of the energy with respect to every single atomic coordinate could be very computationally challenging. By considering that $\psi_n(\vec{R})$ is an eigenstate of the Hamiltonian, Hellman-Feynman theorem [76, 77] suggests that instead of calculating derivative of the energy, we can calculate the expectation value of the derivative of the Hamiltonian with respect to $\vec{R}_I$:

$$\frac{\partial E}{\partial \vec{R}_I} = \int d\vec{r}\psi_n^*(\vec{R})\frac{\partial \hat{H}}{\partial \vec{R}_I}\psi_n(\vec{R}) \tag{2.31}$$

which leads to:

$$\begin{aligned}\vec{F}_I &= -\frac{\partial V_{ext}}{\partial \vec{R}_I} - \frac{\partial E_{N-N}}{\partial \vec{R}_I} \\ &= Z_I \int d\vec{r} n(\vec{r})\frac{(\vec{r}-\vec{R}_I)}{|\vec{r}-\vec{R}_I|^3} - \sum_{J\neq I} Z_J Z_I \frac{(\vec{R}_J-\vec{R}_I)}{|\vec{R}_J-\vec{R}_I|^3}\end{aligned} \tag{2.32}$$

With this approach and employing complete and position independent basis sets, calculation of the atomic forces is straightforward. For methods that employ atom-centered basis sets, additional terms (known as Pulay forces [78]) must also be taken into account [79]. In addition to the methodology explained in the original papers (Hellman 1937 [76] and Feynman 1939 [77]), one can find more detailed information on the variational methods used for the calculation of forces from [60] and also from so many other textbooks devoted to the theory of computational material science.

2.4.5 Basis sets

Depending on the properties of the system that we tend to study, electronic wavefunctions can be represented in different forms.

$$\phi(\vec{r}) = \sum_i c_i \varphi_i(\vec{r}) \tag{2.33}$$

The main goal here is to find the coefficients c_i to be able to expand the Kohn-Sham orbitals in the spatial domain of study (*i.e. computational cell*). There are three main approaches for calculating independent electronic states in materials, and each method has its advantages and shortcomings.

Atom-centered basis sets

We can expand the wavefunction as a linear combination of localized atomic orbitals:

$$\phi_i(\vec{r}) = \sum_{I,nlm} c_{I,nlm}\varphi_{I,nlm}(\vec{r}) \tag{2.34}$$

in which n, l, and m are principal, angular and azimuthal quantum numbers, respectively. $\varphi_{I,nlm}(\vec{r})$ accounts for both the atomic coordinate ($\vec{R}_I$) and the orbital centred on that position.

Gaussian type orbitals are widely used in chemistry for non-periodic systems. By employing localized basis sets, only a small number of $c_{I,nlm}$ is needed to expand the wavefunction. On the other hand, Gaussian basis sets are not orthogonal (could lead to basis set superposition error (BSSE)), and as mentioned earlier, they give rise to Pulay forces when it comes to the calculation of atomic forces.

Plane-wave basis sets

One of the common applications of the Bloch's theorem [80], especially in periodic systems, is to use plane waves for the expansion of wavefunctions [81]:

$$\phi_{\vec{k}}(\vec{r}) = \sum_{\vec{G}} C_{n,\vec{k}+\vec{G}} e^{i(\vec{k}+\vec{G})\cdot\vec{r}} \tag{2.35}$$

In here, $\vec{k}$ is the wave vector within the first Brillouin zone, n is the band index and $C_{n,\vec{k}+\vec{G}}$ is the Fourier transform coefficient in reciprocal space. The $\vec{G}$ vectors are constructed from the primitive vectors of the reciprocal lattice.

Plane-waves are perfect for periodic and crystalline systems, and their implementation is straightforward. Also, they provide a complete and unbiased basis set since there is no dependence on atomic positions. The main disadvantage of using this method is that plane-waves span the entire simulation box, and the empty space is also included in the calculations, which requires a large number of plane-waves for the calculations.

Augmented plane-wave (APW) approach

APW is a mixed basis set of spherical harmonics centered on atoms and plane-waves in the interstitial region. The APW method is highly accurate but restricted to small systems.

2.4.6 Nudged Elastic Band (NEB)

The lowest energy path connecting two local energy minima is known as the minimum energy path (MEP). Identification of the MEP between an initial and a final stable configuration in a chemical reaction and localizing the transition state (TS), i.e., the saddle point along the reaction coordinate, is a common problem in computational chemistry. Among several different methods designed for this purpose, the Nudged Elastic Band (NEB) method [82, 83], is one of the most successful. This method is based on a linear interpolation of the atomic positions between the available initial and final structures. In order to get faster and more accurate results, sometimes intermediate configurations are also needed. These configurations are called “images”. The provided images are then connected using imaginary springs – forming a band – to keep them linked during the energy optimization process. The path is then optimized until the convergence criteria are met. NEB method is schematically shown in Figure 2.1.

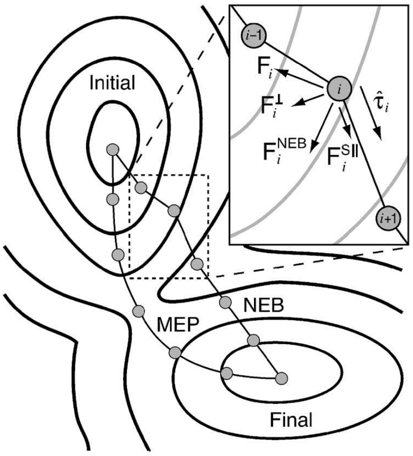

Figure 2.1: Schematic picture of the Nudged Elastic Band (NEB) method. Adapted from [84].

Calculation of energy and forces along the path requires separate DFT calculations for each image. If we consider harmonic springs with a spring constant k between the $N+1$ images located at $\vec{R}_0, \vec{R}_1, \ldots, \vec{R}_N$, the resulting force acting on each of the intermediate images can be written as:

$$F_i = -\nabla E(\vec{R}_i)|_{\perp} + F_i^S \cdot \hat{\tau}_i \hat{\tau}_i \tag{2.36}$$

where $\nabla E(\vec{R}_i)|_{\perp}$ and F_i^S represent the perpendicular force and the spring force affecting image i, respectively. $\hat{\tau}_i$ is the estimate of the unit tangent at image i given by the vector connecting images i and $i+1$. During the band optimization process, the energy and the gradient of all the intermediate images are taken into account to estimate the tangent to the reaction coordinate at each image.

2.5 Modeling of plasma-induced surface charging

A method for the treatment of charged configurations was developed in our group, PLASMANT, by Bal et al. [85]. In this approach, a positive charge is introduced to the system and located far from the surface (in the Z-direction) without assigning a local basis set to it. Therefore, the electron density is not allowed to be distributed around the ion, but it will be localized on the surface, which thus becomes negatively charged. This is an ideal approach for modeling the effect of plasma-induced excess electrons on the surface of a catalyst, because it explicitly incorporates both the negative charging from excess electrons, as well as the polarization effects and electric fields arising from positively charged ions in the plasma sheath region in the gas phase. Using this method, the surface charge density obtained is consistent with plasma catalysis experiments (electron density of 10^{15}–$10^{17}\, m^{-2}$) [85].

Electrostatic interactions are described with the Martyna-Tuckerman (MT) Poisson solver [86], which requires the Z-component of the cell size to be very large (100 Å) for charged configurations. The MT solver allows imposing full periodicity across the surface slab (in the XY plane), mimicking a semi-infinite catalyst surface, while simultaneously removing periodicity along the Z direction. As such, the slab's unphysical interactions with itself are avoided, which would otherwise result in significant computational artifacts when dealing with charged surfaces [87].

More details on the methodology and validation of results are provided in the following chapters.

2.6 Modeling of the external electric field effect

We explored two different methods for modeling the electric field effect: a constant potential method for the field-only effects, and the charged plates (or dipole sheet) method for considering the combined effects of electric field and excess electrons. As we will show in Chapter 4, both methods can yield equivalent energetics for the field-only calculations, but only the latter can be used in systems carrying a net charge. In this study, the direction of the electric field in all calculations is chosen to be normal to the surface of the metal slab and in $-\vec{Z}$ direction. So, all the positive numbers reported for the electric field represent its absolute value or strength.

The constant potential method is based on using an implicit (generalized) Poisson solver [88] by employing Dirichlet boundary conditions to simulate the applied voltage on the system without using dipole sheets. The main advantage of using Dirichlet boundary conditions is that this method makes it possible to directly apply a specified potential while eliminating the need for considering large supercells. Also, it maintains charge neutrality of the supercell during the calculations, which is important to avoid divergence of the energy.

In the charged plates approach, which we developed [89], we use a dipole sheet with some modifications to include the combined effect of the electric field and the excess electrons. This method requires localized (atom-centered) basis sets and is thus not applicable in packages using plane-waves only. In this approach, we use two charged plates as electrodes, and we employ the MT Poisson solver. Charged plates consist of atomic cores with modified charges so that both plates are charged with opposite signs, making a dipole sheet in the middle of the simulation box. Using this novel technique [89] has made it possible to fine-tune the amount of charge on the plates and the corresponding electric field strength between dipole sheets. For considering the combined effect of an electric field and one excess electron, we can add one unit of implicit extra charge to the system together with the charged plates. Figure 2.2 shows a schematic picture of both methods.

Using the constant potential approach, the electric field strength on a conductor surface depends on the distance between the electrodes and correspondingly on the thickness of the metal slab ($E = \frac{\Delta V}{D-d}$), in which E is the field strength, ΔV is the potential difference, D is the distance between the electrodes, and d is the slab thickness. This makes it feasible to consider a change in electric field strength due to the morphology and the thickness of the surface. In other words, depending on the thickness and roughness of the used slab, the strength of the electric field arising from a specific potential would be different.

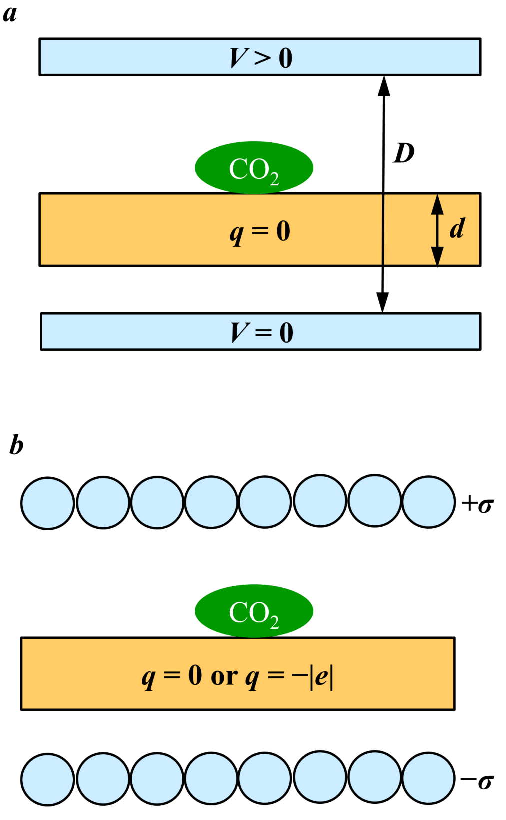

Figure 2.2: a) Constant potential method used for "field only" effect and b) Dipole sheet method used for the combined effect of charge and external field on CO_2 activation over Cu surfaces.

Using the dipole sheet approach, the strength of the electric field between the charged plates is given by ($E = \frac{\sigma}{\varepsilon_0}$) in which σ is the surface charge density of the dipole sheet and ε_0 is the vacuum permittivity. Thus, the distance between the charged plates and the slab's thickness does not affect the electric field strength. However, the charged plates cannot be placed too close to the slab to avoid direct interactions with the dummy ions in the plates.

Chapter 3

Effect of Plasma-Induced Surface Charging on CO_2 Activation[*]

---

[*] This chapter is published as: A. Jafarzadeh et al. "CO_2 Activation on TiO_2-Supported Cu_5 and Ni_5 Nanoclusters: Effect of Plasma-Induced Surface Charging," *J. Phys. Chem. C*, vol. 123, no. 11, pp. 6516–6525, Feb. 2019.

3.1 Introduction

As explained in the introduction, the plasma is a highly reactive but non-selective environment that can suitably be combined with a catalyst. In particular, the plasma leads to a modification of the gas phase (and hence the reactants) while still allowing for a (relatively) low gas temperature (e.g., room temperature or slightly above). The contribution of all the specific plasma factors strongly depends on the type of plasma and the working conditions. The mechanisms of plasma-induced changes in the catalyst structural and electronic properties remain mostly unresolved. To unravel (some of) the mechanisms underlying plasma-catalyst interactions, it is useful to narrow down the complexity of the system by focusing on one specific factor at a time and its effect on the whole plasma-catalytic process.

A catalyst surface becomes inevitably charged upon interaction with plasma. The accumulated surface charge can alter the catalyst electronic and geometric structure, leading to a change in the whole catalytic reaction thermodynamics and kinetics. Even changes in the activity of the different geometric structures of a catalyst are generally ascribed to differences in their electronic structures [90]. Hence, by investigating the catalyst electronic properties during its interaction with the plasma, we gain information about the effect of plasma-induced surface charging on catalytic reactions.

The effect of surface charging is important in heterogeneous catalysis, and in particular, when transition metal clusters are deposited on oxide surfaces. Excess electrons accumulated on the oxide surface can alter the electronic structure and adsorption properties of the supported transition metal nanoparticles. Although there have been both experimental [91, 92] and theoretical [93, 94] investigations on the effect of plasma in heterogeneous catalysis, and studies have been carried out on the deposition of metal clusters on oxide surfaces without plasma, [95–97] the effect of plasma-induced excess electrons on the deposition of metal clusters and their catalytic properties has been scarcely investigated.

Both nickel and copper are widely used in heterogeneous catalysis, for instance, for CO_2 conversion into value-added products like methanol [94, 98, 99]. We here choose to study Ni and Cu pentamers. First, these clusters can be synthesized and are actually used in the catalysis community. Further, they require minute amounts of material because of their small size, making them cheaper (per unit surface area). Finally, considering the limited number of possible isomers, their fluxionality (in the gas phase) is much less than for larger clusters, making them computationally tractable.

In this chapter, we report on the role of excess electrons on (1) the adsorption of Ni_5 and Cu_5 clusters on an anatase TiO_2 (101) slab; (2) adsorption of an adsorbate molecule (CO_2) on the stoichiometric surface of anatase TiO_2 (101); (3) adsorption of a CO_2 molecule on TiO_2-supported Ni_5 and Cu_5 clusters; and (4) dissociation of the CO_2 molecule.

As a reducible oxide, TiO_2 is interesting to investigate the effects of surface charging. Among the various polymorphs of titania, anatase has been widely used in modeling catalytic reactions [95–97, 100, 101]. The (101) plane of anatase (a-TiO_2) has been chosen for the adsorption of the metal clusters because of its high thermodynamic stability [96].

3.2 Computational details

All calculations were carried out based on spin-polarized density functional theory (DFT) by using the Quickstep [102] module of the CP2K [103] version 5.1 package. This module employs localized Gaussian orbitals and auxiliary plane waves as a dual basis for expanding the Kohn-Sham orbitals. Double–ζ valence plus polarization (DZVP) basis sets which are optimized from molecular interactions (MOLOPT) [104] combined with a plane wave basis set with 800 Ry cutoff were used for the calculations. Goedecker-Teter-Hutter (GTH) pseudopotentials [105, 106] were used for describing the inner shell electrons; for C, O, Cu, Ti, and Ni atoms, 4, 6, 11, 12, and 18 valence electrons are explicitly considered, respectively. The GGA-PBE functional [73] was applied for treating electron exchange and correlation effects. Dispersion interactions were included through Grimme's D3 approximation along with Becke-Jonsson damping [68, 69]. The Broyden-

Fletcher-Goldfarb-Shanno (BFGS) scheme was used for geometry optimization, where a maximum force of 0.02 $eV/\text{Å}$ was set for the relaxation of atoms. k-point sampling was limited to the Γ–point only, and the Hirshfeld-I scheme [107] was used for charge analysis of interactions between the adsorbates and the slab surface. Thermal and zero-point energy calculations were not considered.

Lattice parameters of bulk anatase with $a = b = 3.7845$ Å and $c = 9.5143$ Å) [108] were used for creating the surface slabs. A slab of anatase (101) with dimensions of $10.239 \times 11.3535 \times 30.00$ Å^3 (1×3 supercell) consisting of 6 (O-Ti-O) trilayers and containing 108 atoms (Figure 3.1) was used for the calculations. We fixed the bottom layers of the support in the first set of calculations to mimic the bulk-like structure. This, however, also leads to interference in the excess electron's localization pattern. Thus, we also examined a fully relaxed structure, with no atoms frozen. The results with the fixed layers are provided in Appendix 1. We here mainly focus on the results achieved without applying any constraint on the relaxation of the atoms. Calculations for the metal clusters and the CO_2 molecule in the gas phase were done in a box of $15 \times 15 \times 15$ Å^3 dimensions.

We employed DFT+U [109, 110] calculations for cross-checking the results while accounting for the strong on-site Coulomb interactions. By using this approach, the self-interaction effect for Ti *d*-orbitals was corrected by Hubbard's U parameter. This parameter was set to 5 eV for Ti atoms, as suggested by previous studies [111–113]. Considering the small number of atoms in clusters studied in this work and the negligible impact of their self-interaction on the results, no Hubbard parameter is applied to the *d*-orbitals of Ni and Cu atoms. Considering that DFT+U provides a better picture for electron localization on support cations, the PDOS and spin density diagrams were obtained from the DFT+U calculations.

We investigated the effect of charge in two ways: First, re-optimization of the neutral structure after adding an excess electron to the system, and second, optimization of the initially negatively charged configuration. We compared the corresponding adsorption energies and other properties for the neutral and negatively charged structures after finding the most stable mode for both neutral and

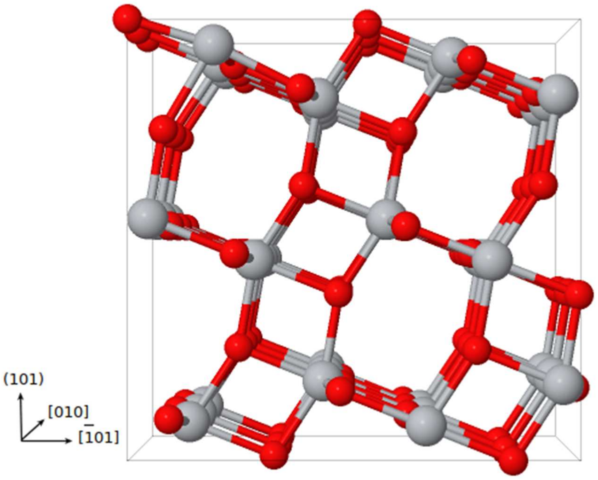

Figure 3.1: (1 × 3) supercell of anatase TiO_2 (101).

charged configurations.

Adsorption energies of clusters on anatase are calculated based on equation 3.1, where $E_{cluster}$ is the total energy of the Ni_5/Cu_5 clusters, $E_{slab+cluster}$ is the total energy of the complex (consisting of cluster and surface) and E_{slab} is the total energy of the bare slab:

$$E_{Adsorption} = E_{slab+cluster} - E_{cluster} - E_{slab} \tag{3.1}$$

Similarly, the adsorption energy of CO_2 on the supported cluster is calculated as:

$$E_{Adsorption} = E_{complex+molecule} - E_{complex} - E_{molecule} \tag{3.2}$$

3.3 Results and discussion

3.3.1 Adsorption of Ni_5 and Cu_5 clusters on the anatase (101) surface

To investigate the adsorption of Cu_5 and Ni_5 on the TiO_2 surface, we first optimized their structure in the gas phase, as described in Appendix 1. The clusters were then deposited on the neutral anatase (101) surface, and their adsorption energy was calculated. Subsequently, one electron was added to this configuration, and the system was re-optimized. This allowed us to compare the adsorption properties of each metal cluster in the neutral and charged systems.

Similar to the gas phase calculations, we explored five initial structures with different orientations relative to the surface. Then we examined the most stable orientation in five different adsorption sites. The most stable configurations found for Ni_5 and Cu_5 adsorption are shown in Figure 3.2, while the unstable adsorption modes are provided in Appendix 1. We acknowledge that this procedure does not guarantee finding the global minimum.

Upon adsorption, hardly any change in the shape of the Ni_5 cluster is seen. Adsorption of the Ni_5 cluster on the anatase surface changes the support's electronic structure. In agreement with the literature, the Ni *d*-orbitals fill the bandgap of the TiO_2 semiconductor (see Appendix 1) [114, 115]. Population analysis based on the Hirshfeld scheme shows that during the adsorption of $Ni_{5,}$ there is a charge transfer from the support to the cluster. For the gas phase Ni_5 cluster, the total spin moment (n_α–n_β) is $2\mu_B$ (triplet state) which changes to $3.1\mu_B$ upon adsorption. Also, the accumulated net charge of -0.893 $|e|$ on the Ni_5 cluster shows that there is a significant charge transfer between the surface and the cluster, which leads to a high adsorption energy of -5.72 eV. This electron transfer from the support to the cluster leaves the support with one unpaired electron, as seen from the spin density isosurfaces (Figure 3.3a).

Upon adsorption, the Cu_5 cluster changes its original planar configuration to a more 3D structure, facilitating a strong interaction between the cluster and the oxide surface with an adsorption energy of -4.29 eV. In comparison to Ni_5, the *d*-orbitals of the Cu_5 cluster partially lie in the TiO_2 bandgap with a tendency to be located near the valence band (see Appendix 1). The direction of the charge transfer between the support and cluster is different for Ni_5 and Cu_5. The Cu_5 has a total spin moment of $1\mu_B$ (doublet state) in the gas phase, which changes to 0 after its adsorption on the support surface. During the adsorption, one unpaired electron in the Cu_5 cluster is transferred to the support. From Figure 3.3c we can see that the transferred electron localizes on the subsurface Ti atom of the support.

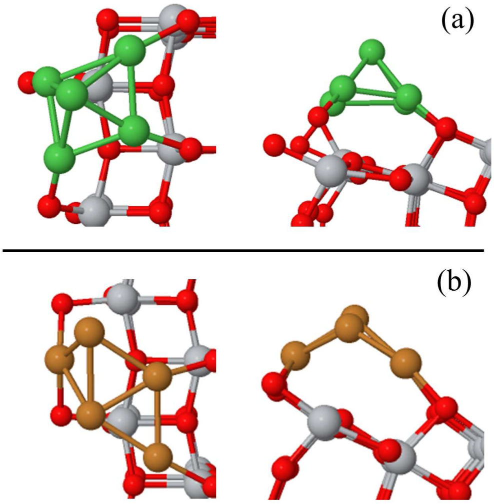

Figure 3.2: Top and side view of the most stable configurations of a) Ni_5 and b) Cu_5 clusters on anatase TiO_2 (101) slab.

After adding an excess electron to the relaxed neutral structures and re-optimization, no change in the adsorption mode is seen. Changes in adsorption energies, as described below, can therefore (mostly) be attributed to the effect of the negative charge (Figure 3.4). Adding a single excess electron to the surface model leads to an electron density of $8.6 \times 10^{17}\ m^{-2}$ or a surface charge density of $-0.137\ \frac{C}{m^2}$, which is in the same order of magnitude of experimental estimates of plasma-deposited charge densities on dielectrics [116], and a factor of four higher than reported in recent particle-in-cell/Monte Carlo collision PIC/MCC simulations for plasma in contact with dielectric surfaces or catalyst pores [117].

From the spin density analysis (Figure 3.3b) we can see that for the charged Ni_5 structure, the added electron is mostly localized on the Ni cluster, changing its net charge to $-1.643\ |e|$ and also the total net spin moment to $2.2\mu_B$. This gives rise to a change in adsorption energy of the cluster by $+0.06\ eV$, amounting to an adsorption energy of $-5.66\ eV$. However, in Figure 3.4, the DFT result without U correction shows that upon charging, the adsorption energy decreases by $-0.51\ eV$, which is mostly because of the failure in localization of the excess electron.

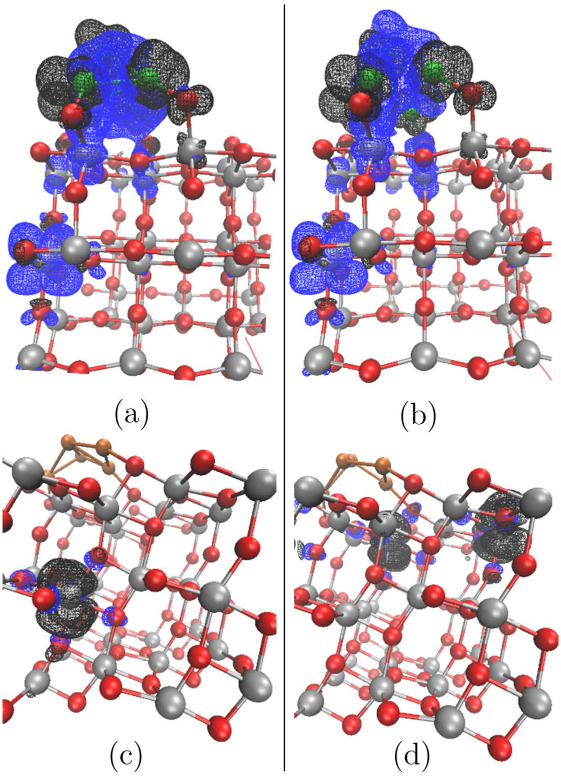

Figure 3.3: Spin density isosurfaces for a) neutral Ni_5/TiO_2, b) charged Ni_5/TiO_2, c) neutral Cu_5/TiO_2, and d) charged Cu_5/TiO_2 structures. The black and blue lobes correspond to spin up and spin down, respectively. Isovalues are set to ±0.001 $e/\text{Å}^3$.

In contrast, upon negatively charging the surface, no spin polarization on the Cu_5 is seen, which means that the added electron is not localized on the cluster (i.e., the net spin moment of the cluster remains zero). Instead, as can be seen from Figure 3.3 d, the presence of excess electrons leads to a change in the localization of the previously transferred electron. Eventually, two electrons are localized on the surface of the support, which decreases the adsorption energy by 1.20 eV for the Cu_5 cluster, amounting to an adsorption energy of -5.49 eV. A detailed summary of the changes in net spin moment and partial charges of the atoms for both neutral and charged structures is provided in Appendix 1.

These results highlight the different effect of excess charge on the adsorption properties of Cu and Ni pentamers. Methodologically, these results also show that depending on the localization procedure of the excess electron, its effect on

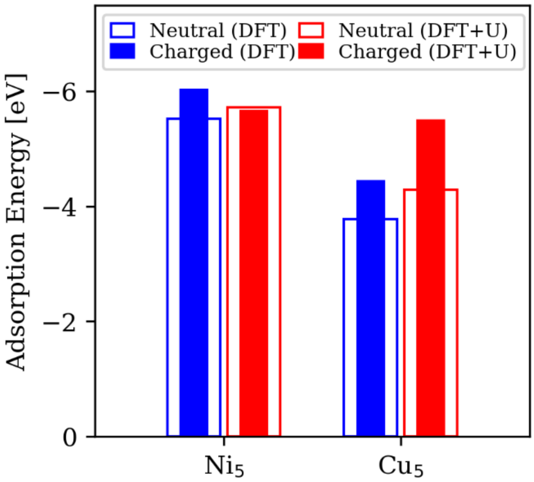

Figure 3.4: Adsorption energies of Ni_5 and Cu_5 clusters on anatase TiO_2 (101).

the stabilization of the adsorbed metal clusters can be different. Furthermore, it is seen that for fully relaxed systems, DFT calculations without considering on-site Coulomb interactions have difficulties describing the effect of excess electrons on the stability of the metal clusters.

3.3.2 CO_2 adsorption on anatase TiO_2 (101)

CO_2 adsorption on neutral anatase was previously studied by DFT [115, 118, 119]. In this study, we aim to investigate the effect of plasma-induced excess electrons on the adsorption of CO_2 on both the bare surface and on titania-supported Ni_5 and Cu_5 clusters. We will focus on the two most stable configurations for the adsorption of CO_2 on the anatase (101) surface, shown in Figure 3.5.

We first kept the three layers of the TiO_2 slab frozen in their bulk structure to allow for a direct comparison between the results for neutral structures and the literature. For the linear configuration, we find that CO_2 adsorbs on the neutral surface with an adsorption energy of $-0.44\ eV$ and $-0.51\ eV$ for DFT and DFT+U, respectively. The bent structure shows an adsorption energy of $-0.03\ eV$ using DFT, while DFT+U yields an adsorption energy of $-0.18\ eV$. It can be seen that the results coming from DFT+U are in agreement with the values of $-0.48\ eV$ for linear and $-0.16\ eV$ for carbonate-like structure, as reported by

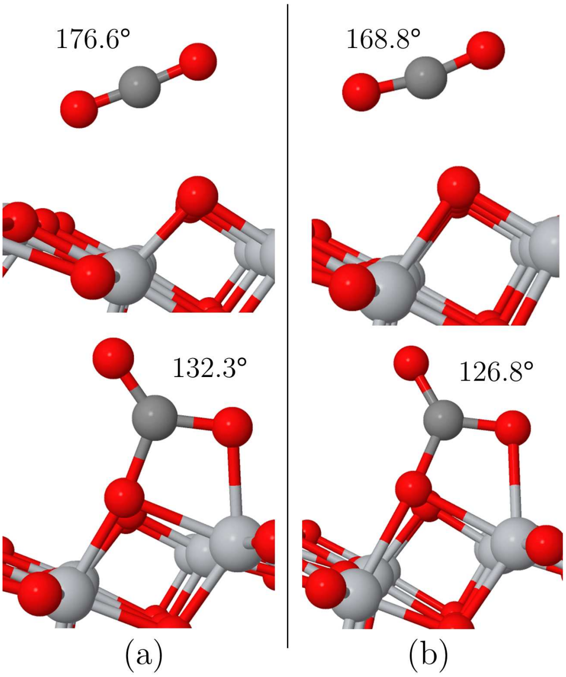

Figure 3.5: The most stable configurations for the linear and bent CO_2 structures adsorbing on the TiO_2 (101) surface. a) neutral and b) charged configurations.

Sorescu et al. [118]. Iyemperumal et al. [115] reported values of $-0.40\ eV$ and $-0.09\ eV$ for the most stable linear and bent structures, respectively. Results for both neutral and charged structures of CO_2 adsorption on bare TiO_2 (with fixed bottom layers) are shown in Figure 3.6 a.

By removing the constraint on the bottom layers of the slab, the electron distribution is unbiased, which permits a reliable comparison between the neutral and charged structures. The results for fully relaxed systems are provided in Figure 3.6 b. As we can see from this figure, the trends are maintained, although there are quantitative differences in adsorption energies achieved for the system with fixed layers.

By adding charge to the system, both adsorption modes essentially maintain their structure. In the linear adsorption mode, the effect of excess charge on the adsorption energy is less pronounced. In this case, there is no mixing between the electronic states of the molecule and the surface, such that the (small) increase in adsorption energy of the linear CO_2 can be attributed to polarization effects.

In this case, electrostatic Coulomb forces between the positive C atom and the negatively charged surface will lead to an improvement in adsorption energy. The PDOS of the linear adsorption mode for both neutral and charged structures (Figure 3.7 a,b) reveals that upon charging, the states of both oxygen atoms of the CO_2 molecule are shifted toward lower energies, and this leads to a small improvement in the stabilization of the molecule.

For the bent structure, there is a substantial increase in adsorption energy upon charging, to $-1.13\ eV$ and $-1.40\ eV$ in DFT and DFT+U, respectively, which is also reflected in the partial charges of CO_2 in the neutral and charged configurations: the partial charges on oxygen atoms of CO_2 molecule change from $-0.862\,|e|$ and $-0.624\,|e|$ (neutral system) to $-1.028\,|e|$ and $-0.728\,|e|$ (charged system). Considering that the surface Ti atom bonded to the oxygen atom of the CO_2 molecule has preserved its net charge from the neutral configuration, we can see that the increase in adsorption energy is mainly due to the change in partial charge of the molecule. This is consistent with the PDOS diagrams (Figure 3.7 d) of the charged configuration, showing a shift in the DOS of the oxygen atoms of CO_2 towards the valence band, facilitating the pronounced mixing with orbitals of the surface Ti atoms, in comparison to the neutral case.

Table 3.1 shows the effect of charge on the adsorption energy of the two most stable modes of CO_2 on titania achieved by DFT and DFT+U.

Transformation of the linear to the bent structure thus seems essential for CO_2 activation. It is clear from the results that adding a plasma–deposited excess electron to the system changes the most stable structure of the CO_2 adsorbed on the titania surface from a linear to a bent configuration, which makes the activation of the CO_2 molecule thermodynamically more favorable.

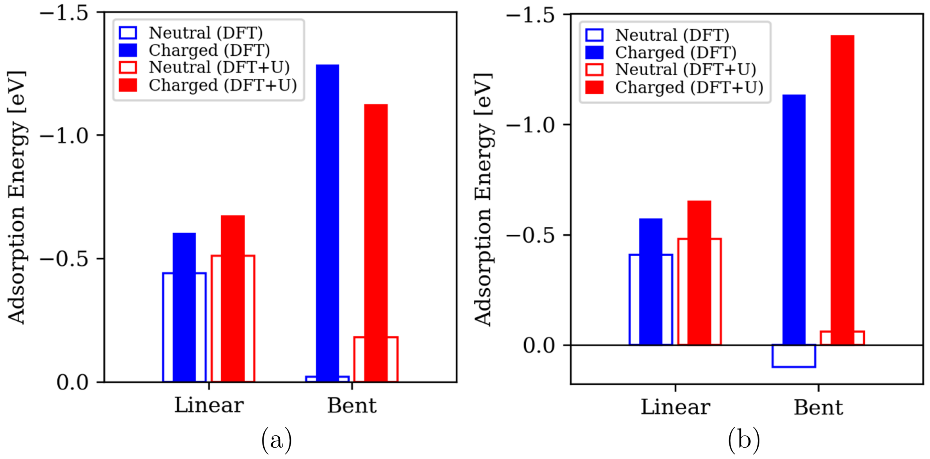

Figure 3.6: CO_2 adsorption energy for both linear and bent structures on neutral and charged configurations of anatase (101) - a) structures with three bottom layers kept frozen and b) fully relaxed structures.

Correspondingly, we also analyzed changes in the C-O bond length and the O-C-O bond angle due to negatively charging the surface. In Table 3.1, we summarize the results for the effect of charge on bond lengths and angles. The presence of excess charge has an impact on bending the CO_2 molecule, while the effect on C-O bond elongation is limited.

Table 3.1: Bond lengths and adsorption energies of the CO_2 molecule with linear and bent structures on both neutral and charged TiO_2 surfaces.

Method	**Structure**	**r(C-O)**	**(OCO)**	$\mathbf{E_{ads}}$ (eV)
DFT	Gas Phase	1.17, 1.17	180	
	Bent (Neutral)	1.20, 1.32	131.6	0.10
	Bent (Charged)	1.23, 1.32	126.4	-1.13
	Linear (Neutral)	1.17, 1.18	177.2	-0.41
	Linear (Charged)	1.18, 1.18	169.9	-0.57
DFT+U	Bent (Neutral)	1.20, 1.32	132.3	-0.06
	Bent (Charged)	1.23, 1.32	126.8	-1.40
	Linear (Neutral)	1.17, 1.18	176.6	-0.48
	Linear (Charged)	1.18, 1.18	168.8	-0.65

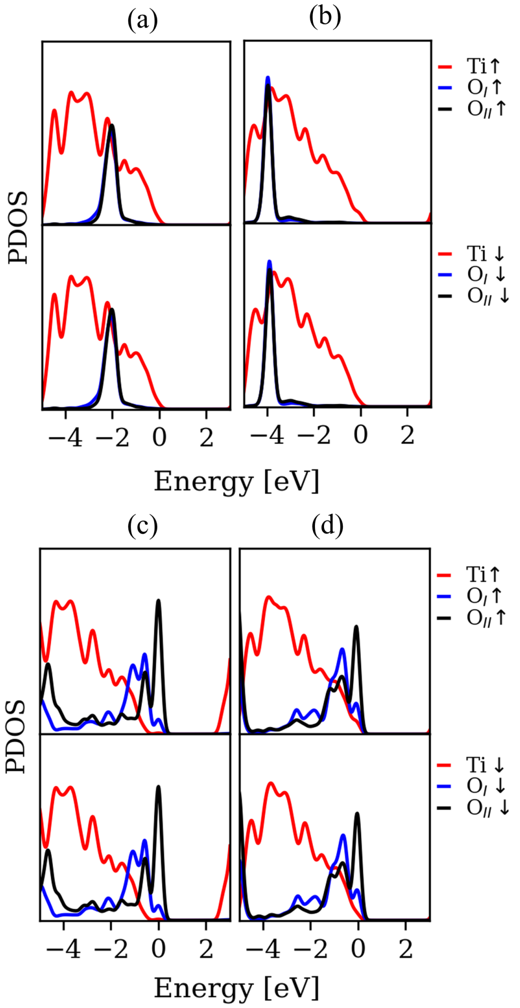

Figure 3.7: Projected density of states for the adsorption of a CO_2 molecule on TiO_2. a) linear-neutral, b) linear-charged, c) bent-neutral, and d) bent-charged structures. O_I and O_{II} are oxygen atoms of the CO_2 molecule. Up/down spin states are shown with up/down arrows.

3.3.3 CO_2 adsorption on supported clusters

For the adsorption of CO_2 on titania-supported clusters, various initial modes were examined. In this case, we optimized each initial structure both with and without the presence of plasma-induced excess electrons.

Adsorption of CO_2 on the supported Ni_5 cluster does not lead to a marked

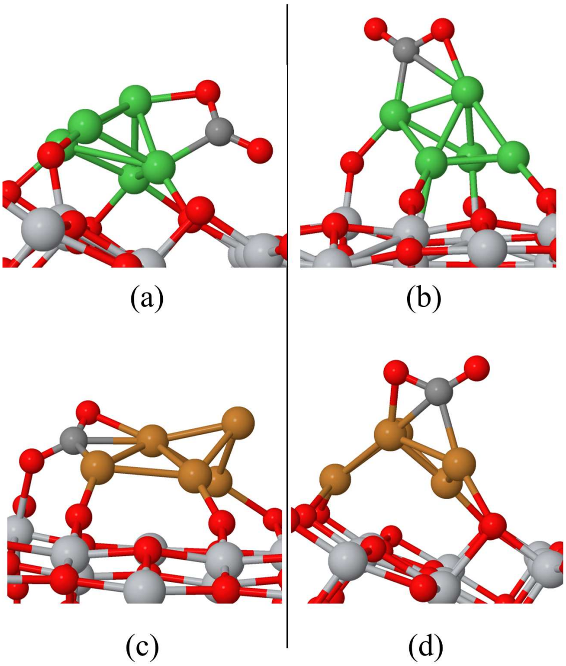

Figure 3.8: Adsorption of CO_2 on supported a) Ni_5-neutral, b) Ni_5-charged, c) Cu_5-neutral, and d) Cu_5-charged structures.

change in the cluster shape. Bond formation between the CO_2 molecule and Ni atoms of the cluster results in a bent structure of CO_2 (Figure 3.8 a) with an adsorption energy of -0.53 and -0.31 eV for DFT and DFT+U, respectively. During CO_2 adsorption, the net spin moment of the cluster remains at $3\mu_B$, while its net charge increases from $-0.893\,|e|$ to $-1.412\,|e|$, indicating the formation of a polar covalent bond between the cluster and the C atom of the CO_2 molecule. The Ni atom which bonds to C has a net charge of -0.730 $|e|$, while the carbon atom has a charge of $1.769\,|e|$.

Adsorption of CO_2 on the supported Cu_5 cluster, on the other hand, results in a noticeable change in the cluster shape. In this case, CO_2 adsorbs on the interface via the C atom making bonds with two copper atoms of the cluster and the oxygen atom with a surface Ti atom (Figure 3.8 c). In this configuration, the Cu_5 cluster has three-fold coordination with surface oxygens and likewise a three-fold coordination with the CO_2 molecule, while maintaining a net spin moment of 0 and having a partial net charge of $-0.205\,|e|$. The net charge for the carbon and the two Cu atoms of the cluster is 1.502 $|e|$, $-0.064\,|e|$ and $-0.228\,|e|$, respectively. This shows the formation of a covalent bond between the cluster and the CO_2 molecule.

Bond lengths and adsorption energies of CO_2 on Ni_5 and Cu_5 clusters supported by anatase TiO_2 (101) are shown in Table 3.2. From this table and Figure 3.9, we observe a clear increase in the stability of the CO_2 molecule adsorbed on both clusters upon negatively charging the surface.

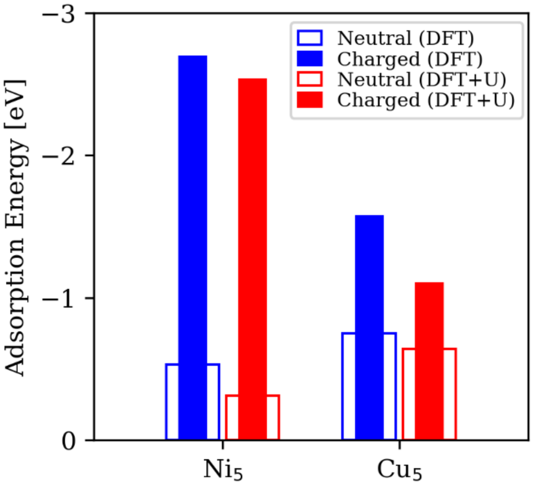

Figure 3.9: Adsorption energy of the CO_2 molecule on Ni_5/Cu_5 clusters supported by anatase TiO_2 (101).

The increase in adsorption energy for the charged Ni_5 structure is mostly because of the extra bond formation between the C atom and the top Ni atom of the cluster (Figure 3.8 b). Together with a net spin moment of $2\mu_B$, the net charge on the cluster increases to $-1.708\,|e|$, explaining the stronger bond between the cluster and the (positively charged) C atom of the molecule. The PDOS reveals that upon charging, there is a shift in bonding states of the CO_2 molecule towards the valence band (Figure 3.10 b). This facilitates the hybridization of high-lying CO_2 antibonding π^* orbitals with d orbitals of the cluster. This shift is also seen in CO_2 adsorption on a negatively charged slab of titania, which resulted in improved adsorption energy of the carbonate-like structure.

For the CO_2 adsorption on the negatively charged Cu_5/TiO_2 (Figure 3.8 d), we can see a slightly smaller bandgap (Figure 3.10 d), together with a more extensive hybridization of C states with the cluster d orbitals. By analyzing the spin population and net charge of each atom, together with the morphological changes in the cluster shape upon charging the system, we can see that for the charged configuration, the CO_2 molecule binds only with the metal cluster, in contrast to the neutral case, where CO_2 binds to the interface. This change in adsorption mode is accompanied by a change in the amount of accumulated charge on the CO_2 molecule (from $+0.184\,|e|$ to $-0.268\,|e|$ upon negatively charging the system). The net spin moment remains zero, while the net charge on the cluster increases due to the presence of the excess electron. Considering the unpolarized spin configuration of the cluster, we conclude that the net charge of the cluster is the amount of charge that it shares with the surface as a result of their interaction. Thus, the improved adsorption energy of the CO_2 molecule on negatively charged Cu_5/TiO_2 is actually due to more hybridization of the CO_2 states with cluster orbitals and also stronger interaction of the complex of *cluster* + *molecule* with support's surface (considering that the amount of charge shared between the cluster and the support has been increased).

Table 3.2: Bond lengths and adsorption energies of CO_2 molecules on TiO_2-supported Ni_5 and Cu_5 clusters.

Method	**Structure**	**r(C-O)**	**(OCO)**	$\mathbf{E_{ads}}$ (eV)
DFT	Gas Phase	1.17, 1.17	180	
	Ni_5-Neutral	1.22, 1.27	135.9	-0.53
	Ni_5-Charged	1.26, 1.32	124.2	-2.69
	Cu_5-Neutral	1.25, 1.28	131.0	-0.75
	Cu_5-Charged	1.25, 1.30	125.6	-1.57
DFT+U	Ni_5-Neutral	1.23, 1.27	134.3	-0.31
	Ni_5-Charged	1.26, 1.32	123.7	-2.53
	Cu_5-Neutral	1.25, 1.29	129.5	-0.64
	Cu_5-Charged	1.25, 1.29	125.8	-1.10

By looking into the bond lengths and angles reported in Table 3.2, we can see that the bond length elongation and bending of the O-C-O angle in the Ni_5 case are more sensitive to excess charge than in the Cu_5 case. This agrees with the more stable bent structure of the CO_2 adsorbed on supported Ni_5.

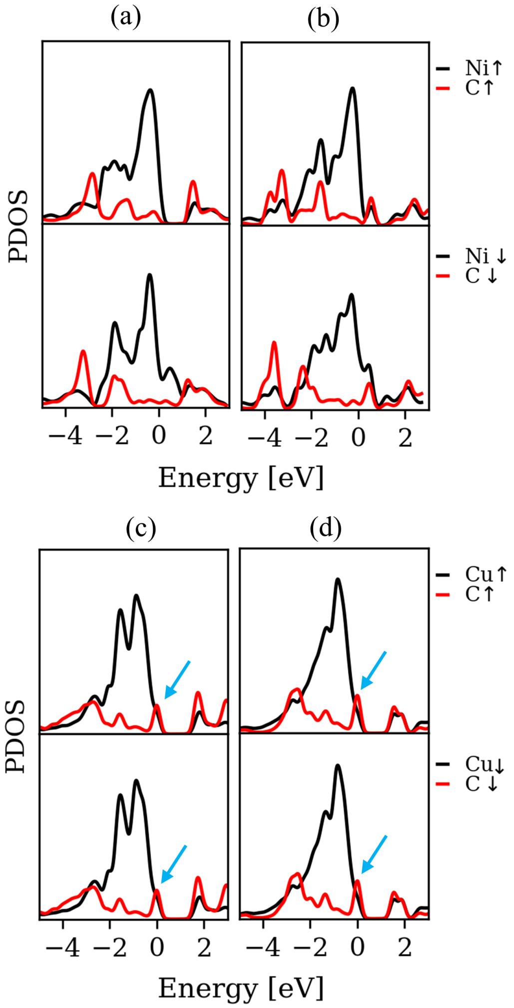

Figure 3.10: Projected density of states for the adsorption of CO_2 molecule on TiO_2 supported: a) Ni_5-neutral, b) Ni_5-charged, c) Cu_5-neutral, d) Cu_5-charged structures.

3.3.4 Dissociated CO_2 on TiO_2, Ni_5/TiO_2, and Cu_5/TiO_2

In plasma catalysis, CO_2 dissociation can occur via several reaction paths. In this work, we focus on the adsorption of CO_2 on neutral and negatively charged surfaces, and not on the actual reaction paths. Hence, these simulations do not aim to identify the most suitable catalyst for CO_2 dissociation, but they provide insight into the effect of surface charging, which is one of the characteristic features of plasma catalysis, distinguishing it from thermal catalysis. In order to estimate the effect of charge on the dissociation of CO_2, we examined various initial configurations of dissociated CO_2 (CO(ads) + O(ads)) on TiO_2, Ni_5/TiO_2, and Cu_5/TiO_2.

For CO_2 dissociation on neutral TiO_2, we did not find a stable structure for adsorbed CO (ads). In most cases, CO either desorbs back in the gas phase or attracts an oxygen atom from the surface and so forms a linear CO_2 molecule. A less stable structure is shown in Figure 3.11 a, in which CO(ads) + O(ads) is obtained. Although the results in Figure 3.12 for dissociation on the bare surface of TiO_2 show an improvement in the adsorption energy due to the presence of the excess electron, dissociative adsorption is thermodynamically unfavorable, regardless of charging. This means that in the absence of a catalyst, dissociation of CO_2 on a bare slab of anatase will not proceed spontaneously. An interesting parallel can be drawn with the effect of vacancies on the reactivity of TiO_2 towards CO_2 activation. Just like the formation of vacancies, electron addition effectively corresponds to a reduction of the TiO_2 surface. In both cases, this reduction has been found to result in improved chemisorption of CO_2. However, vacancies additionally provide a strong binding site for oxygen [118, 120], thus also promoting the dissociation of CO_2 adsorbed on a vacancy; such site is not created upon charging, and CO_2 splitting remains unfavorable.

By employing Ni_5 as a catalyst, we find a dissociative adsorption energy of -0.03 eV for the CO_2 dissociation on the neutral surface (Figure 3.11 c). By adding an excess electron to the system, the adsorption energy significantly increases to -1.85 eV, which makes the reaction thermodynamically highly favorable (Figure 3.11 d).

For the case of neutral Cu_5/TiO_2, dissociation of the CO_2 molecule into adsorbed $(CO)_{ads}$ and $(O)_{ads}$ is slightly endothermic with an adsorption energy of $+0.14$ eV (Figure 3.11 e). Upon negatively charging the system (Figure 3.11 f), the dissociative adsorption energy becomes -0.25 eV, making this reaction thermodynamically favorable. Figure 3.12 shows the corresponding dissociative adsorption energy for each configuration based on DFT and DFT+U calculations.

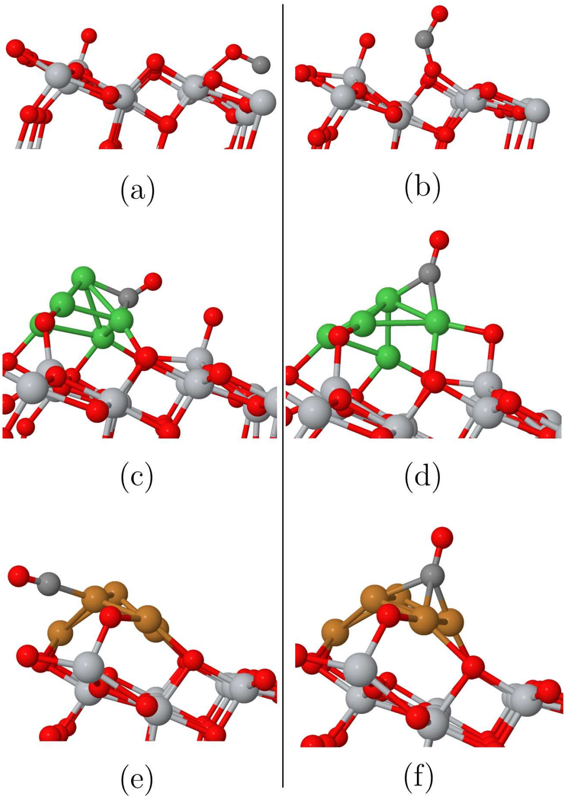

Figure 3.11: The most stable structures for dissociative adsorption of CO_2 (CO(ads) + O(ads)) on a) neutral TiO_2, b) charged TiO_2, c) neutral Ni_5/TiO_2, d) charged Ni_5/TiO_2, e) neutral Cu_5/TiO_2 and f) charged Cu_5/TiO_2.

These results show that the presence of an excess electron positively impacts the stabilization of the dissociated CO_2. This impact is more pronounced in the case of a Ni pentamer as a catalyst, which shows excellent performance in response to the presence of a plasma-induced excess electron and significantly improves the adsorption energy of both adsorbed and dissociated CO_2. Cu_5 adsorbed on a neutral TiO_2 surface is not active enough to dissociate the CO_2 favorably, but it also shows positive feedback to negatively charging the surface. Therefore, these two particular test cases (adsorbed Ni_5 and Cu_5) are good examples of how electrons from a plasma can induce a shift in the chemical properties of different catalysts.

While there are small differences in bond lengths and adsorption energies in the results obtained from DFT and DFT+U, trends regarding the effect of charge on CO_2 activation are the same for both approaches. In addition to comparing the DFT and DFT+U results, we have also investigated the effect of change in surface charge density. We did the same calculations for CO_2 adsorption on pristine titania by using a larger slab (2×4 supercell) of anatase TiO_2 (101) corresponding to a surface charge density of $-0.05\,\frac{C}{m^2}$, which is 2.7 times less than for the small slab. The results indicate that for the large slab, the trends in the effect of charge on stabilization of the bent CO_2 molecule remain the same, although less pronounced (see Appendix 1).

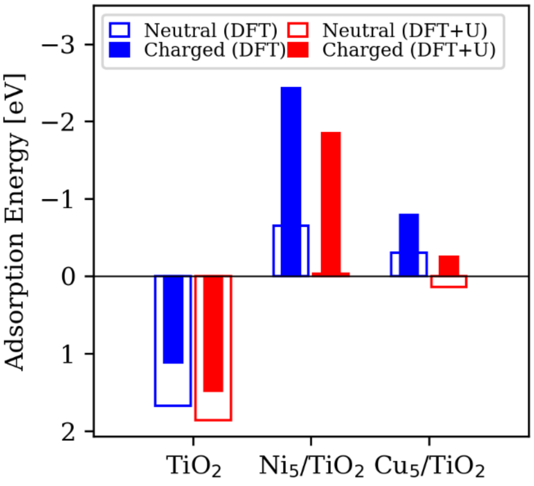

Figure 3.12: Dissociative adsorption energy of CO_2 on bare TiO_2, Ni_5/TiO_2 and Cu_5/TiO_2.

3.4 Conclusion

In this chapter, we investigated the effect of excess electrons induced by plasma on the adsorption properties of Ni_5 and Cu_5 clusters over the anatase TiO_2 (101) surface and also CO_2 activation on both pristine a-TiO_2 and supported clusters.

Adsorption of Ni_5 and Cu_5 clusters on the surface of anatase (101) in the neutral case leads to a charge transfer between the cluster and the support. Depending on the type of catalyst, the direction of charge transfer can be from the surface to the cluster or vice versa. In this case, negatively charging the system leads to minor changes in the stabilization of the clusters. If the excess electron is localized on the surface, it will have a more pronounced impact than when the electron is localized on the cluster. Negatively charging the surface for adsorption of the CO_2 on a bare slab of anatase (101) causes the most stable structure of the CO_2 molecule to change from a linear to a bent configuration. This is mostly because of shifting the high-lying CO_2 antibonding π^* orbitals towards the valence band and facilitating their hybridization with p or d states of the surface.

In the case of employing Cu_5 and Ni_5 nanoclusters, the same result is seen for the improvement of bent CO_2 stabilization, although the underlying mechanisms are slightly different. Upon negatively charging the system in CO_2 adsorption on supported Ni_5, the same shifting in CO_2 high-lying states is seen, which leads to increased hybridization with the cluster d orbitals. In contrast, for the supported Cu_5, changing the adsorption site from the interface to the cluster leads to more stabilization of the CO_2 molecule. This change in adsorption mode results in a significant increase in the negative partial charge of the CO_2 molecule, indicating the activation of the molecule.

The dissociation of CO_2 on a bare slab of anatase titania is thermodynamically unfavorable, regardless of added charge. CO_2 dissociation is favorable on Cu_5 as a catalyst in a charged configuration and on Ni_5 both in neutral and charged configurations. Together with better results for adsorption energies and bond elongation of the CO_2 (ads) in charged configurations, Ni_5 could be a good option for plasma-catalytic CO_2 conversion.

In general, plasma-induced excess electrons alter the adsorption process by shifting the anti-bonding states of CO_2 towards the valence band, increasing the polarization effects and changing the adsorption site of the molecule. These effects consequently lead to improved stabilization of bent (ads) and dissociated CO_2 in negatively charged structures. This can be considered as a possible reason for the synergistic effects observed in plasma catalysis.

Chapter 4

The Synergy Between Electric Field, Surface Morphology, and Excess Electrons[*]

---

[*] This chapter is published as: A. Jafarzadeh et al. “Activation of CO_2 on Copper Surfaces: The Synergy between Electric Field, Surface Morphology, and Excess Electrons,” *J. Phys. Chem. C*, vol. 124, no. 12, pp. 6747–6755, Mar. 2020.

4.1 Introduction

Cu surfaces have been widely used for CO_2 reduction [121–124]. However, it is known that activation and further reduction of CO_2 over Cu surfaces are not straightforward without the help of electro-catalytic conditions, e.g., an applied external potential and corresponding occurrence of electric fields and charges in the electrochemical double layer. For instance, Chernyshova et al. [125] showed that a clean Cu (111) surface in the presence of an aqueous electrolyte is not able to activate CO_2 without the presence of a hydrated Na^+ cation on top of the linear CO_2 molecule. Also, Garza et al. [126] concluded that the formation of a negative carbonate-like structure of CO_2 on Cu (111) in an electrolyte medium is not favorable until the effect of the applied electrochemical potential is accounted for. Indeed, applied potentials can lead to significant changes in the thermodynamics of catalytic reactions: It has been reported that electric fields stronger than 0.1 V/Å can alter the energies of molecular orbitals of adsorbates [127, 128] which in turn leads to changing chemisorption patterns, as well as different activation energies of reactions over metal surfaces.

Although electrochemical systems have shown successful performance towards CO_2 reduction over metal catalysts, accurate simulation of the interface between the electrodes and an electrolyte is highly challenging, mostly because of the existence of the complex electrolyte environment and limitations in applying the electrochemical potential [129]. It is known that explicit approaches used for elucidation of the electrolyte are computationally demanding [130]. On the other hand, it is difficult to assess the accuracy of the description for the solid-liquid interface using implicit methods that treat the electrolyte medium using continuum models [130].

Moreover, in an electrochemical double layer as found in the electrochemical activation of CO_2, many factors potentially contributing to the reaction are simultaneously present (e.g., electric fields, excess electrons, solvent molecules, solvated ions, changes in surface morphology, etc.). As a result, it is very difficult to pinpoint the precise effect of each individual factor or phenomenon or understand if and how any synergies between them can arise. For this reason, it would be useful to alternatively study a pure gas-facing system to focus on the respective roles of the field and excess electrons, and not take any electrolyte into account. Not only does such a set-up dramatically simplify the surface physical chemistry—and thus allow for a more focused exploration of the role of excess electrons and electric fields—but it is also a physically sensible model of certain phenomena arising at a plasma–catalyst interface.

Indeed, as explained earlier, a plasma provides a non-equilibrium and reactive environment for chemical reactions, thanks to the ions, electrons, radicals, and (vibrationally and electronically) excited species present [45]. The plasma can also affect a catalyst, for example by generating strong electric fields near the surface or by depositing excess electrons. In contrast to electrochemical systems, where electric field and charge distributions are intertwined phenomena that directly depend on the applied potential and nature of the electrolyte solution, these effects can vary significantly in plasma setups, which means that a potentially much more diverse chemistry can be accessed [131]. Also, the Debye length in plasmas typically used for plasma catalysis is typically in the order of μm or larger (as opposed to nm in electrochemical systems). Therefore, the electronic effect of the double layer can easily be incorporated in microscopic models in the form of a net charged slab and external electric field without the need to consider solvent molecules or specific microscopic countercharge distributions. Thus, a simple model of a gas-facing catalyst also represents a true physical aspect of a plasma-catalytic setup, besides being of purely theoretical interest.

In Chapter 3, we demonstrated that the presence of excess electrons improves the activation of CO_2 on supported transition metal clusters [132]. However, we did not attempt to disentangle the role of the electric field and the surface charge. In this chapter, we therefore systematically assess the respective contributions of electric fields and excess charges on well-defined catalytic copper surfaces. Moreover, by considering different surface facets, we can also reveal how the morphology of the catalyst controls the response of the surface chemistry to any of these electronic effects.

In this study, we developed methodologies to efficiently study the effect of external electric fields and excess electrons on molecular adsorption. First, we considered the effect of the two different electronic effects in isolation and evaluated the role of the surface structure. Subsequently, we simultaneously considered the electric field and excess electrons, and then we explained how their combined effect could improve the activation of CO_2 over Cu surfaces with different morphologies. Besides its direct relevance to understanding surface chemistry in plasma catalysis, the results also provide fundamental insights into charge-based phenomena found in electrochemical systems.

4.2 Computational details

All calculations were performed on four different Cu surfaces ((111), (211), (110) and (001)) by means of DFT calculations. A lattice constant of 3.615 Å [133] was used for making the slabs. The (111), (110), and (211) surfaces consist of four atomic layers, while we chose five layers for the more compact structure of (001). Further details, including dimensions of the supercell used for each slab, are provided in Appendix 2.

The Quickstep [102] module of the CP2K [103] package was used for all calculations, employing molecularly optimized (MOLOPT) [104] double-ζ valence plus polarization (DZVP) basis sets, together with an auxiliary plane-wave basis set with 800 Ry cutoff for the expansion of Kohn-Sham orbitals. Electron exchange and correlation effects were dealt with using the GGA-PBE functional [73], while applying Grimme's D3 approximation together with Becke-Johnson damping for dispersion corrections [68, 69]. Inner shell electrons were taken into account by using Goedecker-Teter-Hutter (GTH) pseudopotentials [105, 106], while for the upper shell electrons of Cu, C, and O we considered 11, 4 and 6 valence electrons, respectively. Geometry optimizations were performed using the Broyden-Fletcher-Goldfarb-Shanno (BFGS) scheme with a maximum relaxation force tolerance of 0.02 eV/Å between atoms. Partial charges on atoms were calculated using the Hirshfeld-I scheme [107] as implemented in CP2K. We performed test calculations both with k-point sampling of the Brillouin zone by using 4 × 4 × 1 Monkhorst-Pack mesh [134] and k-point sampling which was limited to the Γ–point only. We found that sampling with the Γ–point is significantly faster compared to k-point sampling with $4 \times 4 \times 1$ Monkhorst-Pack mesh, while there are only minor differences in adsorption energies and all the trends are maintained. We therefore carried out the calculations considering sampling of the Brillouin zone restricted to the Γ–point only. Full periodic calculations were performed along the surface (only X and Y directions) in order to avoid unrealistic interactions with replicated pictures along the Z direction [87].

In order to compare Cu (111) (with a thickness of 6.26 Å) to Cu (110) (with a thickness of 8.77 Å) surfaces, we used Dirichlet boundaries to apply a $15\,V$ potential difference on the electrodes, resulting in different electric field strengths for each slab ($1.08\,V/$Å for Cu (111) and $1.31\,V/$Å for Cu (110)). Making the same comparison using charged plates with applying a charge density of $0.089\,\frac{C}{m^2}$ on the dipole sheets, we get the same electric field strength for both surfaces ($1.00\,V/$Å for Cu (111) and $1.01\,V/$Å for Cu (110)). In other words, using a fixed setup in the case of the Dirichlet boundaries results in different external field strength when applied to different slabs, which must be accounted for when comparing different surface morphologies. For methodological consistency, we have opted to use the same electrode settings for all considered surface slabs in all further calculations using Dirichlet boundaries. The main disadvantage of the method is that it is not possible to combine the electric field effect with the effect of excess electrons since the method assumes charge neutrality.

Despite these differences between both approaches, we can obtain equivalent results using both methods if we correct the different slab size dependencies of both methods; details of this cross-checking are provided in Appendix 2 (Figure A2.1). Adsorption energies are achieved by subtracting gas-phase CO_2 and bare slab total energies from the complex (surface + adsorbed molecule) total energy. To be consistent with the experiments, we have considered CO_2 in gas-phase without the presence of an electric field while considering the energies of the bare slab and complex in the presence of an electric field. In this case, the CO_2 molecule is initially outside of the area influenced by the field and by entering the area between the electrodes, it is affected by the applied electric field while approaching the surface. Deshlahra et al. have used the same approach for the study of CO chemisorption on Pt (111) in the presence of a uniform electric field [135].

4.3 Results and discussion

Here, we first report on the calculations using constant potential electrodes, which aim to investigate the effect of an external electric field on bare Cu surfaces and their ability to adsorb CO_2. Next, we will briefly report on the effect of net charges without the presence of an external electric field. Finally, we will discuss the combined effect of electric field and excess electrons on the redistribution of surface charges on pristine Cu surfaces and on CO_2 chemisorption patterns, as obtained from the modified dipole sheet method calculations.

4.3.1 Electric field effect using constant potential electrodes

CO_2 adsorption on all Cu surfaces is studied first without an applied potential and then compared with the results obtained in the presence of a negative electric field. The applied voltage range is between 0 and $25\,V$. Note that extreme potentials over $25\,V$ lead to very strong electric fields, such that CO_2 gets dissociated and attached to the upper electrode, which results in unphysical energies. Also, in most cases above $25\,V$, Cu atom detachment from the surface was seen as a result of 'field-evaporation'. This effect has already been reported as the detachment of single atoms and even clusters from metal surfaces in response to applying very strong electric fields [136, 137].

Electric field effect on bare surfaces

We started with applying a potential on the upper electrode while keeping the lower electrode at zero potential to see how this changes the electrostatic potential inside the simulation box for bare Cu surfaces. As expected without the applied electric field, the potential rapidly falls to zero after a short distance from both sides of the surfaces. In this case, negative partial surface charges of the top and bottom layers are present, showing a slight charge accumulation over the surfaces of the metal slab. After applying an electric field to the bare surface, the charge distribution inside the surface changes in a way that leads to a migration of negative charge from the bottom to the above layers of the slabs (opposite to the electric field direction). The linear relationship between the electric field strength and the charge separation over the top and bottom layers of the surface is shown in Appendix 2. (Figure A2.2). The slope of the potential in both the upper and lower sides of the metal surface resulted in the same electric field strength, considering the zero-field inside the conductor slab (Figure A2.3). This is in excellent agreement with the potential distribution reported by Deshlahra et al. [135].

Electric field effect on CO_2 adsorption

Without the presence of an applied electric field, CO_2 does not chemisorb on Cu surfaces, no matter how rough the surface is. In all cases without applied electric field, physisorbed CO_2 is the most stable structure on the Cu surfaces, which is consistent with the literature [138–140]. Corresponding adsorption energies and bond lengths and angles for CO_2 adsorption on Cu surfaces upon changing the applied potential are shown in Appendix 2. (Table A2.3 - Table A2.6).

On Cu (111), physisorption remains the most stable mode until the applied electric field reaches a value of around $1V/\text{Å}$, where chemisorption becomes the favored mode. Figure 4.1 shows the most stable adsorption mode of CO_2 on the Cu surfaces as a function of the potential applied to the upper electrode. For the $\Delta V = 15\ V$ case, the slight increase in adsorption energy is due to the improved Coulomb interaction between the carbon atom of the slightly bent molecule and the negative surface charge. Bending of the molecule is a natural result of the force applied to the positive carbon atom towards the electric field, while pushing negatively charged oxygen atoms in the opposite direction.

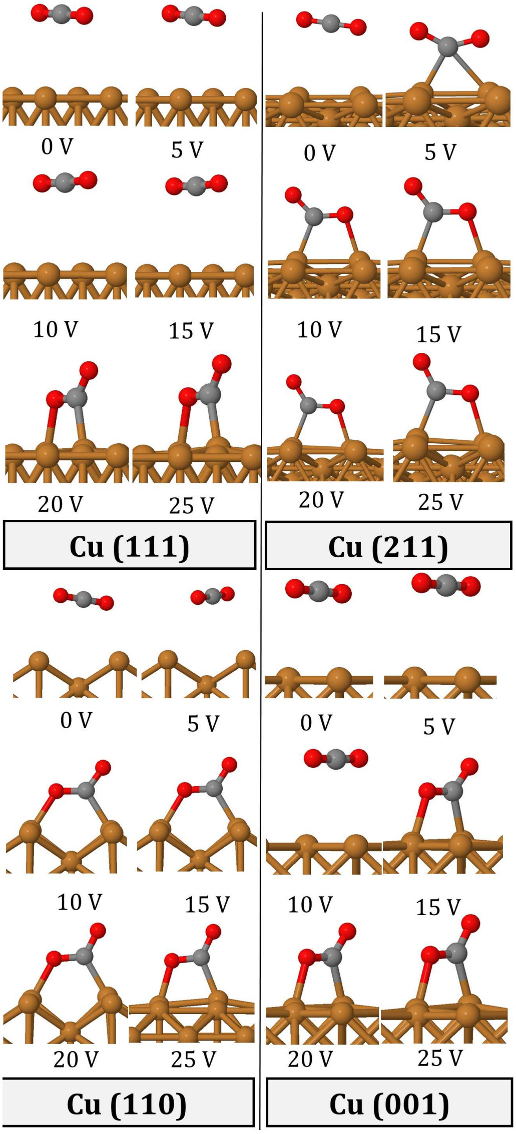

Figure 4.1: The most stable CO_2 adsorption mode on Cu surfaces for different applied potentials.

Once the adsorption mode changes from physisorption to chemisorption, there is a dramatic change in the adsorption energy and C-O bond elongation, together with a decrease in the O-C-O angle, which all point to CO_2 activation. We have also studied the change in accumulated charge of the molecule as a result of increasing the applied potential. Figure 4.2 shows a linear relationship between the strength of the applied electric field and the increase in the accumulated charge on the adsorbed CO_2 over all Cu surfaces.

Note that considering the different thicknesses of the slabs, the applied voltages will lead to slightly different external electric fields at the slab surface. This is shown in Figure 4.3 and Figure 4.4. Even though the applied potential is the same, the strength of the electric field is different for each slab configuration.

On Cu (211), as one of the rough surfaces that we have considered, CO_2 chemisorbs weakly with an adsorption energy of -0.33 eV when applying a potential of $5\,V$ (equivalent to $0.41\,V/Å$ electric field strength) (see Figure 4.3 and Figure 4.4). By increasing the applied potential, the adsorption energy increases together with a greater C-O bond elongation and accumulated charge compared to the Cu (111) surface. As shown in Figure 4.4, at the voltage of $25\,V$, corresponding to an electric field of $1.94\,V/Å$, a strong adsorption energy of -1.96 eV is found together with the longest C-O bond length and smallest O-C-O angle.

CO_2 adsorption patterns over Cu (110) are more or less similar to the (211) case except that the physisorption-to-chemisorption transformation occurs after applying a somewhat larger potential to the system. As shown in Figure 4.1, CO_2 prefers a long-bridge site for chemisorption for the applied voltage range of 5 to $20\,V$. However, for $\Delta V = 25\,V$ we found the most stable chemisorbed CO_2 on a short-bridge site. From Figure 4.4, it can be seen that at $25\,V$ applied potential, the adsorption energy is the same as on the Cu (211) surface, consistent with the observed bond elongation and increase in negative partial charge of the molecule.

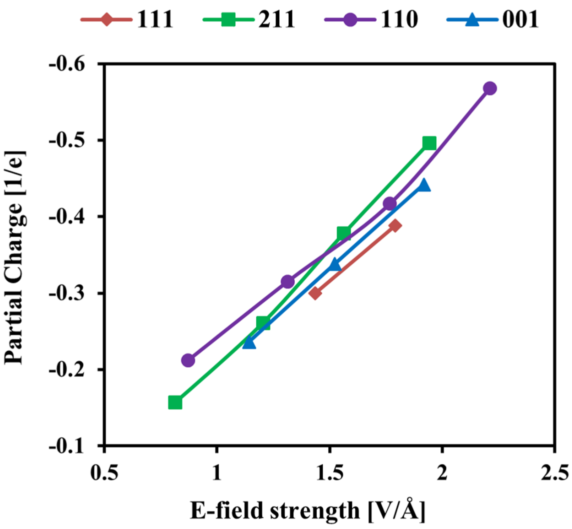

Figure 4.2: Partial charge of the adsorbed CO_2 versus electric field strength.

The Cu (001) slab shows a stronger response to the electric field towards CO_2 chemisorption in comparison to the other flat surface (Cu (111)). In the presence of an applied electric field, chemisorbed CO_2 is more stable on (001) surfaces than on (111). This higher sensitivity is also seen in the larger partial charge accumulation on the CO_2 molecule due to the presence of the electric field (Figure 4.2). The projected density of states (PDOS) of both slabs reveal the underlying reason for the difference in performance. Only strong electric fields lead to a very small shift in the surface *d* states towards the valence band. However, this shift is more pronounced in the molecules *s* or *p* states. Figure 4.5 and Figure 4.6 show the PDOS of both surfaces upon changing the applied potential. As indicated by the blue arrows, shifting of the C and O states for the CO_2 adsorbed on (001) surface is more pronounced compared to the (111) slab. This increased shift leads to enhanced hybridization between the molecule and the metal surface states. This can also apply to the observed change in the performance of Cu (211) and Cu (110) surfaces. More details on the bonding properties between CO_2 and Cu atoms are provided in Appendix 2.

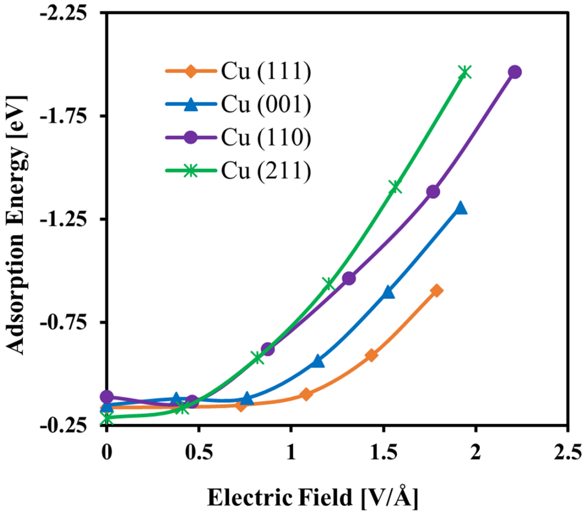

Figure 4.3: Adsorption energy of CO_2 over Cu surfaces as a function of the electric field strength between both electrodes.

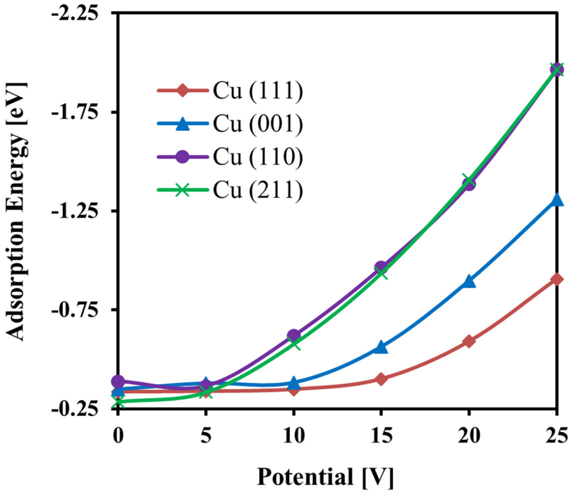

Figure 4.4: Adsorption energy of CO_2 over Cu surfaces as a function of the applied potential between both electrodes.

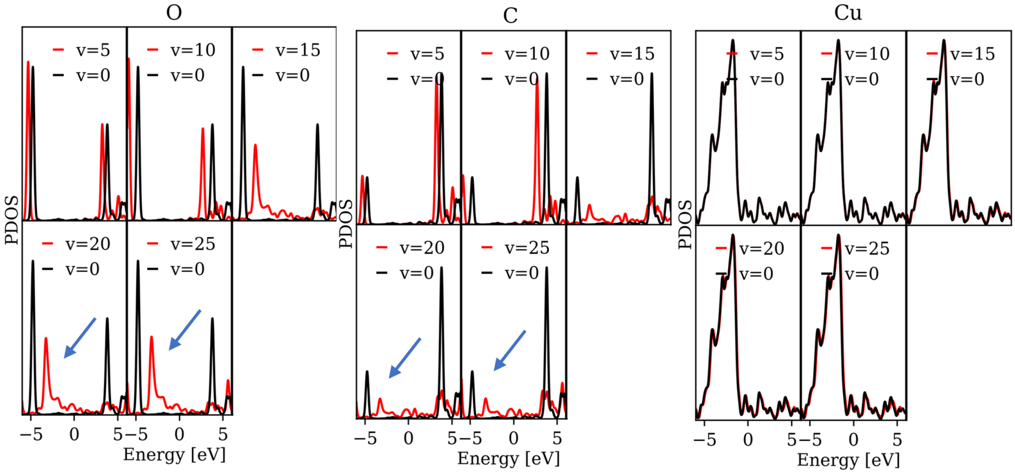

Figure 4.5: Projected density of states for CO_2 adsorption on Cu (001).

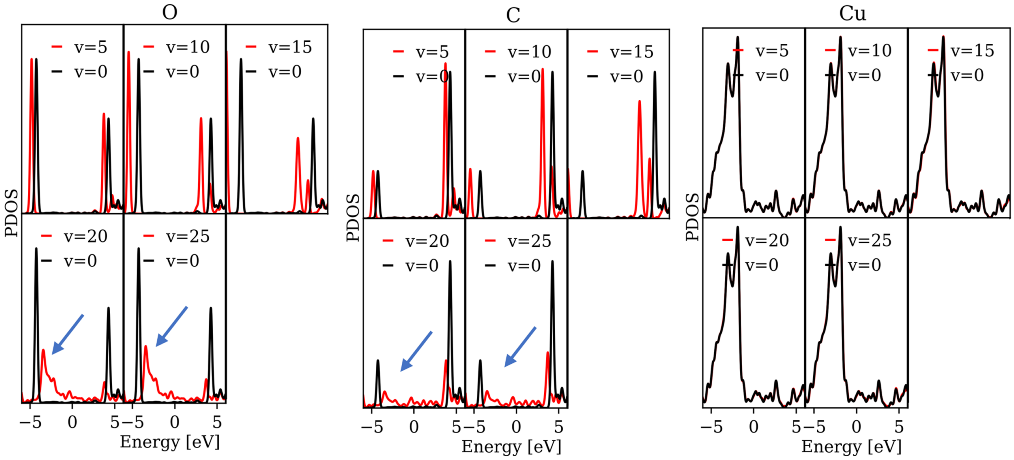

Figure 4.6: Projected density of states for CO_2 adsorption on Cu (111).

In summary, the results indicate that a negative electric field has a strong impact on the adsorption of CO_2 and more specifically on its chemisorption as the first step towards activation. The rougher surfaces respond more strongly to the electric field. This is partially because of the local electric field enhancements as a result of morphological differences. Also, lower coordinated atoms in rougher surfaces, like (211) and (110), are more prone to make a stable bond with CO_2 than the highly coordinated Cu atoms in flatter surfaces.

4.3.2 Excess electron effect on CO_2 adsorption patterns

To make a consistent comparison between the individual effect of each parameter and the combined effects, we also need to consider the presence of excess electrons only, without any external electric field applied to the system. In this case, we first optimized the CO_2 adsorption (using both initially physisorbed and chemisorbed configurations) on all surfaces without any charge or electric field applied. Then we re-optimized the most stable structure by adding one electron to the supercell. We found that the lone added charge is evenly distributed on both sides of the slab, as expected from electrostatic theory, and does not lead to any noticeable change in the adsorption energy of the molecule. In all cases, the re-optimized structure with the excess electron has almost the same stability as the neutral structure (with differences in adsorption energies less than 0.02 eV, as shown in Figure 4.7).

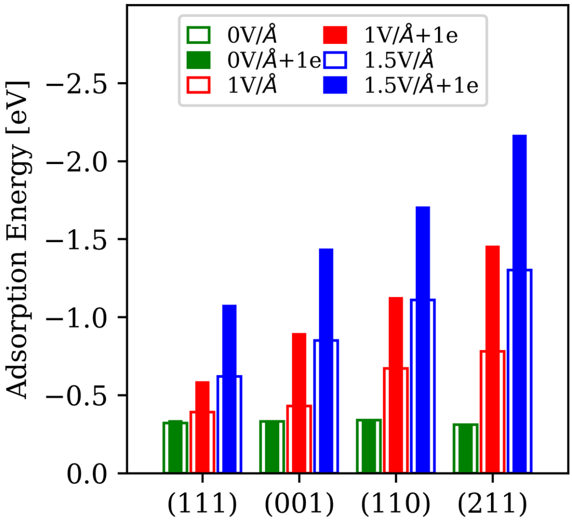

Figure 4.7: Adsorption energy of CO_2 on Cu surfaces as a function of both electric field and excess electrons.

For the Cu (110) surface without excess electron, the most stable structure is the linear physisorbed CO_2. This is also the case on the other surfaces. Once the excess electron is added, chemisorption becomes the most stable adsorption mode, although the adsorption energy increases as 0.01 eV. In other words, on the negatively charged Cu (110) surface, the physisorption mode is less stable than the chemisorption mode, in contrast to the neutral case. For all the other surfaces, the most stable neutral and re-optimized charged structures are linear physisorbed CO_2. These results show that without an external electric field, the presence of excess electrons has a negligible effect on the adsorption properties of CO_2 on the Cu surfaces studied here. This is in line with recent findings within our group PLASMANT, for CO_2 chemisorption on charged semiconductors; there, the adsorption enhancement due to the presence of excess electrons is linearly correlated with the work of charging or, more generally, the band gap [141]. As a result, the chemistry on metallic surfaces can also be expected to be mostly unaffected by negative charging.

4.3.3 The combined effect of electric field and excess electrons using the modified dipole sheet approach

We have devised a modified version of the dipole sheet approach to be able to explain the combined effects occurring in plasma catalysis as a result of an electric field and plasma-induced excess electrons. As in the previous section, we first study the combined effects on bare surfaces and then extend it to the adsorption of CO_2 over Cu surfaces.

The combined effect on bare surfaces

Using a dipole sheet induces a uniform electric field between the plates independent of the thickness of the employed metal surface. This is different from the constant potential electrodes approach in which the electric field strength varies with the size of the vacuum area between electrodes (which changes when metal surfaces with different thicknesses and morphologies are placed between the electrodes). In order to apply the intended electric field between the dipole sheets, the electric charge on the plates should be adjusted. Table A2.1 and Table A2.2 in Appendix 2 show values for charge and surface charge density for the corresponding strengths of the external electric field.

When we add an excess electron to the system and simultaneously apply the electric field, the distribution of the electrons on both upper and lower surfaces of the slab will change. This leads to altered electric fields in the regions on the top and bottom of the metal slab, as seen from the difference in slope of the potential in cases with the combined effect of electric field and excess electron in the upper and lower regions of the slab (Figure A2.8). Also, it is seen that the presence of an excess electron increases the accumulated partial negative charge on both sides of the slab (Figure A2.9). This makes the upper layer more negative and the bottom layer less positive, which in turn increases/decreases the electric field strength in the upper/lower vacuum regions of the metal slab. This effect is more pronounced by using a stronger electric field, which increasingly leads to charge separation on both sides of the slab.

The combined effect on CO_2 adsorption

In order to study the combined effect of electric field and plasma-induced excess electrons on CO_2 adsorption over Cu surfaces, we employ two electric field strengths ($1V/Å$ and $1.5V/Å$), both with and without adding an excess electron, and we compare the results. In the presence of the electric field only, the results are entirely in agreement with the results achieved by the constant potential electrode approach. The most stable configurations for CO_2 adsorption over Cu surfaces in the presence of combined electric field and excess electrons are provided in Appendix 2 (Figure A2.4 – Figure A2.7). For the case of Cu (111), $1V/Å$ electric field (without adding an excess electron) is not sufficient to induce chemisorption (Figure A2.4), whereas chemisorption is the most stable adsorption mode under the examined circumstances for all the other surfaces, as shown in Figure A2.5 – Figure A2.7.

Adding one excess electron to the system and applying the electric field gives rise to CO_2 creating a stable chemisorbed state on Cu (111) and more stabilization of previously formed chemisorbed structure on the three other surfaces. A careful analysis of the partial charges on the atoms involved in bonding (provided in the Appendix 2 - Table A2.11 - Table A2.14) shows that once chemisorption occurs, the Cu atom coordinating with the C atom of the molecule attains a noticeable partial charge. At the same time, there is only a marginal change in the partial charge of the other neighboring Cu atoms. This leads to forming a polar covalent bond, where the positive partial charge is located on the C atom. This is the opposite for the Cu atom, which makes a bond with the O atom of the molecule. In this case, the previously negatively charged Cu atom loses all its negative charge to the bonded oxygen atom and becomes slightly positive. The other oxygen atom of the molecule gets a pronounced partial negative charge, which indicates the further activation of the molecule.

In all cases, adding an excess electron leads to an enhancement of the electric field effect, correspondingly giving rise to an increase in adsorption energy and C-O bond stretching and a decrease in the O-C-O bond angle. The trends in adsorption energy are shown in Figure 4.7. The combined effect of an electric field and excess electrons on the partial charges of the CO_2 molecule are shown in Figure 4.8. We obtain more or less the same results for the $\frac{1V}{\mathring{A}} + 1e$ and $\frac{1.5V}{\mathring{A}}$ cases, which implies that by combining the excess electrons with the electric field yields the same results towards CO_2 activation as a 50% stronger field.

As already seen in the previous section, Cu (211) shows the strongest binding ability amongst the four different slabs studied here. The same reasoning for the improved CO_2 activation can be used here, which stresses the important role of the surface morphology in response to the charge and electric field effect. By analyzing the PDOS (provided in Appendix 2; Figure A2.10 – Figure A2.13), the same shift in s and p states of the CO_2 molecule resulted from applying an electric field and excess electrons is seen. By slightly shifting the metal's d states around the Fermi level, the increased accumulated negative charge on the upper layer of the slab also helps further mixing between the surface and the molecule's states. The more negatively charged the surface is, the stronger the bond it makes with the positive carbon atom of the molecule. In this situation, the repulsion between the negatively charged surface and the reduced oxygen atoms leads to further bending of the molecule. As shown in Figure 4.8, improved bent structures are accompanied by an increased accumulated partial charge on the

CO_2 molecule.

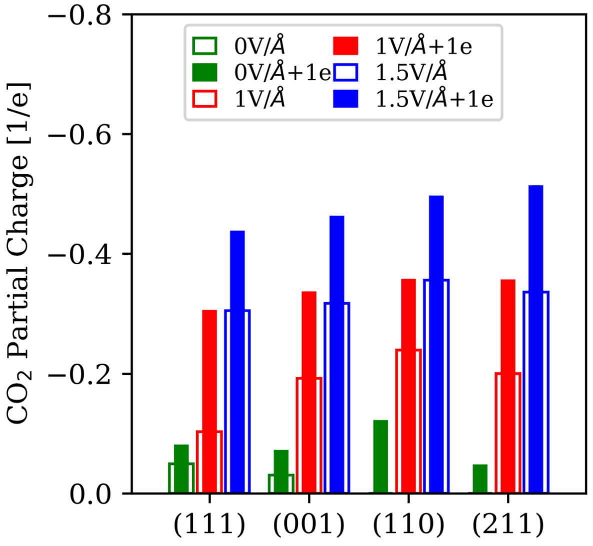

Figure 4.8: Partial charge of adsorbed CO_2 over different Cu surfaces.

Improved CO_2 activation due to the increased electric field (obtained by the combination of electric field and a plasma-induced excess electron) suggests that the electric field enhancement could be the key factor leading to the higher CO_2 conversion rates in plasma catalysis. In other words, fine-tuning the surface morphology of the catalyst together with the presence of excess electrons could be employed to adjust the required electric field strength aiming for higher conversion rates.

These results also help to explain the role of excess electrons in electrochemical CO_2 reduction. Our initial results for the isolated effect of electric fields or excess electrons seem to suggest that the primary contributor to CO_2 chemisorption is the electric field, so that the only role of the excess electrons is that of a charge carrier needed to obtain the applied potential drop. However, whenever an electric field is present, the electrons on the surface will also play a chemical role, meaning that both have a direct effect on the chemistry. Due to the nature of electrochemical systems, with the applied potential drop within an electrolyte intertwining the two phenomena, such synergistic behavior is always present; it is only through the simplified systematic approach in our study that this precise entanglement can be characterized.

4.4 Conclusion

In this chapter, we investigated the effect of an electric field, excess electrons, as well as the combination thereof, on CO_2 adsorption over Cu surfaces. We used a new technique based on charged parallel plates, which enabled us to analyze the combined effect of the electric field and excess electrons in a plasma-catalytic system for the first time. The results of this study reveal that an external negative electric field induces a switch from physisorption to chemisorption of the CO_2 molecule on Cu surfaces. This effect is even stronger when an excess electron is present in the system. In contrast, excess electrons without an external electric field have no appreciable effect on CO_2 binding. Overall, an increase in adsorption energies, partial charges, and C-O bond elongations in CO_2 are seen due to applying the electric field with or without the presence of excess electrons.

We notice that the rougher surfaces respond more effectively to the presence of the electric field and excess electrons, which we attribute to the locally stronger fields and lower coordinated surface atoms in comparison to the highly coordinated atoms in flat surfaces.

Considering the various synergies that arise through the combined effects, controlling the surface roughness, charge deposition, and electric field strength could be effective parameters to tune and optimize the CO_2 activation process on Cu surfaces.

Chapter 5

Plasma-Catalytic Ammonia Reforming of Methane over Cu-based Catalysts for the Production of HCN and H_2 at Reduced Temperature [*]

---

[*] This chapter is adapted from the manuscript: Yi, Y.; Wang, X.; **Jafarzadeh, A**.; Wang, L.; Yan, J.; Zhang, R.; Zhang, H.; Guo, H.; Neyts, E. C. and Bogaerts, A.” Plasma-catalytic Ammonia Reforming of Methane over Cu-based Catalysts for the Production of HCN and H_2 at Reduced Temperature”- *ACS Catalysis* - Yi, Y; Wang, X and **Jafarzadeh, A** contributed equally to this work as co-first author.

5.1 Introduction

Hydrogen cyanide (HCN), an important chemical featuring the C≡N functional group, is widely used in medicine, metallurgy, pesticide production, fuels, and polymers [24, 25]. Driven by the demand for plastics and polymers, such as nylon and plexiglass in the 1950s, *BASF* corporation created the first facility for industrial production of HCN. The annual production of HCN in 1956 was only 2,400 tons, but it has increased to more than 100,000 tons/year today [24], mainly through the Andrussow process or the BMA process.

As stated earlier in Chapter 1, although both the abovementioned processes have been used in industrial HCN production for many decades, research is still being conducted on optimizing the reaction conditions [142, 143] and uncovering the mechanism of C-N coupling over Pt and Pt-Rh catalysts [144–148]. To our knowledge, there are currently no methods available to synthesize HCN at temperatures below $1,300 - 1,400$ K for the Andrussow process, and below $1,600$ K for the BMA process.

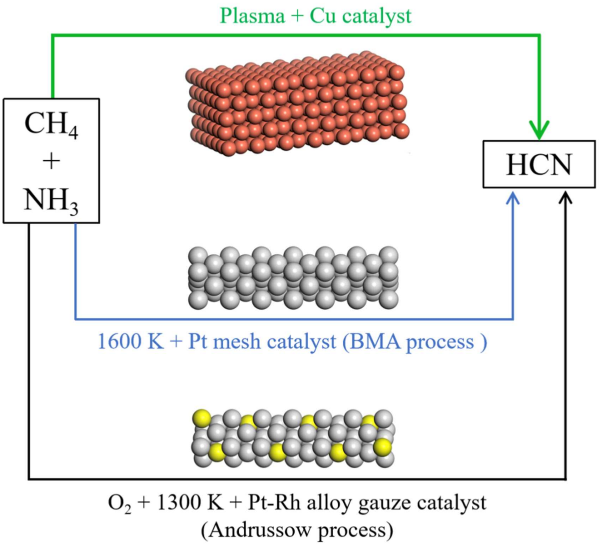

Figure 5.1: Schematic diagram of the classical methods for HCN synthesis and the novel plasma-catalytic method presented in this work.

The non-equilibrium character of non-thermal plasmas (NTP) offers a unique approach to enable thermodynamically unfavorable chemical reactions at low temperature [20, 149, 150]. The gas temperature in such a plasma can be maintained even as low as room temperature. The generated electrons, however, are highly energetic with a typical energy of $1-10\ eV$. Therefore, these energetic electrons can activate reactant molecules (e.g., CH_4 and NH_3) into reactive species, i.e., radicals, excited atoms and molecules, and ions, which can easily trigger chemical reactions at room temperature.

Inspired by the catalytic activity of Pt for HCN production (both in the Andrussow process and BMA process), plasma-catalytic HCN synthesis has been studied by combining supported Pt catalysts with CH_4/NH_3 NTP [151]. HCN was produced from a CH_4/NH_3 mixture at reduced temperatures, reaching 26% CH_4 conversion and 81% HCN selectivity when using optimized catalysts, i.e., Pt/TS-1 catalyst. However, this Pt/TS-1 catalyst is extremely expensive. Therefore, it is economically interesting to examine possible cheaper catalysts using non-noble metals and low-cost supports for the practical application of plasma-catalytic HCN synthesis.

In this chapter, along with some of the experimental results provided in Appendix 3, we report our performed DFT calculations to uncover the reaction mechanisms toward the plasma-assisted production of HCN and H_2. More specifically, we show how the presence of plasma-generated radical species can change the reaction mechanism for plasma catalysis when it is compared to the traditional thermal catalysis.

5.2 Computational details

Fully periodic DFT calculations were conducted using the Quickstep [102] module of the CP2K [103] package, similar to the previous chapters. The GGA-PBE functional [73] was used by employing DZVP-MOLOPT [104] basis sets and GTH pseudopotentials [105, 106]. Dispersion corrections were considered by applying Grimme's DFT-D3 approximation alongside Becke-Johnson damping [68, 69]. A lattice constant of 3.615 Å [133] was used for making four-layered Cu (111), Cu (200), and Cu (220) slabs with the two bottom layers fixed to their bulk structures. The supercell dimensions chosen for each slab are provided in Appendix 3. Fermi-Dirac smearing with the electronic temperature of 300 K was used for the calculations, and sampling of the Brillouin zone was limited to the Γ point only.

For the geometry optimization of the endpoints for the MEP calculation, the Broyden-Fletcher-Goldfarb-Shanno (BFGS) scheme was used by applying a maximum force tolerance of 0.02 $eV/\text{Å}$ and employing an energy cutoff of 800 Ry for the auxiliary plane-wave basis set.

The energy profiles and activation energies were obtained using the climbing image nudged elastic band (CI-NEB) [83] method implemented in the CP2K code. Depending on the distance that atoms needed to travel, between 9 and 28 images were interpolated along the path. The transition state was identified as the highest point between two minima in the energy profile. The plane wave cutoff energy was set to 400 Ry for the NEB calculations.

For most of the exothermic reactions, no saddle point was detected along the reaction coordinate. Consequently, the reaction barrier was reported as zero (barrier-less) for these reactions. For the endothermic reactions without a detected transition state, the reaction energy is reported.

5.3 Results and discussion

In order to understand how the plasma-induced radicals detected by OES contribute to the plasma-catalytic conversion process, and thus to understand why the plasma activates the catalytic process, we performed dispersion-corrected DFT calculations to find the minimum energy path (MEP) for the reactions of N, NH, CH and NH_2 to produce HCN on various Cu surfaces. Based on the surface morphology seen in the XRD patterns (Figure A3.3 a), we selected Cu (111), Cu (200), and Cu (220) slabs for the calculations. In contrast to thermal catalysis, where the reactions typically occur via the Langmuir-Hinshelwood (LH) mechanism [152], in plasma catalysis, both Eley-Rideal (ER) and LH mechanisms can occur [94] and depending on the mechanism to proceed, the reaction barrier will be different. In Figure 5.2, we summarize the elementary steps of

C-N coupling, as well as the formation of hydrogenated intermediates and their dehydrogenation to HCN, considered in our calculations, occurring through both ER and LH mechanisms.

Table 5.1: Calculated activation energy of the elementary steps of C-N coupling, the formation of hydrogenated intermediates and their dehydrogenation to HCN through ER and LH mechanisms, as well as for the desorption of HCN and H_2, on Cu (111), (200) and (220) crystal planes. The values in parentheses are reaction energies instead of activation energies. All values are in eV.

No.	**Reaction**	**Cu (111)**	**Cu (200)**	**Cu (220)**
1	N (s) + CH (s)→ HCN (s)	0.78	0.75	0.62
2	N (g) + CH (s)→ HCN (s)	0.00	0.00	0.00
3	N (s) + CH (g)→ HCN (s)	0.00	0.00	0.00
4	HCN (s) → HCN (g)	(0.83)	(0.70)	(0.88)
5	NH (s) + CH (s) → HCNH (s)	0.45	0.50	0.72
6	NH (g) + CH (s) → HCNH (s)	0.00	0.00	0.00
7	NH (s) + CH (g) → HCNH (s)	0.00	0.00	0.00
8	HCNH (s) → HCN (s) + H (s)	1.38	1.32	1.48
9	NH_2 (s) + CH (s) → $HCNH_2$ (s)	1.20	1.60	1.54
10	NH_2 (g) + CH (s) → $HCNH_2$ (s)	0.00	0.00	0.00
11	NH_2 (s) + CH (g) → $HCNH_2$ (s)	0.00	0.00	0.00
12	$HCNH_2$ (s) → HCNH (s) + H (s)	1.27	1.25	1.30
13	H (s) + H (s) → H_2 (g)	1.01	0.91	0.89

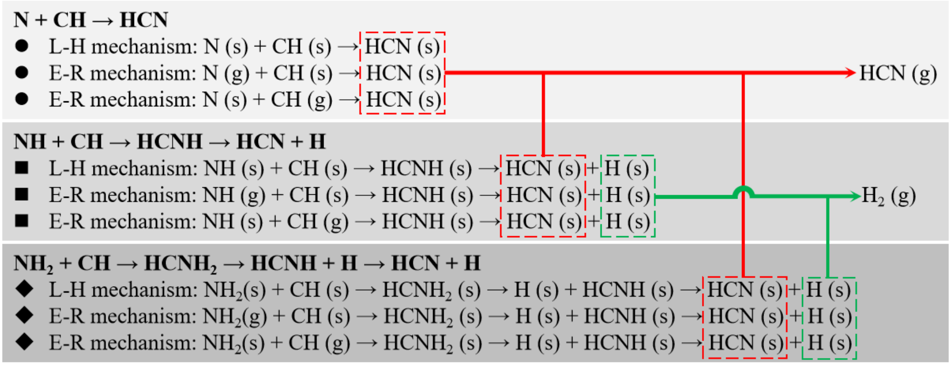

Figure 5.2: Elementary steps of C-N coupling, hydrogenated intermediates' formation, and their dehydrogenation to HCN through ER and LH mechanisms considered in our calculations.

The activation energies calculated for these reactions are listed in Table 5.1. The values in parentheses represent the reaction barriers for these endothermic reactions, in which no saddle point is detected along the path. The equilibrium bond lengths calculated for HCN in the gas phase (C-N: 1.158 and C-H: 1.074) are in good agreement with experimental and theoretical data [153, 154].

For direct C-N coupling – one of the critical steps in HCN synthesis – we see that the reactions happening via the ER mechanism are barrierless, thanks to the high reactivity of the plasma-generated radicals. For instance, Figure 5.3 shows the interaction of N and CH to form HCN via both LH and ER mechanisms (reactions 1, 2, and 3) on the Cu (111) surface (corresponding to the highest intensity in the XRD patterns of Figure A3.3 a). The LH interaction of pre-adsorbed N(s) and CH(s) (reaction 1) exhibits a reaction barrier of 0.78 *eV* towards the formation of HCN (Figure 5.3 a).

Figure 5.3 b and c show the same reaction via both ER mechanisms (reaction 2 and 3). In this case, the energy of the initial gas-phase radicals is much higher, so the whole configuration is highly unstable, representing the non-equilibrium nature of the plasma-catalytic system. As shown in Figure 5.3 b, N is initially in the gas phase and approaches the pre-adsorbed CH(s). At the C-N distance of around 3.47 Å, N(g) enters the reaction channel and the energy of the system decreases steeply.

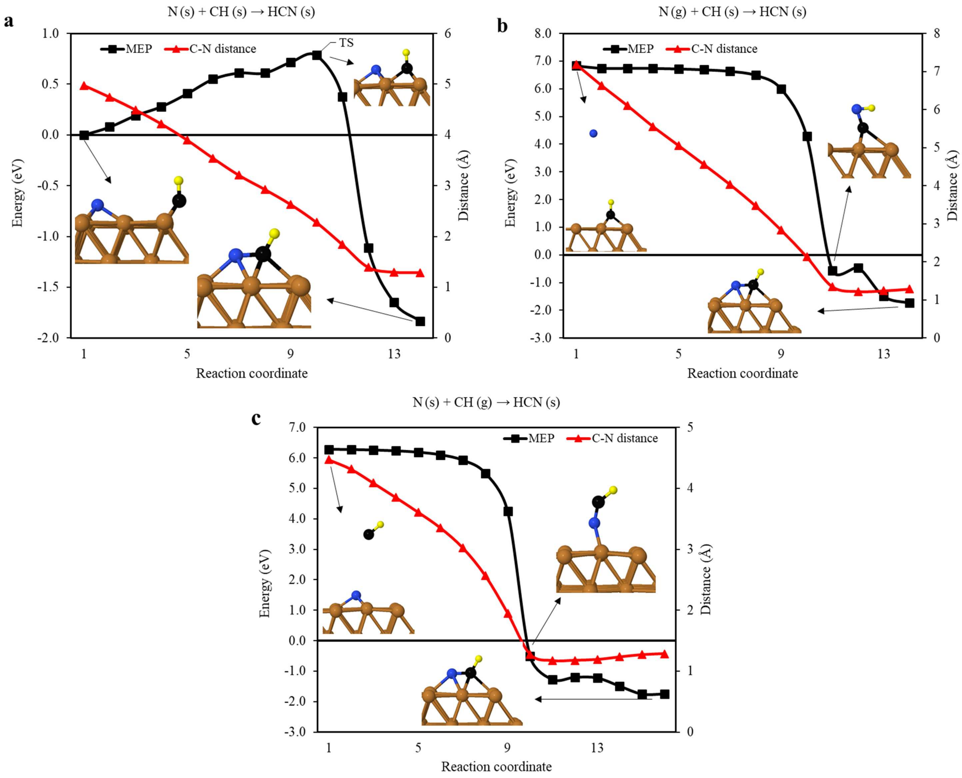

Figure 5.3: Minimum energy path (MEP; black curve, left y-axis) and C-N distance (red curve, right y-axis) for the interaction of pre-adsorbed N and CH (a), gas-phase N with pre-adsorbed CH (b), and gas-phase CH with pre-adsorbed N (c) to form HCN(s) on the Cu(111). The insets illustrate the configurations of the initial state, transition state (TS), and final state, where brown, black, blue, and yellow colors correspond to Cu, C, N, and H atoms, respectively.

The same happens to the alternative ER pathway, starting with gas-phase CH interacting directly with pre-adsorbed N(s) (Figure 5.3 c). CH(g) experiences the van der Waals attraction at a C-N distance of around 3.02 Å, and the gas phase radical falls into the lower energy levels towards coupling with N. We observed the same pattern for all the reactions occurring through the ER mechanism on all three Cu surfaces, which emphasizes that the C-N coupling reactions containing gas-phase radicals can easily happen via this mechanism, without the need to overcome any reaction barrier (see Figure A3.5 and Figure A3.6 in Appendix 3 for reactions 5, 6, 7 and 9, 10, 11 taking place on the Cu(111) surface).

These results are consistent with the OES spectra presented in Appendix 3, showing the disappearance of the excited species with the Cu/S-1 catalyst packing (Figure A3.4). The highly reactive N, NH, NH_2, and CH radicals created in the plasma either interact directly with pre-adsorbed species or adsorb on the Cu surface, to be involved in LH reactions. The barrierless C-N coupling via the ER mechanism can explain why HCN formation can proceed in plasma catalysis at low temperatures, with high conversion. This is not possible in thermal catalysis due to the relatively large activation barriers for C-N bond formation, which is one of the critical steps in HCN synthesis.

For the dehydrogenation step of the hydrogenated intermediates, i.e., HCNH and $HCNH_2$, Table 5.1 suggests that the activation barriers for the reactions taking place on the rougher surface of Cu (220) are slightly higher than for the same reactions occurring on the flatter Cu (111) and Cu (200) surfaces. This suggests that the dehydrogenation steps are more likely to happen on Cu (111) and Cu (200) surfaces. However, a more detailed study considering the highly complex network of possible reaction pathways and coverage effects is needed to determine the surface sensitivity of the plasma-assisted HCN synthesis from ammonia and methane.

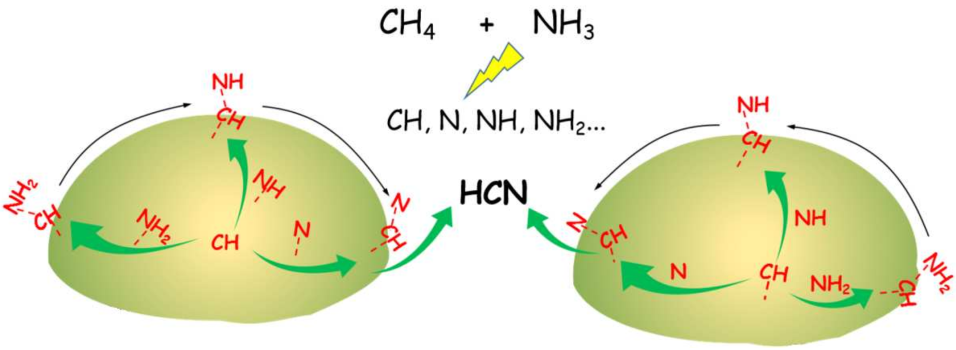

Figure 5.4: Schematic diagram of the reaction mechanism in plasma-catalytic ARM for HCN synthesis. left: the reaction between pre-adsorbed CH and gas-phase NHx, and right: reaction between gas phase CH and pre-adsorbed NHx.

5.4 Conclusion

We performed DFT calculations for plasma-catalytic ammonia reforming of methane (ARM) for the production of HCN and H_2 on Cu surfaces. By considering combined experimental and DFT calculation results, we can conclude that HCN production in plasma catalysis can be attributed to the barrierless ER reactions between radicals generated in plasma and adsorbed species over the Cu surface, as schematically shown in Figure 5.4.

Chapter 6

Reactivity of Plasma-Induced Vibrationally Excited Species

6.1 Introduction

As mentioned earlier, non-thermal plasmas provide a non-equilibrium environment in which collisions between the plasma species can lead to the formation of excited molecules, radicals, and ions. Depending on the relevant energy thresholds, electronic, rotational, or vibrational excitations can take place. Vibrational excitations can occur due to collisions in the energy range of 0.1 to 1.5 eV/molecule [155]. While interacting with the surface of a catalyst, the reactivity of a vibrationally excited molecule can be different from its reactivity in the ground state. This change in reactivity is due to the additional energy stored in the vibrational degrees of motion on the one hand and the induced change in the transition state, on the other hand [43].

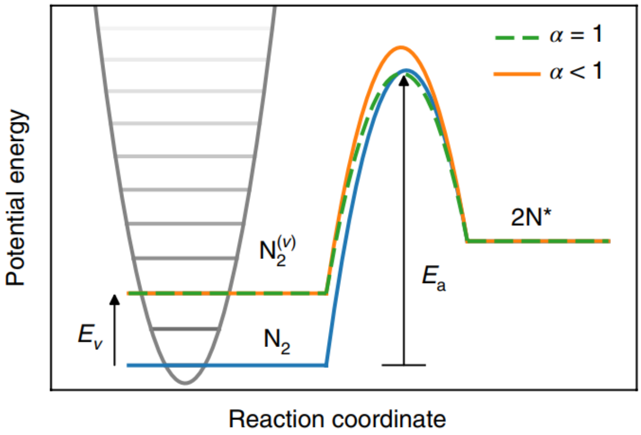

Figure 6.1: Effect of vibrational excitation on the activation energy of N_2 dissociation, corresponding to the vibrational efficiency (α)- Adapted from [150].

The effect of vibrational excitation on the reactivity can be described by the so-called vibrational efficiency factor (α) defined by the Fridman-Macheret (F-M) model [28]. However, the F-M model provides a coarse-grained approach that is not capable of demonstrating a precise description of vibrationally induced changes in the reaction pathway. Figure 6.1 shows how the possible effect of vibrational excitation can facilitate the occurrence of the N_2 dissociation reaction by increasing the energy of the reactant. As indicated, the reaction coordinate of the vibrationally excited molecule only matches the reaction coordinate of the ground state molecule when $\alpha=1$. When the vibrational efficiency is lower, the change in activation energy is not correspondingly the same as the vibrational energy (E_v) of the molecule [150]. Figure 6.2 also shows the rate enhancements linked to the plasma-induced vibrational excitation of the N_2 molecule interacting on various metal surfaces [150].

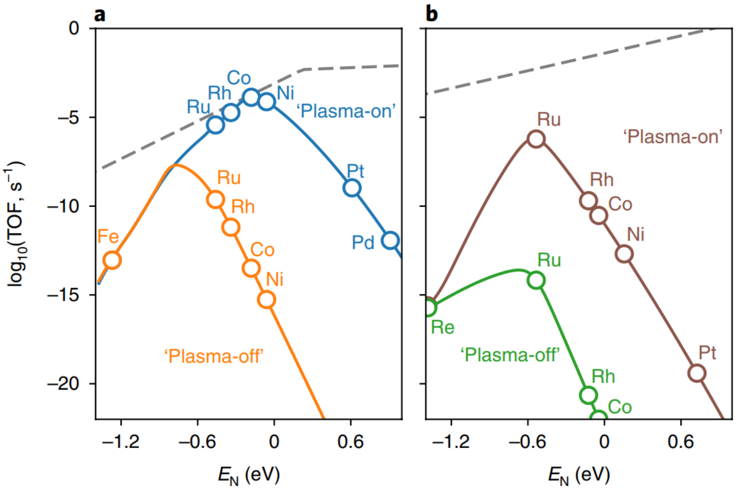

Figure 6.2: Plasma-induced rate enhancements for N_2 dissociation via vibrational excitation for a) step and b) terrace sites- Adapted from [150].

It is well-known that vibrational excitation plays an important role in so-called warm plasmas, like gliding arc discharges and microwave plasmas, changing the whole network of plasma-catalytic reactions. Since gliding arc discharges and microwave plasmas allow selective excitation of energy levels, they show great promise towards achieving high vibrational efficiencies [156]. However, it must be realized that these plasma types are less straightforward to be combined with catalysts. In addition, DBD plasmas, which are most common in plasma catalysis, can also exhibit some degree of vibrational excitation, as demonstrated by recent simulations [157]. These advantages provide enough incentives to investigate the effect of plasma-induced vibrational excitation on catalytic surface reactions in more detail via atomistic simulations. Atomistic modeling of vibrational excitation has its own challenges, such as the difficulty of allocating a quantum mechanical energy spectrum to the molecules and sampling the rare events that cannot be achieved using the standard computational timescales of ab-initio molecular dynamics (AIMD) simulations. It is also very challenging to consider correlated vibrational states during the interactions. In this chapter, we tackle some of these problems for the simple case of diatomic molecules, to provide a framework to be extended later for the reactions containing polyatomic molecules.

6.2 Computational Details

Similar to the previous chapters, spin-polarized DFT calculations were carried out using the Quickstep [102] module of the CP2K [103] package. The dispersion-corrected PBE [73] functional was applied, employing the DZVP basis sets [104] and the GTH pseudopotentials for the AIMD calculations. For the geometry optimization prior to the MD simulations, we used the BFGS scheme with a maximum force tolerance of 0.02 $eV/\text{Å}$.

Both microcanonical and canonical ensembles were considered for carrying out the calculations. As detailed below, we used both Nosé-Hoover [158–161] and Hotspot-GLE [162] thermostats, depending on the approach employed for the treatment of the vibrationally excited diatomic molecules.

When the dissociation of the molecule or in general, the occurrence of a reaction is rare and a very long simulation timescale is required, resorting to advanced sampling techniques such as metadynamics [163, 164] seems quite useful, especially to avoid the high cost of unbiased AIMD simulations. Metadynamics is an efficient method that is based on gradually adding a bias potential in the form of Gaussian functions to the system so that the PES minima can be filled up. To perform an efficient metadynamics calculation, we first have to define a proper collective variable (CV) that describes the dynamics of the system along the reaction coordinate. This is important, especially to identify intermediate states to explore the rare events. By monitoring the fluctuations of the selected CV, we can specify the properties of the Gaussians that we are going to employ during the metadynamics simulations. Defining a good CV can also help to understand where an additional bias is needed and where the system can escape the local minima by normal evolution and without the help of bias potential.

In the simulations presented here, the collective variable used corresponds to the coordination number, describing the interaction between oxygen and carbon atoms. It is defined as:

$$CN_{\mathrm{OC}} = \frac{1}{N_{\mathrm{O}}} \sum_{i_{\mathrm{O}}} \sum_{j_{\mathrm{C}}} \frac{1 - (\frac{r_{ij}}{R_0})^{nn}}{1 - (\frac{r_{ij}}{R_0})^{nd}} \tag{6.1}$$

in which nn and nd determine the curvature of the function used to compute the coordination number and R_0 is the reference distance between two atoms.

6.3 Results and Discussion

We tried to analyze the effect of vibrational excitation on both hydrogen exchange and CO hydrogenation reactions:

$$\mathrm{H} + \mathrm{H}_2^* \rightarrow \mathrm{H}_2 + \mathrm{H} \tag{6.2}$$

$$\mathrm{H}_2 + \mathrm{CO}^* \longrightarrow \mathrm{CH}_2 + \mathrm{O} \tag{6.3}$$

6.3.1 Addition of initial potential energy

The first step towards modeling the vibrational excitation of a diatomic molecule is to conduct a vibrational analysis to obtain the molecule's vibrational modes. Then, in order to excite the molecule from its ground state to a higher vibrational state, a specific amount of energy, dictated by the laws of quantum mechanics, needs to be transferred to the molecule. In the microcanonical ensemble in which the energy of the system is preserved, the initial vibrational energy can be allocated to a diatomic molecule via the bond length extension in terms of the potential energy. To add the correct quanta of energy to the molecule for the excitation of a desired vibrational mode, we should first calculate the potential energy surface (PES) via single-point energy calculations. The calculated PES of the H_2 and CO molecules are shown in Figure 6.3 and Figure 6.4, respectively. By fitting the PES of the molecule to the harmonic potential, we can get the energy levels corresponding to the quantum mechanical description of a harmonic oscillator. However, anharmonic effects are quite important and cannot be neglected if an accurate description is required. We therefore used the Morse potential, which is a more suitable model to describe the vibrational motion of a diatomic molecule [165].

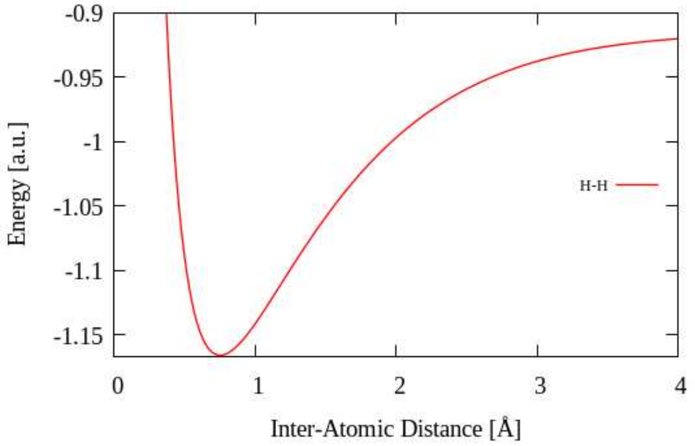

Figure 6.3: Potential energy surface of a gas phase H_2 molecule.

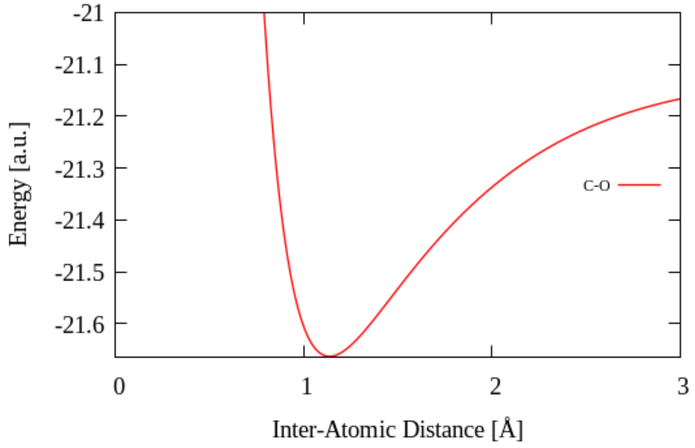

Figure 6.4: Potential energy surface of a gas phase CO molecule.

The Morse potential is defined as:

$$V(R) = D(1 - e^{(-a(R-R_0))})^2 \tag{6.4}$$

where R is the interatomic distance, R_0 is the equilibrium bond length, D is the depth of the potential well corresponding to the dissociation energy, and a is a parameter determining the width of the potential, which can be written as:

$$a = 2\pi\nu_0\sqrt{\frac{2\mu}{D}} \tag{6.5}$$

employing ν_0 and μ as the vibrational frequency and reduced mass of the molecule, respectively.

By fitting the Morse potential to the PES data, we can obtain the vibrational states and corresponding energies using:

$$E_n = h\nu_0(n + \frac{1}{2}) - \frac{\left[h\nu_0(n + \frac{1}{2})\right]^2}{4D} \tag{6.6}$$

in order to obtain the precise amount of bond length elongation for the excitation of the molecule to the vibrational mode of interest. After increasing the interatomic bond length, we can conduct the AIMD simulations to see the excited molecule's behavior in this vibrational mode.

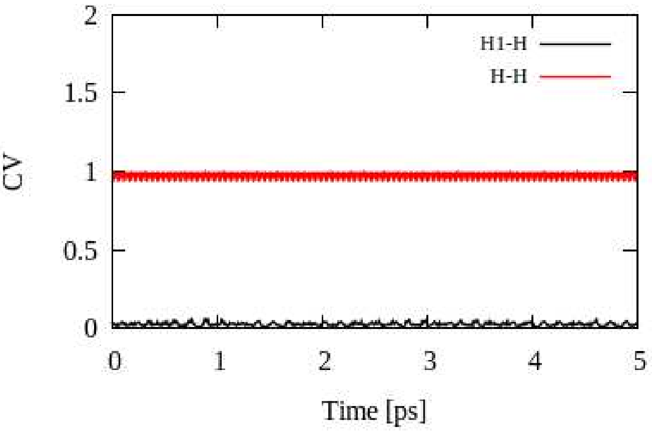

Figure 6.5: Evolution of collective variables for H_2 excitation via bond length stretching (n=2) in $H + H_2^* \rightarrow H_2 + H$ reaction.

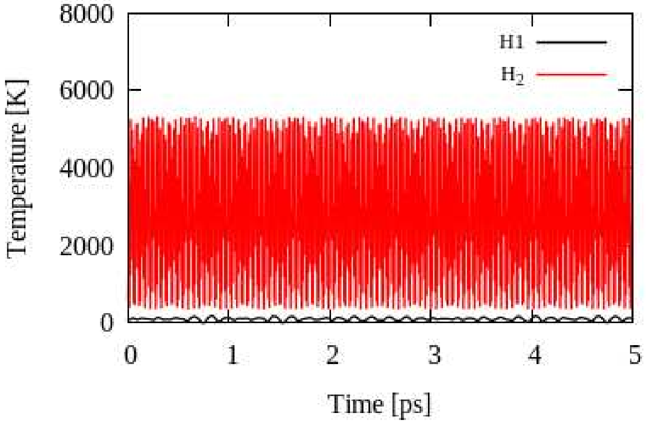

Figure 6.6: Temperature versus simulation time for H_2 excitation via bond length stretching (n=2) in $H + H_2^* \rightarrow H_2 + H$ reaction.

For the $H + H_2^* \rightarrow H_2 + H$ reaction, by extending the H-H bond length to 1.145 Å corresponding to the $n = 2$ energy level, we can see that coordination numbers do not change during the simulation timescale (Figure 6.5) while the temperature of the H_2 molecule (Figure 6.6) indeed shows that the molecule is vibrationally excited, and the lone H atom has much lower temperature. Figure 6.6 also shows that the vibrational excitation of the H_2 molecule is maintained during the simulation. However, since the hydrogen exchange reaction did not occur (at least not within the simulated time scale), this implies that the added vibrational energy is not adequate to overcome the barrier, or a much longer simulation time scale is needed to capture the occurrence of the reaction.

The same behavior is observed in Figure 6.7 and Figure 6.8 for the extension of the CO bond length corresponding to the $n = 5$ energy level in the $H_2 + CO^* \longrightarrow CH_2 + O$ reaction. Although the vibrational excitation is correctly applied to the molecule, and the excitation is maintained during the simulation time frame, the reaction did not happen. This is expected because of the high dissociation energies of H_2 and CO molecules.

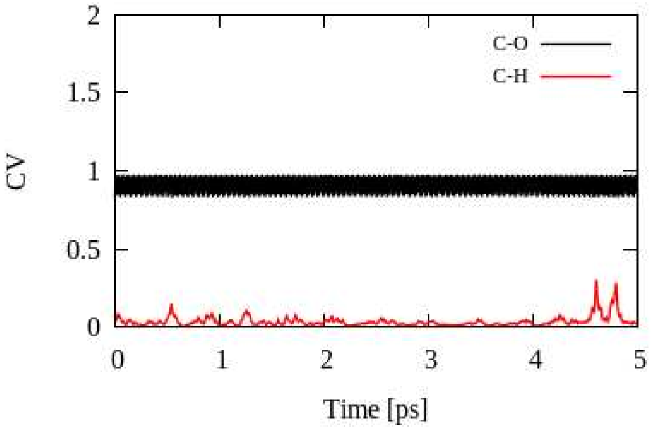

Figure 6.7: Evolution of collective variables for CO excitation via bond length stretching (n=5) in $H_2 + CO^* \longrightarrow CH_2 + O$ reaction.

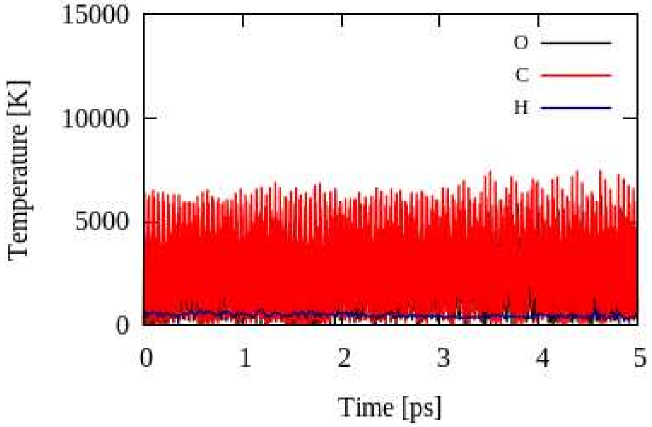

Figure 6.8: Temperature versus simulation time for CO excitation via bond length stretching (n=5) in $H_2 + CO^* \longrightarrow CH_2 + O$ reaction.

6.3.2 Hotspot non-equilibrium GLE thermostat

An alternative way for adding vibrational energy to a molecule is to use a non-equilibrium simulation approach [162] based on the generalized Langevin equation (GLE) to excite a selected set of vibrational modes while the other modes remain at the background temperature. In this method, we use a hotspot thermostat (also known as a colored noise thermostat) to increase the energy corresponding to the temperature T_{max} for the targeted modes with frequencies $\omega \pm \Delta\omega$, while keeping the other modes at the equilibrium temperature T_{base}. More details on the methodology are reported by Dettori et al. [162].

Using this approach and setting the parameters to $\omega = 2140\ cm^{-1}$, $\Delta\omega = 25\ cm^{-1}$, $T_{max} = 3500$ K, and $T_{base} = 300$ K for the vibrational excitation of CO, we were able to specifically excite the vibrational modes assigned to the C-O bond.

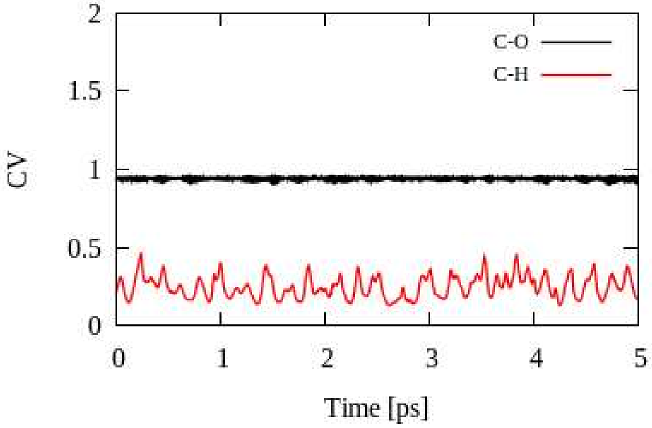

Figure 6.9: Evolution of collective variables for CO excitation via hotspot GLE thermostat in the $H_2 + CO^* \longrightarrow CH_2 + O$ reaction.

As shown in Figure 6.9 and Figure 6.10, carbon and oxygen atoms vibrate around the C-O bond (with lower amplitude compared to the $n = 5$ energy level displayed in Figure 6.7) while maintaining the higher temperature imposed by the colored noise thermostat. The H_2 molecule remains perfectly at the equilibrium temperature of $T_{base} = 300\,K$.

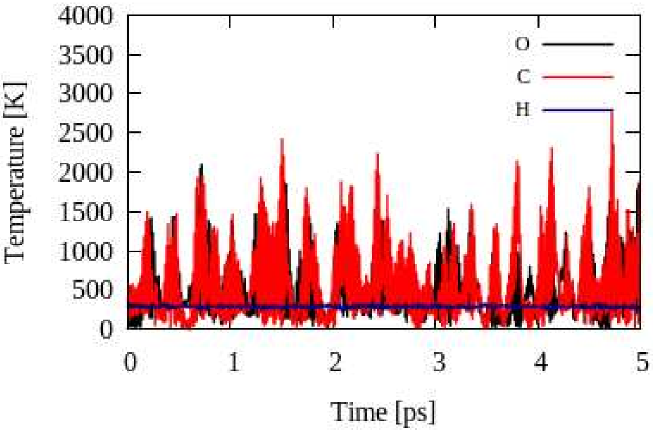

Figure 6.10: Temperature versus simulation time for CO excitation hotspot GLE thermostat in $H_2 + CO^* \longrightarrow CH_2 + O$ reaction.

6.3.3 Metadynamics

Neither of both methods resulted in the dissociation of the targeted molecule, although the vibrational excitation is preserved during the simulation.

Using the same collective variables introduced in section 6.2 and setting the height of the Gaussian hills to WW= 0.1 eV, when they are spawned every 100 MD steps, we conducted metadynamics calculations for the hydrogen exchange reaction.

We can see from Figure 6.11 that dissociation of the H_2 molecule takes place immediately after the start of the calculation, entirely different from the unbiased simulations in which the reaction did not happen. However, as shown in Figure 6.12, because of the absence of a thermostat, the temperature of the system increases dramatically as the simulation continues.

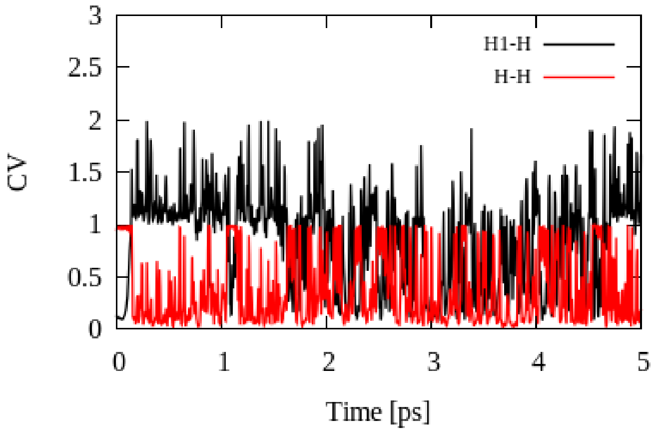

Figure 6.11: Evolution of collective variables for H_2 excitation initiated with bond length stretching (n=2) and using metadynamics in $H + H_2^* \rightarrow H_2 + H$ reaction. H1 represents the lone H atom.

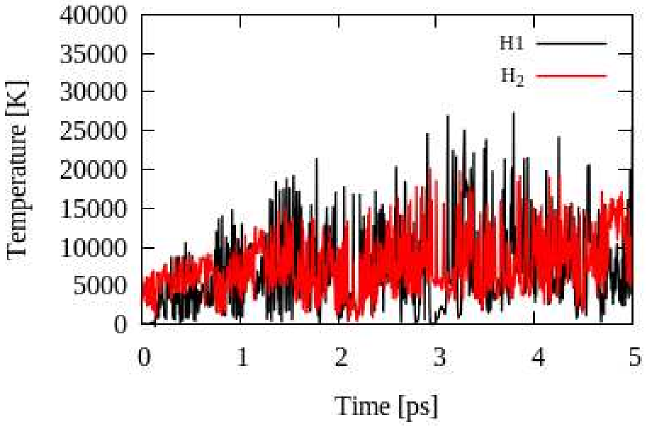

Figure 6.12: Temperature versus simulation time for H_2 excitation initiated with bond length stretching (n=2) and using metadynamics in $H + H_2^* \rightarrow H_2 + H$ reaction.

On the other hand, using the hotspot GLE thermostat for metadynamics calculations, we can see that the temperature remains under control (Figure 6.14), while the hydrogen exchange reaction happens several times during the 5 ps of AIMD simulations (Figure 6.13).

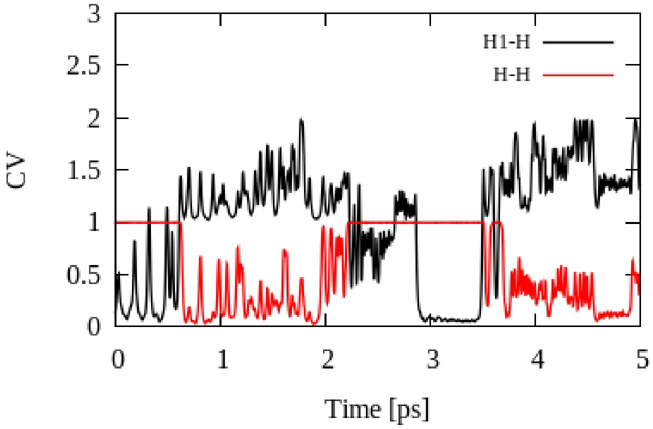

Figure 6.13: Evolution of collective variables for H_2 excitation initiated with hotspot GLE thermostat and using metadynamics in $H + H_2^* \rightarrow H_2 + H$ reaction.

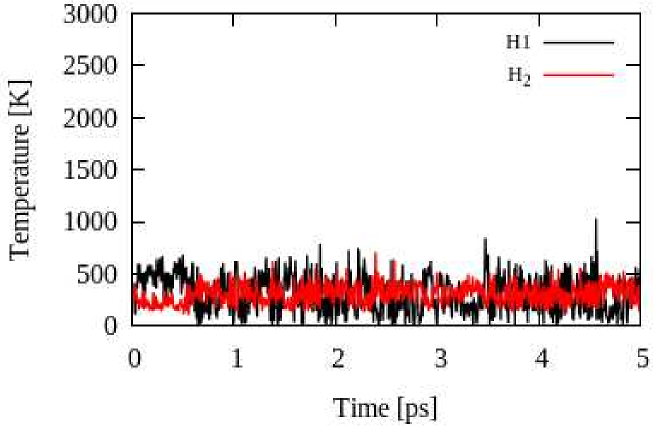

Figure 6.14: Temperature versus simulation time for H_2 excitation initiated with hotspot GLE thermostat and using metadynamics in $H + H_2^* \rightarrow H_2 + H$ reaction.

6.4 Conclusion

In this chapter, we tried to briefly discuss the reactivity of plasma-induced vibrationally excited species. The focus was on diatomic molecules taking part in simple reactions, such as hydrogen exchange and carbene formation. First, vibrational analysis and single-point energy calculations were conducted to obtain the PES for H_2 and CO molecules. Then via both the stretching method and non-equilibrium colored-noise thermostat, the desired vibrational energy is added to the molecules. During the AIMD simulations, the vibrational excitation of the molecules was maintained. For reactions with a large barrier, such as CO and H_2 dissociation, advanced methods such as metadynamics might be needed for sampling the rare events. Employing the hotspot GLE thermostat along with the metadynamics allows observing the hydrogen exchange reaction. Calculations in this chapter will be continued and extended to consider the reactivity of vibrationally excited polyatomic species, such as CO_2 and CH_4, that are of interest for plasma catalysis (e.g., DRM).

Summary and Conclusions

In this dissertation, some of the fundamental mechanisms of plasma-catalyst interactions are studied by means of atomistic calculations based on density functional theory (DFT).

After a general introduction on the context of this thesis in Chapter 1, and explaining the theory behind our calculations in Chapter 2, we study in Chapter 3 the effect of excess electrons induced by plasma on the adsorption properties of CO_2 on titania-supported Cu_5 and Ni_5 clusters, using spin-polarized and dispersion corrected DFT calculations. The effect of excess electrons on the adsorption of Ni and Cu pentamers as well as on CO_2 adsorption/dissociation on a pristine anatase TiO_2 (101) slab is also investigated. The results show that upon adsorption of the Cu_5 and Ni_5 nanoclusters on the anatase surface, the stability of clusters and the direction of charge transfer between the clusters and the support depends on the localization pattern of the excess electron. A linear-to-bent transformation is seen for the CO_2 molecule on the TiO_2 (101) surface as a result of negatively charging the surface, which is attributed with the shifting of high-lying CO_2 antibonding π^* orbitals towards the valence band. For the case of CO_2 activation on supported clusters, an increase in adsorption energies is observed, along with C-O bond elongations for the case of charged surfaces, indicating CO_2 activation. This improved stability is associated with the extra bond formation between the CO_2 molecule and the cluster and support atoms, facilitating the further activation of the molecule. For CO_2 dissociation on the bare TiO_2 (101) surface, we have seen that the reaction is unfavorable for both neutral and negatively charged surfaces. However, for CO_2 dissociation over supported clusters, the presence of excess electrons makes the dissociation reaction favorable, which highlights the importance of the nanoclusters. We hypothesize that surface charging is a plausible cause for the synergistic effects sometimes observed in plasma catalysis employing TiO_2 (101) surfaces.

In chapter 4, we first studied the effect of applying an external electric field via two different methods on CO_2 activation on Cu (111), Cu (211), Cu (110) and Cu (001) surfaces. We then combined surface charging and surface morphology with the electric field effect to see how this combination changes the chemisorption properties and activation of the CO_2 molecule. We observe that the binding energy of the CO_2 molecule on Cu surfaces rises significantly upon increasing the applied electric field strength. In addition, rougher surfaces respond more effectively to the presence of the external electric field towards facilitating the formation of a carbonate-like CO_2 structure and the transformation of the most stable adsorption mode from physisorption to chemisorption. The presence of surface charges further strengthens the electric field effect and gives rise to more pronounced bending of the CO_2 molecule and C-O bond elongation. On the other hand, a net charge in the absence of an externally applied electric field only shows a marginal effect on CO_2 binding on Cu surfaces. The chemisorbed CO_2 is more stable and further activated when the effects of an external electric field, rough surface and surface charge are combined. These results partially elucidate the underlying factors that control CO_2 activation in both heterogeneous thermal catalysis and plasma catalysis, as well as in electrochemical processes.

Chapter 5 deals with the study of the interaction of plasma-generated radicals with each other and the catalyst surface. We performed DFT calculations to support experimental work on ammonia reforming of methane (ARM) to produce HCN and H_2 at low temperatures by combining CH_4/NH_3 plasma and supported Cu/Silicate-1 catalyst. Reaction pathways via both Langmuir–Hinshelwood (LH) and Eley-Rideal (ER) mechanisms with N, NH, NH_2, and CH radicals produced in the plasma, for the production of HCN were identified by calculation of the Minimum Energy Path (MEP) using Nudged Elastic Band (NEB) calculations. The results show that the high energy of the gas phase radicals leads to the dominance of barrierless reactions happening via the ER mechanism for the direct C-N coupling. The highly reactive plasma-generated N, NH, NH_2, and CH radicals can either react directly with the pre-adsorbed species or chemisorb on the Cu surface, to be involved in reactions happening via the LH mechanism. The barrierless C-N coupling via the ER mechanism can explain why HCN formation in plasma catalysis may proceed at reduced temperatures compared to thermal catalysis, in which the LH mechanism is typically dominant, and relatively large activation barriers need to be overcome.

Finally, chapter 6 contains a short discussion on the simulation of plasma-induced vibrational excitation of diatomic molecules. Two methods are considered for adding the vibrational energy to the molecules of interest. Also, metadynamics simulations are conducted to study the sampling of rare events.

In conclusion, we demonstrated that the plasma-induced changes in the electronic structure of catalysts and reactants have great potential in steering the plasma-catalytic reactions. From the atomistic point of view, a valuable and fundamental description of plasma-surface interactions can be obtained, by employing molecular dynamics simulations (using DFT or semi-empirical methods) focusing on the co-adsorption of reactants such as CH_4 and CO_2 (e.g., for dry reforming of methane) under plasma-catalytic conditions, and vibrational excitation of polyatomic molecules and radicals interacting with pre-adsorbed species via ER mechanisms. This could be of great interest for future work. Further, atomistic calculations combined with larger scale modeling methods (also to consider fluxes and densities of plasma species) can significantly improve our understanding of the synergistic effects seen in plasma catalysis.

Samenvatting en Conclusies

In dit proefschrift worden fundamentele mechanismen van plasma-katalysator interacties bestudeerd door middel van atomistische berekeningen gebaseerd op dichtheidsfunctionaliteitstheorie (DFT).

Na een algemene introductie over de context van dit proefschrift in hoofdstuk 1, en een uitleg van de theorie achter onze berekeningen in hoofdstuk 2, bestuderen we in hoofdstuk 3 het effect van overtollige elektronen geïnduceerd door een plasma op de adsorptie-eigenschappen van CO_2 op titania-ondersteunde Cu_5 en Ni_5 clusters, met behulp van spin-gepolariseerde en dispersie-gecorrigeerde DFT berekeningen. Het effect van overtollige elektronen op de adsorptie van Ni en Cu pentameren en op de CO_2 adsorptie/dissociatie op een zuiver anataas TiO_2 (101) kristal wordt ook onderzocht. De resultaten tonen aan dat bij adsorptie van de Cu_5 en Ni_5 nanoclusters op het anataasoppervlak de stabiliteit van de clusters en de richting van de ladingsoverdracht tussen de clusters en het dragermateriaal afhankelijk is van de lokalisatie van het extra elektron. CO_2 ondergaat een transformatie van de lineaire tot de gebogen vorm op het TiO_2 (101) oppervlak als gevolg van het negatief opladen van het oppervlak, hetgeen wordt toegeschreven aan het verschuiven van het hooggelegen CO_2 antibindende * orbitaal in de richting van de valentieband. Bij CO_2 activatie op de clusters op een dragermateriaal merken we een verhoging van de adsorptie-energieën, samen met het uitrekken van de C-O bindingslengte voor de geladen oppervlakken, wat aangeeft dat CO_2 geactiveerd wordt. Deze verhoogde stabiliteit hangt samen met de extra bindingsvorming voor het CO_2 molecuul met het cluster en de substraatatomen, die de verdere activering van het molecuul vergemakkelijkt. Voor de CO_2 dissociatie op zuivere TiO_2 (101) oppervlakken zien we dat de reactie ongunstig is voor zowel neutrale als negatief geladen oppervlakken. Voor CO_2 dissociatie op de clusters op een dragermateriaal maakt de aanwezigheid van overtollige elektronen de dissociatiereactie echter gunstig, wat het belangrijke effect van nanoclusters onderstreept. We stellen dat oppervlaktelading een plausibele oorzaak is voor de synergetische effecten die soms worden waargenomen bij plasmakatalyse op TiO_2 (101) oppervlakken.

In hoofdstuk 4 hebben we eerst het effect van externe elektrische velden bestudeerd via twee afzonderlijke methoden op CO_2 activering op Cu (111), Cu (211), Cu (110) en Cu (001) oppervlakken. Vervolgens hebben we de oppervlaktelading en de oppervlaktemorfologie gecombineerd met het effect van het elektrisch veld om te bestuderen hoe deze combinatie de chemisorptie eigenschappen en de activering van het CO_2 molecuul verandert. Uit de resultaten blijkt dat de bindingsenergie van het CO_2-molecuul op Cu oppervlakken aanzienlijk toeneemt bij het verhogen van de aangelegde elektrische veldsterkte. Bovendien reageren ruwere oppervlakken effectiever op de aanwezigheid van het externe elektrische veld om de vorming van een carbonaatachtige CO_2 structuur en de transformatie van de meest stabiele adsorptiemodus van fysisorptie naar chemisorptie te vergemakkelijken. De aanwezigheid van oppervlakteladingen versterkt het effect van het elektrisch veld nog verder en leidt daardoor tot een betere buiging van het CO_2molecuul en de verlenging van de C-O binding. Anderzijds vertoont een nettolading bij afwezigheid van een extern aangelegd elektrisch veld slechts een marginaal effect op de CO_2 binding over Cu oppervlakken. Het gechemisorbeerde CO_2 is stabieler en wordt verder geactiveerd wanneer de effecten van een extern elektrisch veld, ruw oppervlak en oppervlaktelading worden gecombineerd. Deze resultaten verhelderen (deels) de onderliggende factoren die de activering van CO_2 op heterogene thermische en plasma-katalysatoren en in elektrochemische processen regelen.

Hoofdstuk 5 behandelt de studie van de interactie van plasma-gegenereerde radicalen met elkaar en met het katalysatoroppervlak. Concreet voeren we DFT simulaties uit ter ondersteuning van experimenteel werk over ammoniak-reforming van methaan (ARM) om HCN en H_2 te produceren bij lage temperaturen door de combinatie van CH_4/NH_3 plasma en een Cu/Silicaat-1 katalysator. Zowel Langmuir-Hinshelwood (LH) en Eley-Rideal (ER) reactieroutes voor de productie van HCN uit plasma-genenereerde N, NH, NH_2 en CH radicalen werden geïdentificeeerd door de berekening van het zgn. 'Minimum Energy Path' (MEP) met behulp van 'Nudged Elastic Band' (NEB) berekeningen. De resultaten tonen aan dat de hoge energie van de gasfase radicalen leidt tot de dominantie van barrièrevrije reacties via het ER mechanisme voor de directe C-N koppeling. De zeer reactieve plasma-gegenereerde N, NH, NH_2 en CH radicalen kunnen ofwel direct reageren met eerder geadsorbeerde deeltjes, ofwel door chemisorptie op het Cu oppervlak, om dan via het LH mechanisme betrokken te zijn bij de reacties die plaatsvinden. De barrièrevrije C-N koppeling via het ER mechanisme kan verklaren waarom de HCN vorming in plasmakatalyse bij lagere temperaturen verloopt in vergelijking met thermische katalyse waarbij het optreden van reacties meestal via het LH mechanisme verloopt en waarin relatief hoge activeringsbarrières moeten worden overwonnen.

Tenslottte bevat hoofdstuk 6 een korte bespreking over plasma-geïnduceerde vibratie-excitatie van diatomische moleculen. Twee verschillende methoden zijn beschouwd om vibratie-energie toe te voegen aan de beoogde moleculen. Ook worden metadynamische simulaties uitgevoerd om de steekproef van zeldzame gebeurtenissen te bestuderen.

We kunnen besluiten dat deze studie heeft duidelijk gemaakt dat de plasma-geïnduceerde veranderingen in de elektronische structuur van katalysatoren en reagentia een groot potentieel hebben om de plasma-katalytische reacties te sturen. Vanuit atomair oogpunt kan een waardevolle en fundamentele beschrijving van plasma-oppervlak-interacties worden bereikt. door middel van moleculaire dynamica (met behulp van DFT of semi-empirische methoden), gericht op de co-adsorptie van reactanten zoals CH_4 en CO_2 (bv. voor dry reforming van methaan) onder plasmakatalytische condities en vibratie-excitatie van polyatomaire moleculen en radicalen die interageren met geadsorbeerde deeltjes via het ER-mechanisme. Dit is bijzonder interessant voor toekomstig onderzoek. Verder kunnen atomistische berekeningen gecombineerd met modelleermethoden op grotere schaal (ook om rekening te houden met fluxen en dichtheden van plasmadeeltjes) onze inzichten in de synergetische effecten die worden waargenomen bij plasmakatalyse aanzienlijk verbeteren.

List of Publications

- **A. Jafarzadeh**, K. M. Bal, A. Bogaerts, and E. C. Neyts, “CO_2 Activation on TiO_2-Supported Cu_5 and Ni_5 Nanoclusters: Effect of Plasma-Induced Surface Charging,” *J. Phys. Chem. C*, vol. 123, no. 11, pp. 6516–6525, Feb. 2019
- **A. Jafarzadeh**, K. M. Bal, A. Bogaerts, and E. C. Neyts, “Activation of CO_2 on Copper Surfaces: The Synergy between Electric Field, Surface Morphology, and Excess Electrons,” *J. Phys. Chem. C*, vol. 124, no. 12, pp. 6747–6755, Mar. 2020
- Yi, Y.; Wang, X.; **Jafarzadeh, A**.; Wang, L.; Yan, J.; Zhang, R.; Zhang, H.; Guo, H.; Neyts, E. C. and Bogaerts, A.” Plasma-catalytic Ammonia Reforming of Methane over Cu-based Catalysts for the Production of HCN and H_2 at Reduced Temperature ”- Manuscript under revision at *ACS Catalysis* - Yi, Y; Wang, X, and **Jafarzadeh, A** contributed equally to this work as co-first author.
- Y. Yi, Sh. Li, Zh. Cui, **A. Jafarzadeh**, Y. Zhang, R. Ahmed, L. Wang, Y. Hao, M. Liu, H. Zhang, W. Wang, P. Liu, X. Tu, H. Guo, and A. Bogaerts “Selective Oxidation of CH_4 to CH_3OH through Plasma Catalysis” – Manuscript under revision at *ACS Catalysis.*

List of Presentations

- **A. Jafarzadeh**, K. M. Bal, A. Bogaerts, and E. C. Neyts, “CO_2 Activation on Copper Surfaces: The Combined Effect of Electric Field, Surface Morphology and Excess Electrons” International school on electronic structure calculations- **(Poster Presentation)**, Feb 2020, University of Paderborn and Paderborn Center for Parallel Computing (Germany)
- **A. Jafarzadeh**, “Atomistic Simulations of Plasma-Surface Interactions”, **(Invited Speaker),** Nov 2019, Jürg Hütter group, Department of Chemistry, University of Zürich (Switzerland)
- **A. Jafarzadeh**, E. C. Neyts, and A. Bogaerts, “CO_2 activation on negatively charged Cu_5 and Ni_5 nano-clusters supported on anatase TiO_2 (101)”- **(Poster Presentation)**, Dec 2018, CECAM workshop on metal nanoparticles, Universit´e Grenoble Alpes (France)
- **A. Jafarzadeh**, A. Bogaerts, and E. C. Neyts, “CO_2 activation on TiO_2-supported Cu_5 and Ni_5 nanoclusters: Effect of plasma-induced surface charges”, **(Oral Presentation-** Awarded the Student Travel Grant by the **APS)** Nov 2018, The 71st Annual Gaseous Electronics Conference Co-Located with the 60th Annual meeting of the APS Division of Plasma Physics, The Oregon Convention Center (United States)

Appendix 1

CO_2 Activation on TiO_2-supported Cu_5 and Ni_5 Nanoclusters: Effect of Plasma-Induced Surface Charging – Supporting information to Chapter 3

---

1. Isolated Ni_5 and Cu_5 clusters

Five random initial configurations were examined for both Ni and Cu pentamers in the gas phase to find the most stable configuration. The cohesive energy per atom was used as an indicator for the cluster stability.

$$E_{Cohesive} = \frac{E_{cluster} - 5E_{Ni/Cu}^{gas}}{5}$$

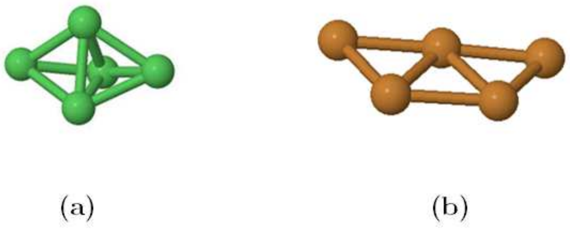
(a) (b)

Figure A1. 1: The most stable configurations for a) Ni_5 and b) Cu_5 clusters

From the geometry optimization calculations, we find that the most stable configuration for Cu_5 is a trapezoidal planar structure with cohesive energy of -1.76 eV. Previous studies have also reported the same configuration as the most stable structure for the Cu pentamer [166–169]. For the Ni_5 cluster, a trigonal bi-pyramidal structure is seen to be the most stable configuration, again in agreement with the literature [170, 171]. Different spin configurations are tested for the calculation of the Ni_5 cluster, and we find that configurations with the spin multiplicity of 3 and 5 are the most stable structures with cohesive energies of $-2.39\ eV$ and $-2.43\ eV$, respectively.

2. Unstable orientations for adsorption of Ni_5 and Cu_5 clusters on TiO_2

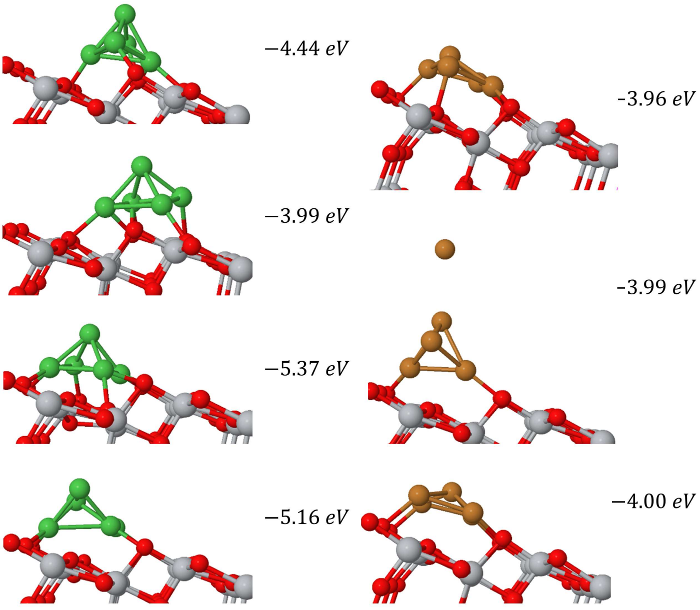

Ni_5/TiO_2 Cu_5/TiO_2

Figure A1. 2: Unstable configurations for the adsorption of Ni_5 and Cu_5 clusters over TiO_2.

3. PDOS plots for adsorption of clusters on TiO_2 (101)

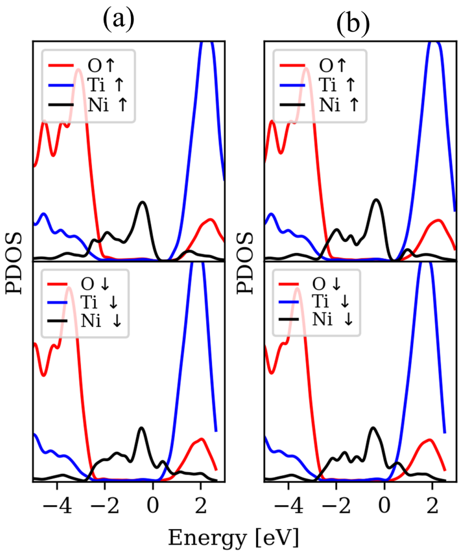

Figure A1. 3: Projected density of states for adsorption of Ni_5 cluster on small slab of TiO_2 (101) for a) neutral and b) charged configurations.

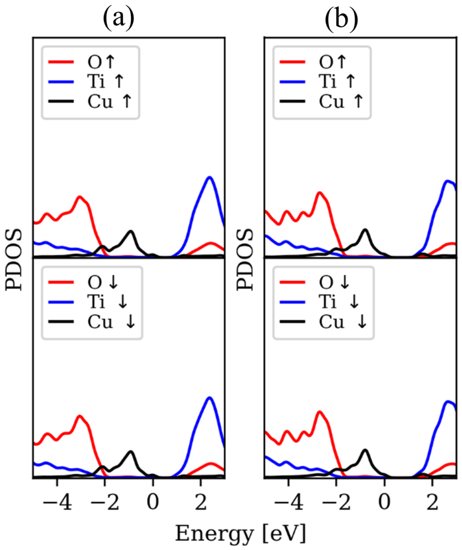

Figure A1. 4: Projected density of states for adsorption of Cu_5 cluster on small slab of TiO_2 (101) for a) neutral and b) charged configurations.

4. Results with fixed three bottom layers of $TiO_2(101)$

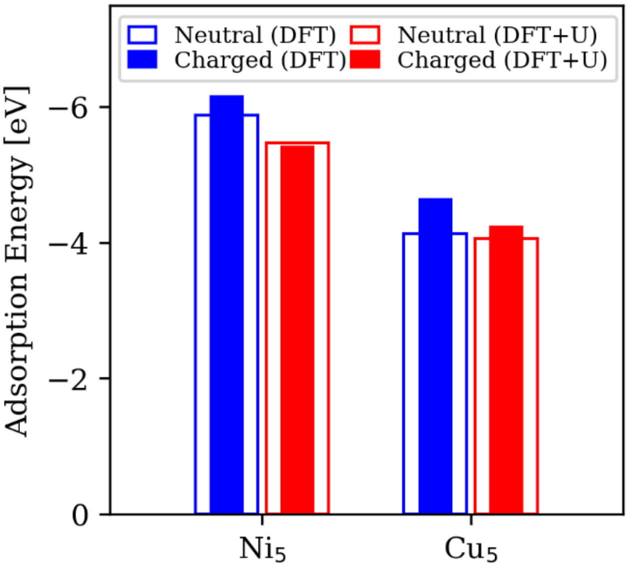

Figure A1. 5: Adsorption energy of Ni_5 and Cu_5 clusters on TiO_2.

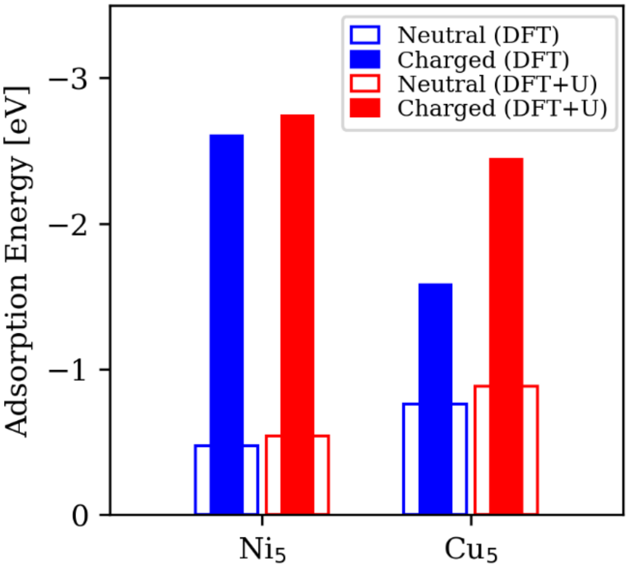

Figure A1. 6: Adsorption energy of the CO_2 molecule on Ni_5/TiO_2 and Cu_5/TiO_2 structures.

5. (2 × 4) supercell of TiO_2 (101)

A large slab of anatase (101) with dimensions of $20.4787 \times 15.138 \times 30.00$ Å^3 (2 × 4 supercell) containing 288 atoms (Figure A1.7) was also used for cross-checking the calculations for CO_2 adsorption on neutral and charged TiO_2(101).

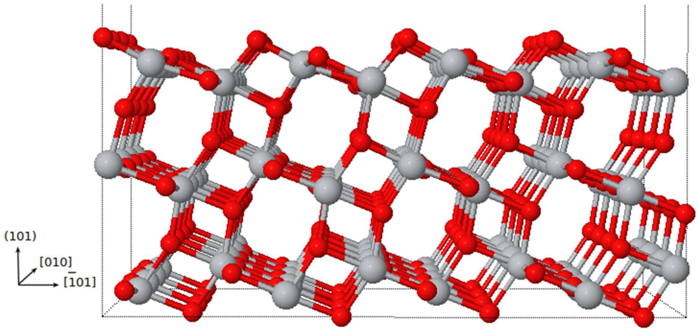

Figure A1. 7: (2 × 4) supercell of anatase TiO_2 (101).

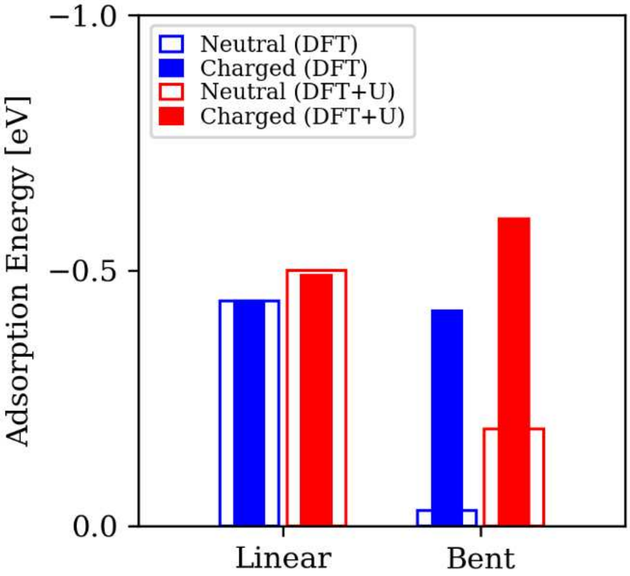

Figure A1. 8: Adsorption energy of the CO_2 molecule on the neutral and charged surface of TiO_2 – 3 layers of the slab were fixed during the geometry optimization.

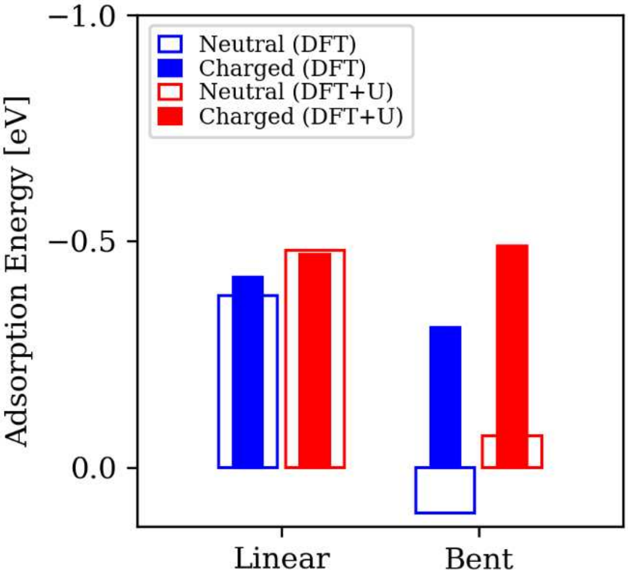

Figure A1. 9: Adsorption energy of the CO_2 molecule on the neutral and charged surface of TiO_2 – all atoms were free to relax during the geometry optimization.

6. Spin moments and net charges

Table A1. 1: Spin moments and net charges of Ni$_5$ and Cu$_5$ clusters in the gas phase.

Ni$_5$- Neutral – gas phase				
Atom	**α**	**β**	**Net Spin moment**	**Net charge**
Ni	8.688	9.395	-0.707	-0.083
Ni	9.329	8.627	0.703	0.044
Ni	9.34	8.616	0.723	0.044
Ni	9.338	8.617	0.721	0.045
Ni	9.304	8.745	0.560	-0.049
Cu$_5$- Neutral- gas phase				
Atom	**α**	**β**	**Net Spin moment**	**Net charge**
Cu	5.625	5.375	0.249	0.001
Cu	5.601	5.383	0.218	0.016
Cu	5.575	5.431	0.144	-0.007
Cu	5.624	5.376	0.248	0.001
Cu	5.573	5.433	0.141	-0.006

Table A1. 2: Spin moments and net charges of Ni$_5$ and Cu$_5$ clusters adsorbed on neutral TiO$_2$.

Ni$_5$- Neutral – (DFT+U)				
Atom	**α**	**β**	**Net Spin moment**	**Net charge**
Ni	9.196	8.729	0.467	0.076
Ni	9.327	8.959	0.369	-0.286
Ni	9.533	8.668	0.865	-0.201
Ni	9.442	8.771	0.671	-0.213
Ni	9.498	8.771	0.728	-0.269
Cu$_5$- Neutral- (DFT+U)				
Atom	**α**	**β**	**Net Spin moment**	**Net charge**
Cu	5.499	5.499	0	0.001
Cu	5.508	5.508	0	-0.016
Cu	5.507	5.507	0	-0.013
Cu	5.478	5.478	0	0.045
Cu	5.527	5.527	0	-0.054

Table A1. 3: Spin moments and net charges of Ni_5 and Cu_5 clusters adsorbed on charged TiO_2.

Ni_5- Charged – (DFT+U)				
Atom	**α**	**β**	**Net Spin moment**	**Net charge**
Ni	9.294	8.981	0.313	-0.275
Ni	9.348	8.987	0.361	-0.335
Ni	9.485	8.863	0.622	-0.348
Ni	9.403	8.904	0.499	-0.307
Ni	9.387	8.992	0.395	-0.378
Cu_5- Charged- (DFT+U)				
Atom	**α**	**β**	**Net Spin moment**	**Net charge**
Cu	5.513	5.512	0.001	-0.025
Cu	5.519	5.517	0.002	-0.036
Cu	5.697	5.698	-0.001	-0.395
Cu	5.519	5.519	0.001	-0.037
Cu	5.56	5.559	0.001	-0.119

Table A1. 4: Spin moments and net charge for CO_2 adsorption on neutral supported clusters. Cluster atoms that have bonds with atoms of the CO_2 molecule are specified with the same colors: C-Ni (green), O-Ni (blue), C-Cu (green), O-Cu (blue). * Cu atom also makes a bond with the oxygen atom of the molecule.

CO_2 on Ni_5/TiO_2 -Neutral (DFT+U)

Atom	α	β	**Net Spin moment**	**Net charge**
Ni	9.269	8.791	0.478	-0.06
🟦 Ni	9.386	8.806	0.58	-0.192
Ni	9.55	8.598	0.952	-0.148
Ni	9.506	8.776	0.729	-0.282
🟩 Ni	9.518	9.212	0.306	-0.73
O	3.429	3.432	-0.003	-0.861
🟦 O	3.266	3.281	-0.015	-0.547
🟩 C	1.111	1.12	-0.009	1.769

CO_2 on Cu_5/TiO_2 - Neutral (DFT+U)

Atom	α	β	**Net Spin moment**	**Net charge**
Cu	5.490	5.490	0	0.020
Cu	5.505	5.505	0	-0.010
Cu	5.461	5.461	0	0.077
🟩 Cu*	5.532	5.532	0	-0.064
🟩 Cu	5.614	5.614	0	-0.228
🟦 O*	3.343	3.343	0	-0.686
O	3.316	3.316	0	-0.632
🟩 C	1.249	1.249	0	1.502

Table A1. 5: Spin moments and net charge for CO_2 adsorption on charged supported clusters. Cluster atoms that have bonds with atoms of the CO_2 molecule are specified with the same colors: C-Ni (green), O-Ni (blue), C-Cu (green), O-Cu (blue). * Ni atom also makes a bond with the oxygen atom of the molecule. ** Cu atom also makes a bond with the oxygen atom of the molecule.

CO_2 on Ni_5/TiO_2 -Charged (DFT+U)

Atom	**α**	**β**	**Net Spin moment**	**Net charge**
Ni*	9.454	8.811	0.643	-0.265
Ni	9.297	8.959	0.338	-0.256
Ni	9.352	9.347	0.005	-0.699
Ni	9.498	8.688	0.811	-0.186
Ni	9.334	8.967	0.367	-0.302
O	3.479	3.51	-0.031	-0.989
O*	3.339	3.307	0.032	-0.647
C	1.141	1.14	0.001	1.719

CO_2 on Cu_5/TiO_2 - Charged (DFT+U)

Atom	**α**	**β**	**Net Spin moment**	**Net charge**
Cu	5.5	5.5	0	0.001
Cu	5.515	5.514	0.001	-0.029
Cu	5.546	5.546	0	-0.091
Cu**	5.531	5.53	0	-0.061
Cu	5.611	5.61	0.001	-0.221
O**	3.402	3.401	0	-0.803
O	3.469	3.469	0	-0.938
C	1.263	1.263	0	1.473

Appendix 2

Activation of CO_2 on Copper Surfaces: The Synergy Between Electric Field, Surface Morphology and Excess Electrons – Supporting Information to Chapter 4

1. Dimensions of the supercells used for the calculations (all in Å):

- For constant potential method

  Cu (111): 12.76 × 13.26 × 30.00
  Cu (211): 12.78 × 12.52 × 30.00
  Cu (110): 10.84 × 15.34 × 30.00
  Cu (001): 10.84 × 14.46 × 30.00

- For dipole sheet method

  Cu (111): 12.76 × 13.26 × 70.00
  Cu (211): 12.78 × 12.52 × 70.00
  Cu (110): 10.84 × 15.34 × 70.00
  Cu (001): 10.84 × 14.46 × 70.00

2. Details for making the dipole sheets

Table A2. 1: Corresponding surface area, charge, and surface charge density on dipole sheets for an electric field of $1V/\text{Å}$.

Surface	**A (Å^2)**	**q |e|**	**σ(C/m^2)**
Cu (111)	169.19	0.936	0.089
Cu (211)	160	0.887	0.089
Cu (110)	166.29	0.92	0.089
Cu (001)	156.75	0.87	0.089

Table A2. 2: Corresponding surface area, charge, and surface charge density on dipole sheets for an electric field of $1.5V/\text{Å}$.

Surface	**A (Å^2)**	**q |e|**	**σ(C/m^2)**
Cu (111)	169.19	1.404	0.133
Cu (211)	160	1.33	0.133
Cu (110)	166.29	1.38	0.133
Cu (001)	156.75	1.30	0.133

3. Cross-checking: Calculation of the adsorption energy of the CO_2 molecule on Cu surfaces using both methods

Cross-checking results for Cu (211) surface are shown in Figure A2.1. Using the constant potential method, and corresponding to the electric field strengths of $1.55\,V/\text{Å}$ and $1.44\,V/\text{Å}$ for Cu (001) and Cu (111), we obtained CO_2 adsorption energies of -0.90 eV and -0.59 eV, respectively. Employing the charged plates method, we obtained adsorption energies of -0.85 eV and -0.62 eV, for an electric field strength of $1.5\,V/\text{Å}$ on Cu (001) and Cu (111), respectively. We note that we had to use different Poisson solvers ("Implicit" [85] for constant potential approach and MT [84] for the dipole sheet method) and the slight difference in adsorption energies is a natural result of using different solvers. As emphasized in

Chapter 4, the trends for adsorption energy as a function of electric field strength are quite similar for both employed methods.

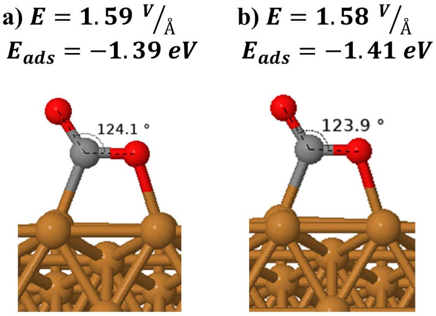

a) $\boldsymbol{E = 1.59\ {}^{V}/_{\text{Å}}}$ $\boldsymbol{E_{ads} = -1.39\ eV}$

b) $\boldsymbol{E = 1.58\ {}^{V}/_{\text{Å}}}$ $\boldsymbol{E_{ads} = -1.41\ eV}$

Figure A2. 1: CO_2 adsorption on Cu (211) surface in the presence of external electric field imposed by a) charged plates and b) constant potential electrodes.

4. Electric field effect- Using the constant potential approach

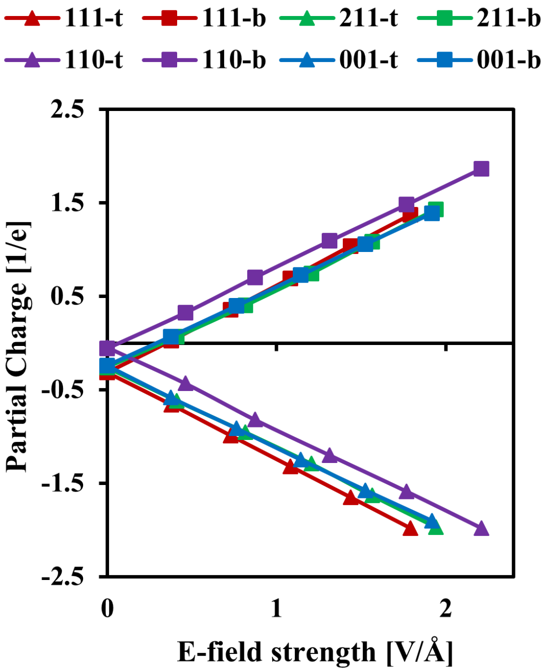

Figure A2. 2: Aggregated surface partial charge versus electric field strength- “t” and “b” represent the top and bottom layers of the Cu surfaces, respectively.

Figure A2.3 shows the potential distribution for the range of applied potential inside the simulation box. As we considered an electrode thickness of 5 Å in our simulations, the potential drops to zero around $z = 2.5$ Å inside the supercell.

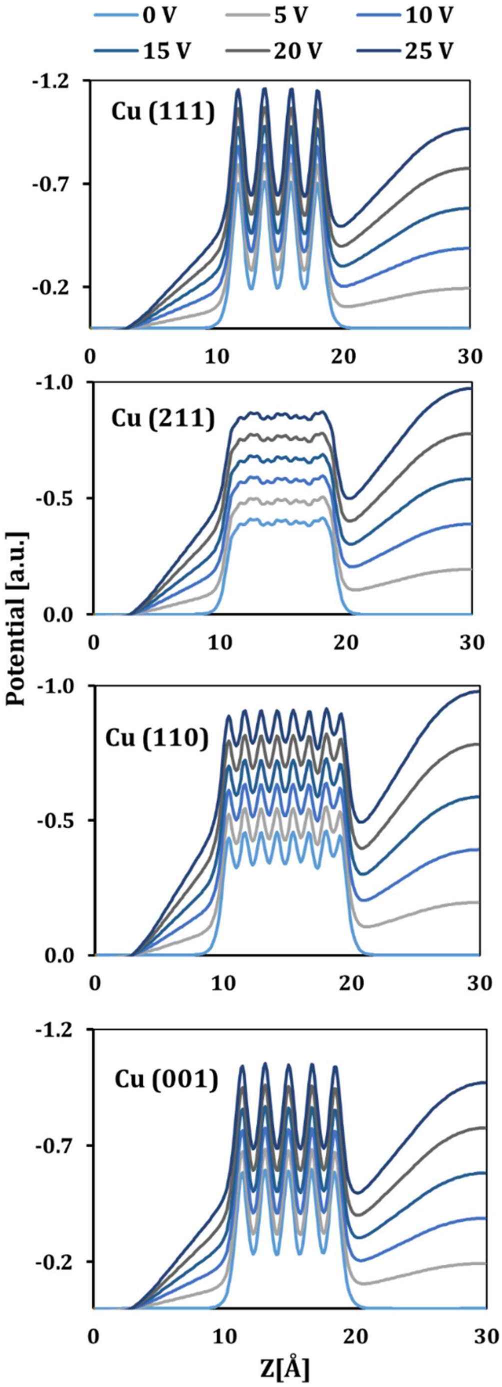

Figure A2. 3: Electrostatic potential around the Cu surfaces for each applied voltage on the electrodes.

Table A2. 3: Bond lengths(Å), angles(°), and adsorption energies(eV) for the most stable CO_2 adsorption mode on Cu (111) as a function of the applied potential.

V [V]	**Ads. mode**	$\mathbf{r_{C\text{-}O}}$		**OCO angle**	$\mathbf{r_{C\text{-}Cu}}$	$\mathbf{r_{O\text{-}Cu}}$	$\mathbf{E_{ads}}$
0	physi.	1.17	1.17	179.9			-0.34
5	physi.	1.17	1.17	178.5			-0.34
10	physi.	1.17	1.17	176.7			-0.35
15	physi.	1.18	1.18	172.1			-0.40
20	chemi.	1.24	1.29	127.2	2.04	2.07	-0.59
25	chemi.	1.25	1.3	125.2	2.05	2.09	-0.90

Table A2. 4: Bond lengths(Å), angles(°), and adsorption energies(eV) for the most stable CO_2 adsorption mode on Cu (211) as a function of the applied potential.

V [V]	**Ads. mode**	$\mathbf{r_{C\text{-}O}}$		**OCO angle**	$\mathbf{r_{C\text{-}Cu}}$	$\mathbf{r_{O\text{-}Cu}}$	$\mathbf{E_{ads}}$
0	physi.	1.17	1.18	179.5			-0.29
5	chemi.	1.23	1.25	137.4	2.05	2.12	-0.33
10	chemi.	1.23	1.28	130.7	2.01	2.03	-0.58
15	chemi.	1.24	1.29	127.0	2.00	2.03	-0.94
20	chemi.	1.25	1.3	123.9	2.01	2.03	-1.41
25	chemi.	1.27	1.31	121.4	2.03	2.04	-1.96

Table A2. 5: Bond lengths(Å), angles(°), and adsorption energies(eV) for the most stable CO_2 adsorption mode on Cu (110) as a function of the applied potential.

V [V]	**Ads. mode**	$\mathbf{r_{C\text{-}O}}$		**OCO angle**	$\mathbf{r_{C\text{-}Cu}}$	$\mathbf{r_{O\text{-}Cu}}$	$\mathbf{E_{ads}}$
0	physi.	1.17	1.18	179.8			-0.39
5	physi.	1.17	1.17	177.6			-0.36
10	chemi.	1.24	1.28	127.9	2.02	2.02	-0.62
15	chemi.	1.25	1.29	125.3	2.03	2.03	-0.96
20	chemi.	1.26	1.3	122.8	2.03	2.03	-1.38
25	chemi.	1.28	1.3	121.0	2.05	2.08	-1.96

Table A2. 6: Bond lengths(Å), angles(°), and adsorption energies(eV) for the most stable CO_2 adsorption mode on Cu (001) as a function of the applied potential.

V [V]	**Ads. mode**	$\mathbf{r_{C\text{-}O}}$		**OCO angle**	$\mathbf{r_{C\text{-}Cu}}$	$\mathbf{r_{O\text{-}Cu}}$	$\mathbf{E_{ads}}$
0	physi.	1.17	1.17	179.5			-0.35
5	physi.	1.17	1.17	177.9			-0.38
10	physi.	1.17	1.17	175.9			-0.38
15	chemi.	1.23	1.28	130.3	2.03	2.09	-0.56
20	chemi.	1.24	1.29	127.0	2.04	2.08	-0.90
25	chemi.	1.26	1.29	124.2	2.04	2.09	-1.31

5. The combined effect of electric field and excess electron- Using dipole sheet method

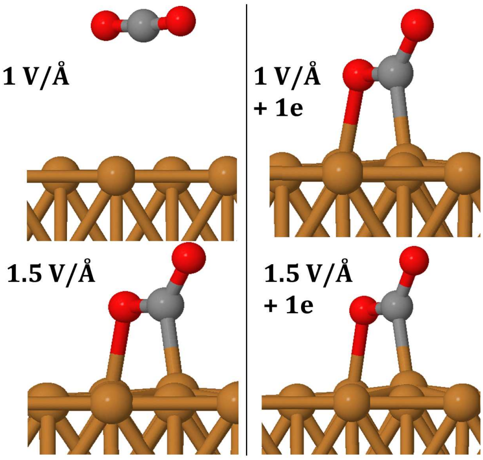

Figure A2. 4: The most stable CO_2 adsorption mode on Cu (111).

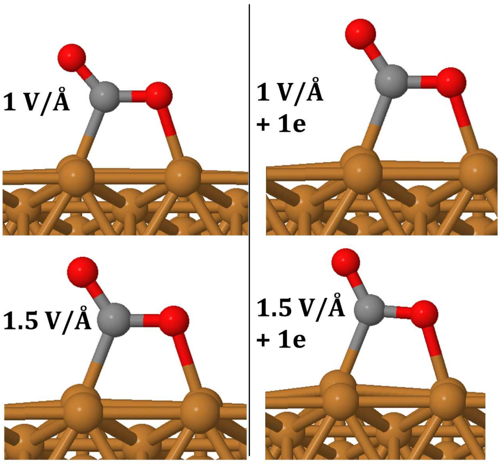

Figure A2. 5: The most stable CO_2 adsorption mode on Cu (211).

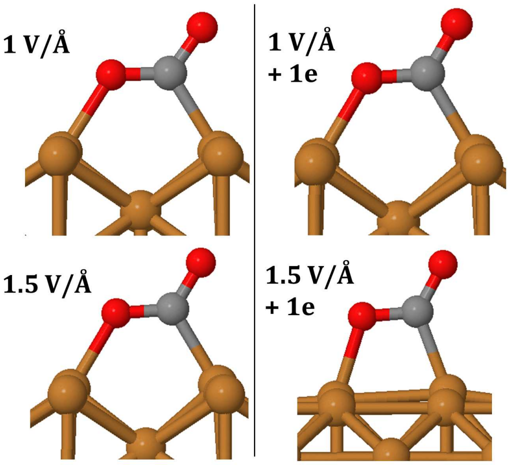

Figure A2. 6: The most stable CO_2 adsorption mode on Cu (110).

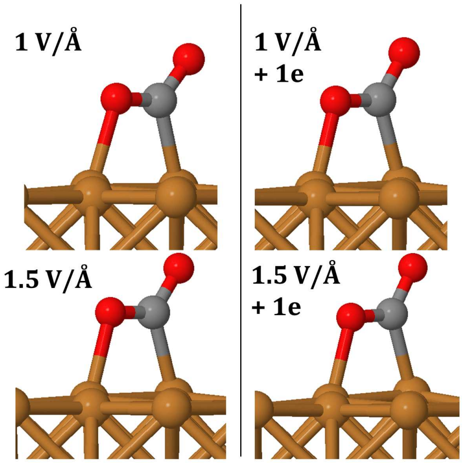

Figure A2. 7: The most stable CO_2 adsorption mode on Cu (001).

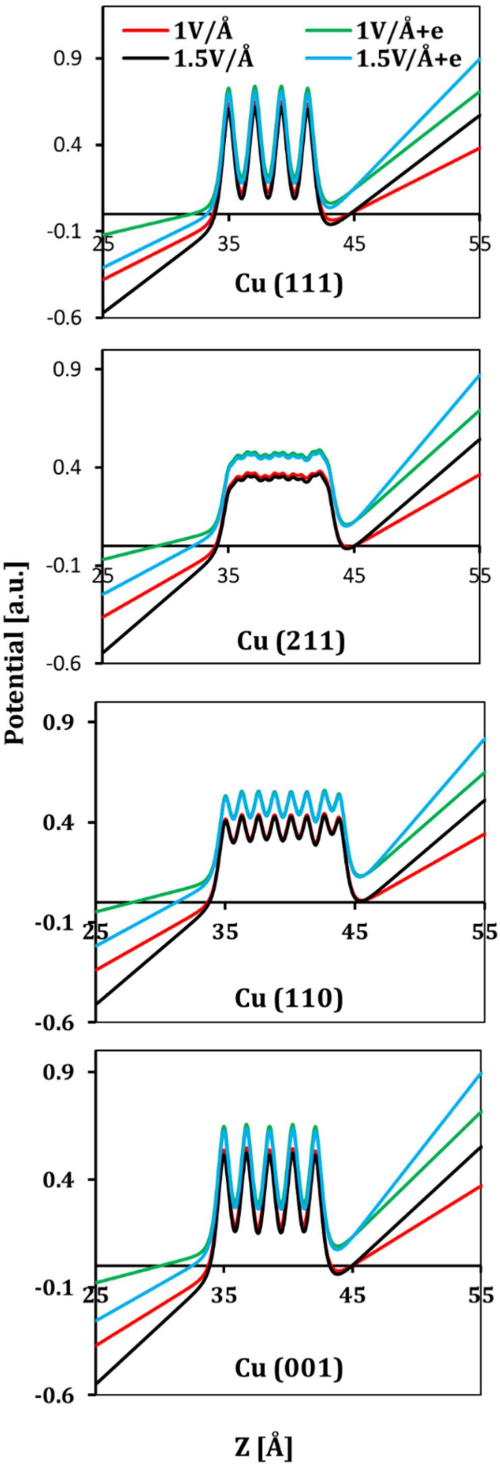

Figure A2. 8: Potential distribution around the Cu surface for different combined electric field and excess electron situations.

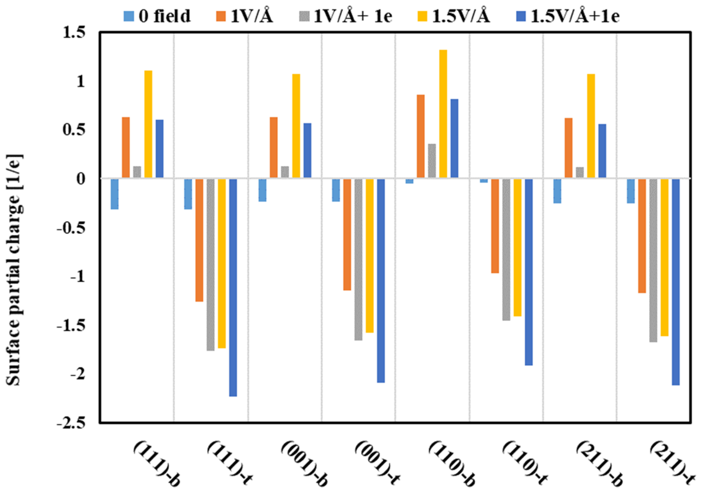

Figure A2. 9: Surface partial charges as a function of field and excess electron combination- “b” and “t” are referred to bottom and top layers of the slabs, respectively.

Table A2. 7: Bond lengths(Å), angles(°), and adsorption energies(eV) for the most stable CO_2 adsorption mode on Cu (111).

V [V]	**Ads. mode**	$\mathbf{r_{C\text{-}O}}$		**OCO angle**	$\mathbf{r_{C\text{-}Cu}}$	$\mathbf{r_{O\text{-}Cu}}$	$\mathbf{E_{ads}}$
0V/Å	physi.	1.17	1.17	179.9			-0.32
0V/Å+e	physi.	1.17	1.17	177.7			-0.33
1V/Å	physi.	1.17	1.18	175.3			-0.39
1V/Å+e	chemi.	1.24	1.29	127.5	2.04	2.08	-0.58
1.5V/Å	chemi.	1.24	1.29	127.0	2.04	2.07	-0.62
1.5V/Å+e	chemi.	1.25	1.29	124.8	2.06	2.12	-1.07

Table A2. 8: Bond lengths(Å), angles(°), and adsorption energies(eV) for the most stable CO_2 adsorption mode on Cu (211).

V [V]	**Ads. mode**	$\mathbf{r_{C\text{-}O}}$		**OCO angle**	$\mathbf{r_{C\text{-}Cu}}$	$\mathbf{r_{O\text{-}Cu}}$	$\mathbf{E_{ads}}$
0V/Å	physi.	1.17	1.18	179.5			-0.31
0V/Å+e	physi.	1.17	1.17	176.4			-0.30
1V/Å	chemi.	1.24	1.29	128.9	2.00	2.02	-0.78
1V/Å+e	chemi.	1.25	1.3	124.3	2.01	2.03	-1.45
1.5V/Å	chemi.	1.25	1.3	124.7	2.01	2.02	-1.30
1.5V/Å+e	chemi.	1.27	1.31	121.2	2.03	2.05	-2.16

Table A2. 9: Bond lengths(Å), angles(°), and adsorption energies(eV) for the most stable CO_2 adsorption mode on Cu (110).

V [V]	**Ads. mode**	$\mathbf{r_{C\text{-}O}}$		**OCO angle**	$\mathbf{r_{C\text{-}Cu}}$	$\mathbf{r_{O\text{-}Cu}}$	$\mathbf{E_{ads}}$
0V/Å	physi.	1.17	1.18	179.7			-0.34
0V/Å+e	chemi.	1.23	1.27	131.3	2.02	2.02	-0.33
1V/Å	chemi.	1.24	1.29	127.3	2.02	2.01	-0.67
1V/Å+e	chemi.	1.25	1.30	124.3	2.03	2.03	-1.12
1.5V/Å	chemi.	1.25	1.30	124.3	2.03	2.03	-1.11
1.5V/Å+e	chemi.	1.26	1.30	122.6	2.04	2.06	-1.70

Table A2. 10: Bond lengths(Å), angles(°), and adsorption energies(eV) for the most stable CO_2 adsorption mode on Cu (001).

V [V]	**Ads. mode**	$\mathbf{r_{C\text{-}O}}$		**OCO angle**	$\mathbf{r_{C\text{-}Cu}}$	$\mathbf{r_{O\text{-}Cu}}$	$\mathbf{E_{ads}}$
0V/Å	physi.	1.17	1.17	179.4			-0.33
0V/Å+e	physi.	1.17	1.18	176.8			-0.33
1V/Å	chemi.	1.23	1.27	131.9	2.03	2.08	-0.43
1V/Å+e	chemi.	1.24	1.29	126.7	2.04	2.07	-0.89
1.5V/Å	chemi.	1.24	1.28	127.4	2.04	2.08	-0.85
1.5V/Å+e	chemi.	1.26	1.29	124.0	2.04	2.09	-1.43

6. PDOS for combined electric field and excess electron effect

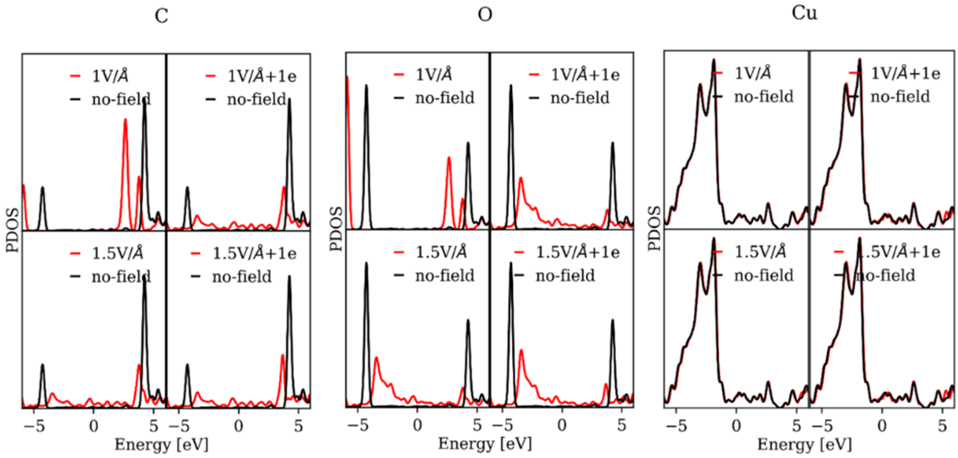

Figure A2. 10: Projected density of states for CO_2 adsorption on Cu (111) surface.

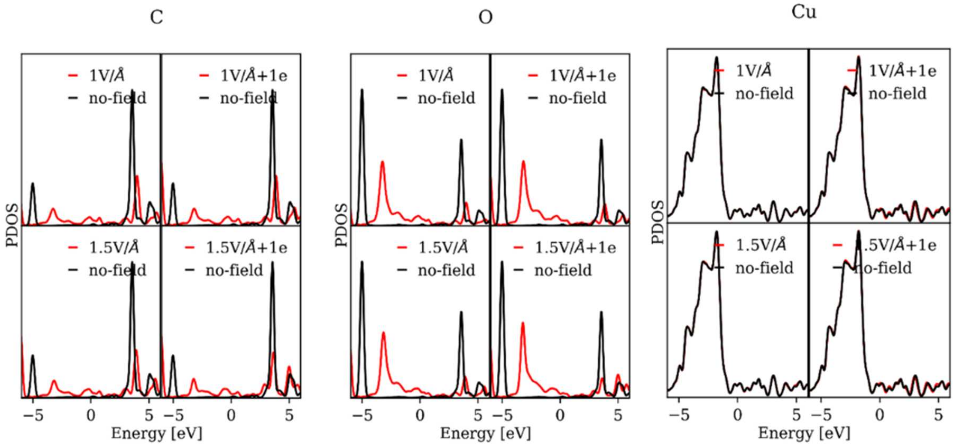

Figure A2. 11: Projected density of states for CO_2 adsorption on Cu (211) surface.

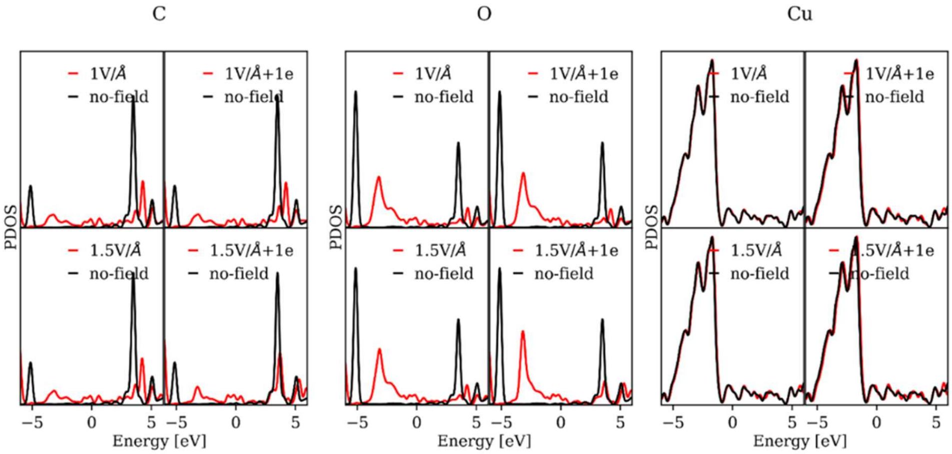

Figure A2. 12: Projected density of states for CO_2 adsorption on Cu (110) surface.

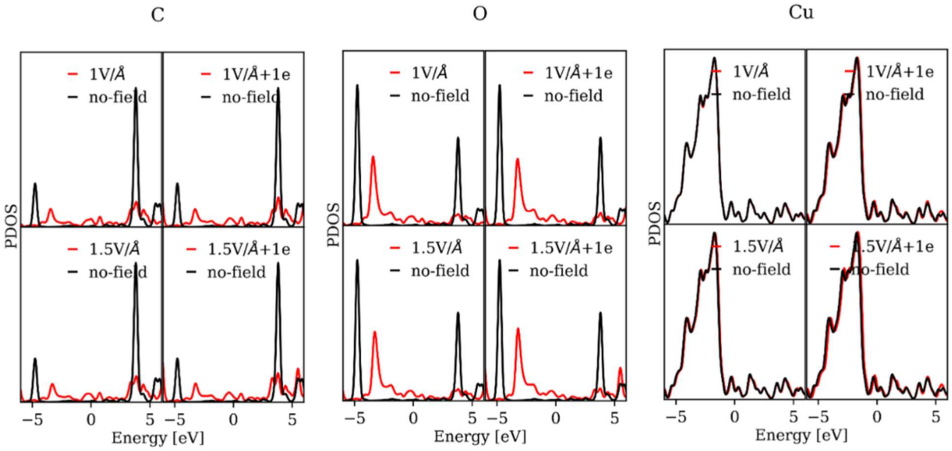

Figure A2. 13: Projected density of states for CO_2 adsorption on Cu (001) surface.

7. Hirshfeld charges of the surface atoms and adsorbed molecule using the dipole sheet method

Table A2. 11: Partial charges of the upper layer atoms of the Cu (111) and the adsorbed CO_2 molecule- bonded atoms from the molecule and the surface are indicated in the same colors.

Atom	**0V/Å**	**0V/Å +e**	**1V/Å**	**1V/Å +e**	**1.5V/Å**	**1.5V/Å +e**
Cu	0.011	0.011	-0.045	-0.051	-0.05	-0.064
Cu	0.01	0.011	-0.04	-0.053	-0.053	-0.065
Cu	0.011	0.011	-0.04	-0.024	-0.025	-0.036
Cu	0.011	0.011	-0.042	-0.033	-0.029	-0.045
Cu	0.011	0.011	-0.04	-0.055	-0.053	-0.068
Cu	0.01	0.011	-0.041	-0.05	-0.049	-0.063
Cu	0.01	0.011	-0.04	-0.021	-0.024	-0.025
Cu	0.011	0.011	-0.03	-0.013	-0.011	-0.025
Cu	-0.01	-0.025	-0.031	-0.255	-0.258	-0.261
Cu	-0.01	-0.027	-0.04	-0.048	-0.047	-0.06
Cu	-0.01	-0.026	-0.04	-0.035	-0.03	-0.044
Cu	0.011	0.011	-0.041	-0.005	-0.002	-0.011
Cu	0.011	0.011	-0.04	-0.052	-0.051	-0.064
Cu	0.011	0.011	-0.041	0.02	0.018	0.025
Cu	0.01	0.011	-0.041	-0.054	-0.052	-0.067
Cu	0.011	0.011	-0.04	-0.051	-0.048	-0.065
Cu	0.011	0.011	-0.042	-0.051	-0.05	-0.065
Cu	-0.01	-0.024	-0.041	-0.051	-0.048	-0.065
Cu	-0.01	-0.026	-0.041	-0.03	-0.031	-0.038
Cu	-0.011	-0.027	-0.033	-0.047	-0.048	-0.059
Cu	0.001	-0.012	-0.029	-0.052	-0.051	-0.066
Cu	0.011	0.011	-0.04	-0.012	-0.012	-0.025
Cu	-0.011	-0.027	-0.041	-0.051	-0.05	-0.065
Cu	-0.011	-0.027	-0.041	-0.052	-0.051	-0.065
Cu	-0.012	-0.028	-0.04	-0.052	-0.051	-0.064
Cu	-0.011	-0.026	-0.041	-0.052	-0.052	-0.066
Cu	-0.011	-0.027	-0.04	-0.053	-0.052	-0.067
Cu	-0.011	-0.027	-0.041	-0.054	-0.052	-0.068
Cu	-0.01	-0.026	-0.023	-0.051	-0.05	-0.065
Cu	-0.011	-0.027	-0.031	-0.053	-0.052	-0.066
C	1.525	1.52	1.454	1.401	1.396	1.369
O	-0.791	-0.8	-0.777	-0.745	-0.74	-0.778
O	-0.783	-0.799	-0.78	-0.96	-0.961	-1.027
Partial charge of the molecule	-0.049	-0.079	-0.103	-0.304	-0.305	-0.436

Table A2. 12: Partial charges of the upper layer atoms of the Cu (211) and the adsorbed CO_2 molecule- bonded atoms from the molecule and the surface are indicated in the same colors.

Atom	**0V/Å**	**0V/Å +e**	**1V/Å**	**1V/Å +e**	**1.5V/Å**	**1.5V/Å +e**
Cu	-0.013	-0.017	-0.008	-0.007	-0.008	-0.009
Cu	-0.013	-0.015	-0.014	-0.016	-0.016	-0.017
Cu	-0.012	-0.015	-0.016	-0.017	-0.017	-0.017
Cu	-0.012	-0.015	-0.016	-0.018	-0.018	-0.019
Cu	-0.013	-0.017	-0.007	-0.008	-0.008	-0.011
Cu	-0.012	-0.015	-0.016	-0.018	-0.018	-0.019
Cu	-0.013	-0.016	-0.016	-0.017	-0.018	-0.018
Cu	-0.012	-0.015	-0.017	-0.018	-0.019	-0.02
Cu	-0.012	-0.016	-0.016	-0.018	-0.018	-0.019
Cu	-0.012	-0.016	-0.017	-0.019	-0.019	-0.02
Cu	-0.015	-0.025	-0.023	-0.031	-0.032	-0.041
Cu	-0.01	-0.024	-0.019	-0.025	-0.025	-0.03
Cu	-0.015	-0.027	-0.021	-0.029	-0.029	-0.037
Cu	-0.014	-0.025	-0.029	-0.038	-0.038	-0.048
Cu	-0.021	-0.031	-0.012	-0.015	-0.015	-0.02
Cu	-0.013	-0.024	-0.029	-0.039	-0.039	-0.047
Cu	-0.014	-0.025	-0.024	-0.033	-0.033	-0.042
Cu	-0.014	-0.025	-0.022	-0.031	-0.03	-0.038
Cu	-0.014	-0.025	-0.031	-0.041	-0.041	-0.05
Cu	-0.014	-0.025	-0.032	-0.042	-0.041	-0.05
Cu	-0.008	-0.041	-0.285	-0.309	-0.304	-0.304
Cu	0.004	-0.023	0.004	-0.017	-0.017	-0.043
Cu	-0.003	-0.039	-0.05	-0.089	-0.077	-0.114
Cu	-0.002	-0.037	-0.045	-0.073	-0.07	-0.097
Cu	0.017	-0.01	0.001	0.002	0.001	0.003
Cu	-0.001	-0.035	-0.041	-0.067	-0.064	-0.092
Cu	-0.006	-0.038	-0.054	-0.082	-0.078	-0.107
Cu	-0.002	-0.037	-0.046	-0.076	-0.073	-0.102
Cu	0.009	-0.027	-0.018	-0.043	-0.039	-0.063
Cu	-0.003	-0.037	-0.047	-0.077	-0.074	-0.102
C	1.528	1.522	1.422	1.381	1.385	1.27
O	-0.768	-0.782	-0.906	-0.994	-0.983	-1.044
O	-0.77	-0.786	-0.716	-0.742	-0.738	-0.738
Partial charge of the molecule	-0.01	-0.046	-0.2	-0.355	-0.336	-0.512

Table A2. 13: Partial charges of the upper layer atoms of the Cu (110) and the adsorbed CO_2 molecule- bonded atoms from the molecule and the surface are indicated in the same colors.

Atom	0V/Å	0V/Å +e	1V/Å	1V/Å +e	1.5V/Å	1.5V/Å +e
Cu	0.001	0.001	0.001	0.003	0.002	0.002
Cu	0.001	0.002	0.001	0.002	0.001	0.002
Cu	-0.006	0.008	0.011	0.011	0.011	0.004
Cu	0.001	0.001	0.001	0.003	0.002	0.002
Cu	-0.003	0.009	0.011	0.011	0.012	0.003
Cu	0.001	0.001	0.001	0.003	0.002	0.002
Cu	0.001	0.001	0.002	0.001	0.002	0.002
Cu	0.001	0.001	0.001	0.001	0.002	0.002
Cu	0.001	-0.001	-0.002	-0.002	-0.003	0.001
Cu	0.001	0.001	0.001	0.001	0.002	0.002
Cu	0.001	-0.001	-0.002	-0.002	-0.002	0.002
Cu	0.001	0.001	0.002	0.001	0.002	0.002
Cu	0.011	0.013	-0.002	-0.02	-0.018	0.01
Cu	-0.003	-0.022	-0.041	-0.067	-0.064	-0.052
Cu	-0.004	-0.016	-0.033	-0.059	-0.054	-0.057
Cu	-0.005	-0.027	-0.05	-0.074	-0.073	-0.084
Cu	-0.003	0.025	0.017	0.014	0.013	-0.289
Cu	-0.003	-0.026	-0.046	-0.073	-0.07	-0.093
Cu	-0.002	-0.008	-0.022	-0.048	-0.041	-0.056
Cu	-0.004	-0.033	-0.058	-0.081	-0.082	-0.098
Cu	-0.012	0.013	0.002	-0.015	-0.014	-0.037
Cu	-0.004	-0.017	-0.032	-0.058	-0.053	-0.071
Cu	-0.005	-0.022	-0.041	-0.066	-0.063	-0.087
Cu	-0.005	-0.028	-0.049	-0.073	-0.072	-0.09
Cu	-0.013	-0.004	-0.019	-0.034	-0.032	-0.06
Cu	-0.007	-0.02	-0.039	-0.064	-0.06	-0.085
Cu	0.025	-0.231	-0.243	-0.26	-0.261	-0.059
Cu	-0.005	-0.023	-0.042	-0.07	-0.066	-0.098
Cu	0.007	-0.006	-0.014	-0.03	-0.03	-0.072
Cu	-0.004	-0.02	-0.038	-0.063	-0.06	-0.09
C	1.463	1.422	1.327	1.309	1.307	1.276
O	-0.734	-0.827	-0.864	-0.94	-0.938	-0.742
O	-0.739	-0.715	-0.702	-0.725	-0.725	-1.029
Partial charge of the molecule	-0.01	-0.12	-0.239	-0.356	-0.356	-0.495

Table A2. 14: Partial charges of the upper layer atoms of the Cu (110) and the adsorbed CO_2 molecule- bonded atoms from the molecule and the surface are indicated in the same colors.

Atom	**0V/Å**	**0V/Å +e**	**1V/Å**	**1V/Å +e**	**1.5V/Å**	**1.5V/Å +e**
Cu	-0.011	-0.031	-0.042	-0.06	-0.058	-0.074
Cu	-0.011	-0.032	-0.046	-0.066	-0.062	-0.081
Cu	-0.012	-0.032	-0.038	-0.057	-0.053	-0.071
Cu	-0.009	-0.026	-0.025	-0.040	-0.038	-0.053
Cu	-0.012	-0.031	-0.038	-0.055	-0.053	-0.069
Cu	-0.011	-0.031	-0.039	-0.063	-0.056	-0.079
Cu	-0.011	-0.031	-0.039	-0.062	-0.056	-0.078
Cu	-0.010	-0.029	-0.034	-0.050	-0.048	-0.064
Cu	-0.012	-0.032	-0.036	-0.056	-0.052	-0.071
Cu	-0.011	-0.032	-0.04	-0.062	-0.055	-0.079
Cu	-0.005	-0.026	-0.022	-0.035	-0.032	-0.049
Cu	-0.012	-0.025	-0.011	-0.016	-0.016	-0.028
Cu	-0.013	-0.037	-0.023	-0.032	-0.032	-0.042
Cu	-0.011	-0.032	-0.042	-0.059	-0.056	-0.073
Cu	-0.009	-0.03	-0.035	-0.049	-0.049	-0.064
Cu	-0.001	-0.002	0.007	0.008	0.006	0.012
Cu	-0.009	-0.03	-0.031	-0.044	-0.044	-0.057
Cu	-0.011	-0.031	-0.033	-0.047	-0.048	-0.062
Cu	-0.012	-0.033	-0.008	-0.018	-0.019	-0.026
Cu	-0.003	-0.033	-0.245	-0.266	-0.261	-0.279
Cu	0.001	-0.018	-0.003	-0.018	-0.017	-0.030
Cu	-0.011	-0.031	-0.042	-0.059	-0.057	-0.073
Cu	-0.012	-0.033	-0.042	-0.058	-0.057	-0.072
Cu	-0.013	-0.032	-0.025	-0.033	-0.032	-0.041
C	1.524	1.521	1.438	1.397	1.403	1.369
O	-0.777	-0.795	-0.737	-0.757	-0.757	-0.783
Partial charge of the molecule	-0.031	-0.07	-0.192	-0.335	-0.317	-0.461

Appendix 3

Plasma-catalytic Ammonia Reforming of Methane over Cu-based Catalysts for the Production of HCN and H_2 at Reduced Temperature - Supporting Information to Chapter 5

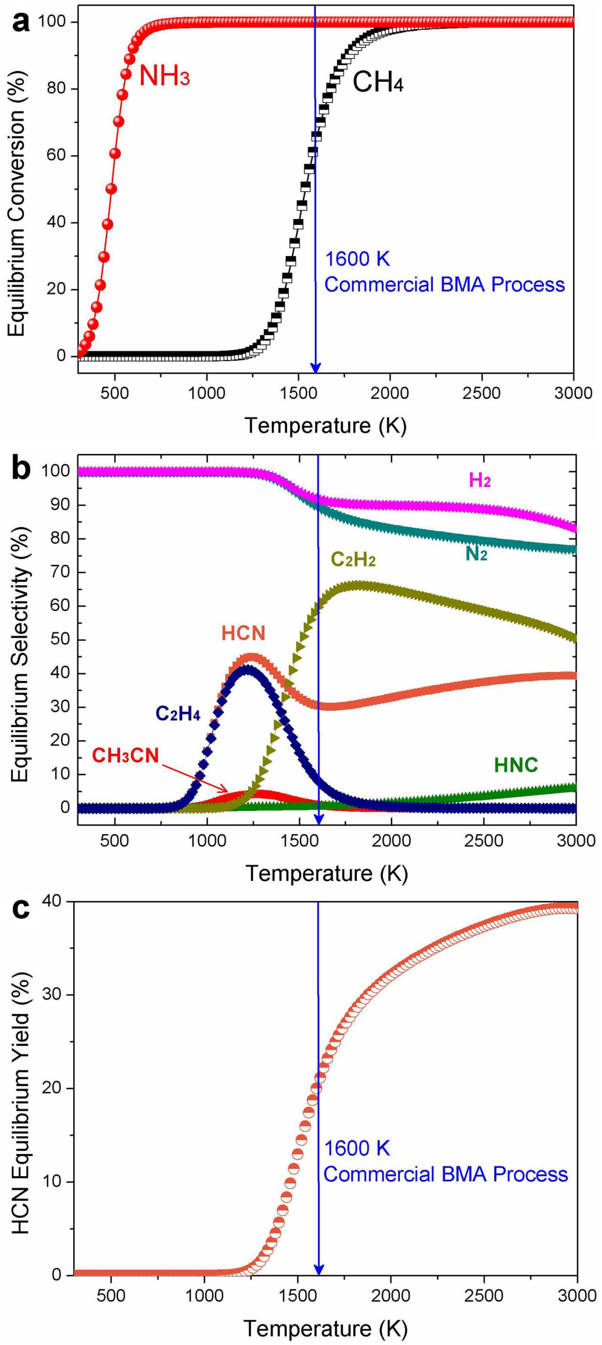

Figure A3. 1: Thermodynamic equilibrium of the BMA process for HCN synthesis at atmospheric pressure. a) equilibrium conversion, b) equilibrium selectivity, and c) HCN equilibrium yield.

Experimental methods

To provide a consistent picture for the calculations conducted, some experimental results (carried out by my colleagues) are also provided here.

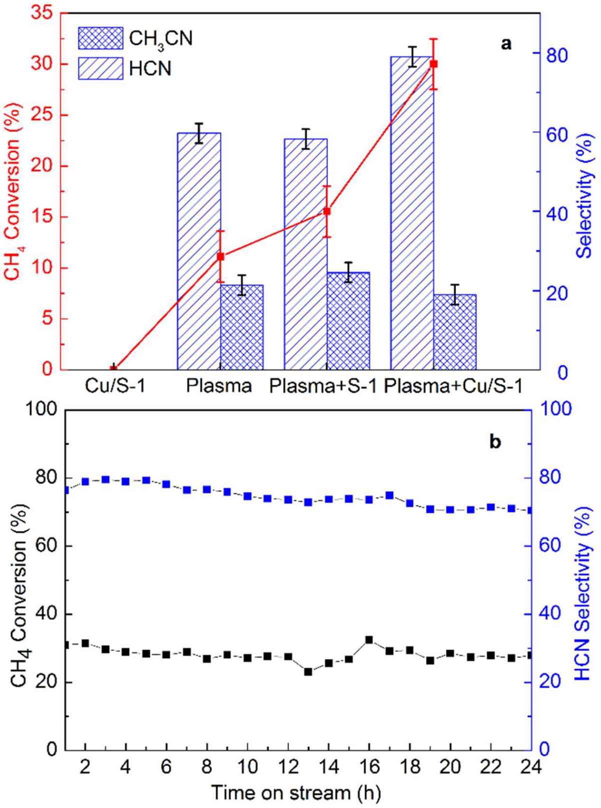

Figure A3. 2: CH_4 conversion and selectivity towards HCN and CH_3CN at 673 K, for catalyst only, plasma only, plasma + S-1 support, and plasma + Cu/S-1 catalyst (a), and for 24 h, to test the stability of Cu/S-1 catalyst (b) (Reaction condition: 10 wt.% Cu loading, CH_4: NH_3 = 1: 2, GHSV: 1529 h^{-1}, discharge length: 5 cm, the error bars are obtained from five repetitions of the experiment).

X-ray diffraction (XRD) patterns were recorded on a SmartLab 9KW X-ray diffractometer using Cu K_α radiation (λ=0.15406 nm). The X-ray tube was operated at 240 kV and 50 mA. The data was recorded at 5°-80°. The scanning speed was 10 °/min with a step size of 0.02°.

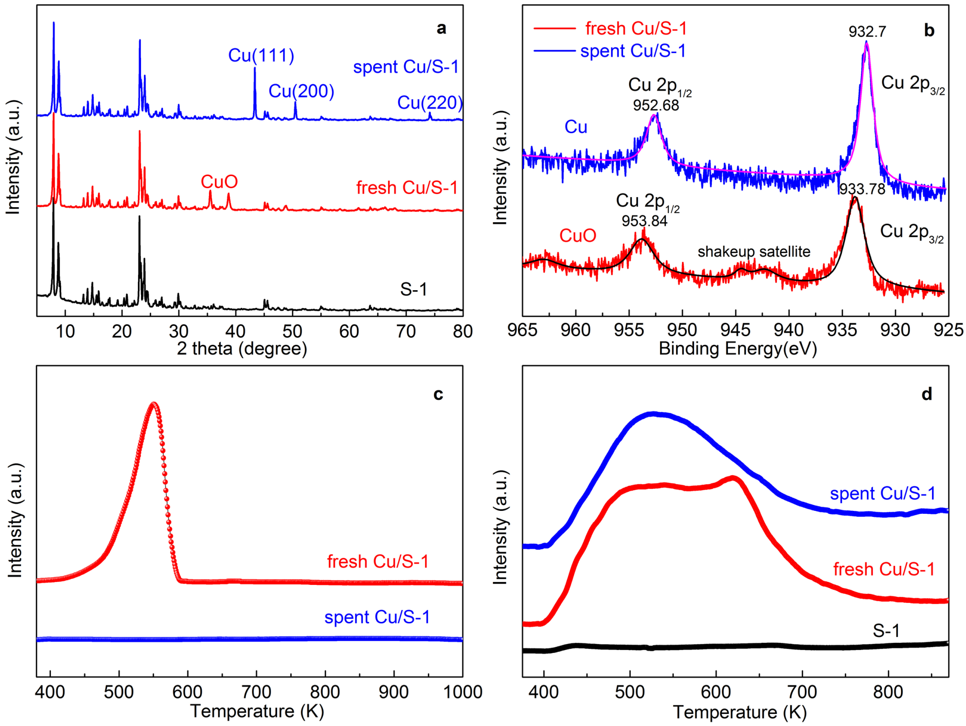

Figure A3. 3: Characterization results of the fresh and spent Cu/S-1 catalysts. XRD patterns (a); XPS spectra (b); H_2-TPR profiles (c) and NH_3-TPD results (d).

The Princeton ICCD spectrometer (SP 2758) was used to record optical emission spectra (OES) of the CH_4/NH_3 DBD plasma in the range of 300-900 nm.

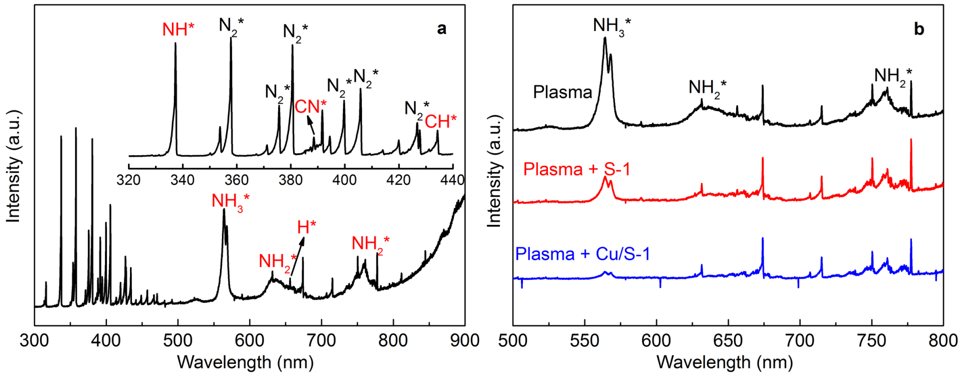

Figure A3. 4: Optical emission spectra of CH_4/NH_3 DBD plasma at 673 K, without catalyst (a), and comparison between plasma-only, plasma + S-1, and plasma + Cu/S-1 catalyst (b).

DFT calculations

- **Dimensions of the supercells used for the calculations (all in Å)**

Cu (111): 10.23 × 08.86 × 30.00

Cu (200): 10.23 × 10.23 × 30.00

Cu (220): 10.23 × 10.85 × 30.00

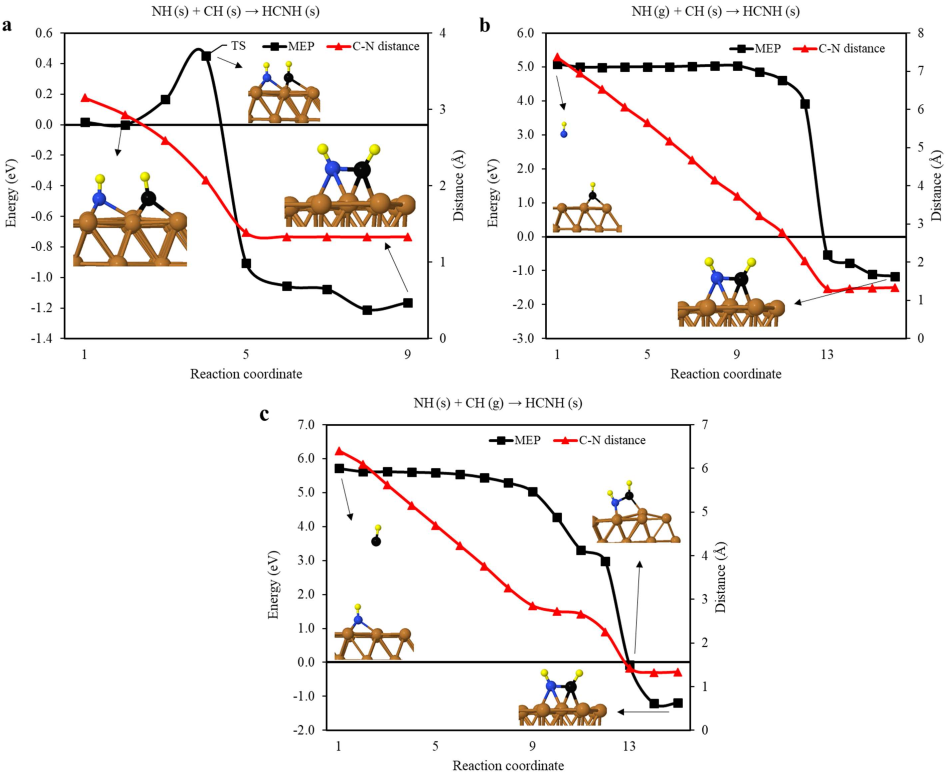

Figure A3. 5: MEP for the interaction of pre-adsorbed NH and CH (a), gas-phase NH with pre-adsorbed CH (b), and gas-phase CH with pre-adsorbed NH (c) to form HCNH. All energies are referenced with respect to the energy of the pre-adsorbed N and CH on Cu (111) - Brown, black, blue, and yellow colors correspond to Cu, C, N, and H atoms, respectively.

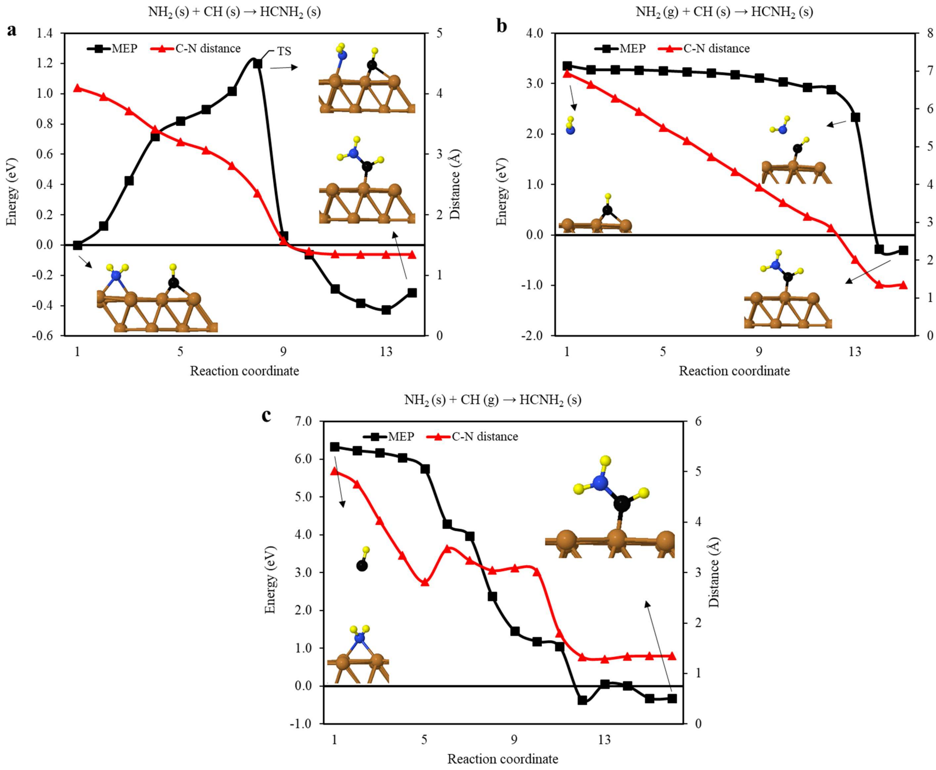

$NH_2 (s) + CH (s) \rightarrow HCNH_2 (s)$

$NH_2 (g) + CH (s) \rightarrow HCNH_2 (s)$

$NH_2 (s) + CH (g) \rightarrow HCNH_2 (s)$

Figure A3. 6: MEP for the interaction of pre-adsorbed NH_2 and CH (a), gas-phase NH_2 with pre-adsorbed CH (b), and gas-phase CH with pre-adsorbed NH_2 (c) to form $HCNH_2$. All energies are referenced with respect to the energy of the pre-adsorbed NH_2 and CH on Cu (111) - Brown, black, blue, and yellow colors correspond to Cu, C, N, and H atoms, respectively.

Bibliography

[1] *Evidence — Facts – Climate Change: Vital Signs of the Planet - Date Accessed: 2020-07-15.* URL: `https://climate.nasa.gov/evidence/`.

[2] Svante Arrhenius. “On the Influence of Carbonic Acid in the Air upon the Temperature of the Ground”. In: *Philosophical Magazine and Journal of Science Series* 5 (1896), pp. 237–276. URL: `http://www.globalwarmingart.com/`.

[3] L.A. Meyer Pachauri and R.K. *IPCC, 2014: Climate Change 2014: Synthesis Report. Contribution of Working Groups I, II and III to the Fifth Assessment Report of the Intergovernmental Panel on Climate Change. IPCC, Geneva, Switzerland, 151 pp - Date Accessed: 2020-07-20.* 2014. URL: `https://www.ipcc.ch/site/assets/uploads/2018/02/AR5_SYR_FINAL_Front_matters.pdf`.

[4] Isabelle Weindl et al. “Livestock in a changing climate: Production system transitions as an adaptation strategy for agriculture”. In: *Environmental Research Letters* 10.9 (Sept. 2015), p. 94021. URL: `https://doi.org/10.1088%2F1748-9326%2F10%2F9%2F094021`.

[5] W. R. L. Anderegg et al. “Expert credibility in climate change”. In: *Proceedings of the National Academy of Sciences* 107.27 (July 2010), pp. 12107–12109. URL: `http://www.pnas.org/cgi/doi/10.1073/pnas.1003187107`.

[6] Naomi Oreskes. “Beyond the Ivory Tower: The scientific consensus on climatic change”. In: *Science* 306.5702 (Dec. 2004), p. 1686.

[7] Peter T. Doran and Maggie Kendall Zimmerman. “Examining the Scientific Consensus on Climate Change”. In: *Eos, Transactions American Geophysical Union* 90.3 (Jan. 2009), p. 22. URL: `http://doi.wiley.com/10.1029/2009EO030002`.

[8] NASA. *yearly temperature anomalies from 1880 to 2019 - Date Accessed: 2020-07-15.* 2020. URL: `https://climate.nasa.gov/system/internal_resources/details/original/1987_yearly_temperature_anomalies_from_1880_to_2019.jpeg`.

[9] NCEI. *Global Climate Change Indicators — Monitoring References - Date Accessed: 2020-07-20.* URL: `https://www.ncdc.noaa.gov/monitoring-references/faq/indicators.php`.

[10] R. S. Nerem et al. “Main Greenhouse Gases — Center for Climate and Energy Solutions”. In: *Proceedings of the National Academy of Sciences* 115.9 (2017), pp. 2022–2025.

[11] *AR5 Climate Change 2014: Mitigation of Climate Change — IPCC - Date Accessed: 2020-07-15.* URL: `https://www.ipcc.ch/report/ar5/wg3/`.

[12] *Global Greenhouse Gas Emissions Data — Greenhouse Gas (GHG) Emissions — US EPA- Date Accessed: 2020-10-20.* URL: `https://www.epa.gov/ghgemissions/global-greenhouse-gas-emissions-data`.

[13] R. B. Jackson et al. *Methane removal and atmospheric restoration.* June 2019. URL: `https://www.nature.com/articles/s41893-019-0299-x`.

[14] Young Sam Oh et al. “A highly active catalyst, Ni/Ce-ZrO2/θ-Al2O3, for on-site H2 generation by steam methane reforming: Pretreatment effect”. In: *International Journal of Hydrogen Energy* 28.12 (Dec. 2003), pp. 1387–1392.

[15] Jun Tae Song et al. *Towards higher rate electrochemical CO2 conversion: From liquid-phase to gas-phase systems.* Mar. 2019.

[16] Dunfeng Gao et al. “Plasma-Activated Copper Nanocube Catalysts for Efficient Carbon Dioxide Electroreduction to Hydrocarbons and Alcohols”. In: *ACS Nano* 11.5 (May 2017), pp. 4825–4831.

[17] Rulle Reske et al. “Particle Size Effects in the Catalytic Electroreduction of CO 2 on Cu Nanoparticles”. In: *Journal of the American Chemical Society* 136.19 (May 2014), pp. 6978–6986. URL: `https://pubs.acs.org/doi/10.1021/ja500328k`.

[18] W. Somers et al. “Temperature influence on the reactivity of plasma species on a nickel catalyst surface: An atomic scale study”. In: *Catalysis Today* 211 (Aug. 2013), pp. 131–136.

[19] Jens Sehested. “Four challenges for nickel steam-reforming catalysts”. In: *Catalysis Today.* Vol. 111. 1-2. Elsevier, Jan. 2006, pp. 103–110.

[20] Ramses Snoeckx and Annemie Bogaerts. *Plasma technology-a novel solution for CO2 conversion?* Oct. 2017.

[21] Mohcin Akri et al. “Atomically dispersed nickel as coke-resistant active sites for methane dry reforming”. In: *Nature Communications* 10.1 (Dec. 2019), pp. 1–10. URL: `https://doi.org/10.1038/s41467-019-12843-w`.

[22] L. Andrussow. “Über die katalytische Oxydation von Ammoniak-Methan-Gemischen zu Blausäure”. In: *Angewandte Chemie* 48.37 (Sept. 1935), pp. 593–595.

[23] Jaime Gómez-Díaz and Nria López. “Mechanistic switch between oxidative (andrussow) and nonoxidative (degussa) formation of HCN on Pt(111) by density functional theory”. In: *Journal of Physical Chemistry C* 115.13 (Apr. 2011), pp. 5667–5674.

[24] John Meurig Thomas. “Handbook Of Heterogeneous Catalysis. 2., completely revised and enlarged Edition. Vol. 1-8. Edited by G. Ertl, H. Knözinger, F. Schüth, and J. Weitkamp.” In: *Angewandte Chemie International Edition* 48.19 (Apr. 2009), pp. 3390–3391. URL: `https://onlinelibrary.wiley.com/doi/full/10.1002/anie.200901598`.

[25] T. K. Sherwood, E. R. Gilliland, and S. W. Ing. “Hydrogen Cyanide Synthesis from Its Elements and from Ammonia and Carbon”. In: *Industrial and Engineering Chemistry* 52.7 (July 1960), pp. 601–604. URL: `https://pubs.acs.org/doi/abs/10.1021/ie50607a030`.

[26] Lars C. Grabow et al. “Descriptor-based analysis applied to HCN synthesis from NH3 and CH4”. In: *Angewandte Chemie - International Edition* 50.20 (May 2011), pp. 4601–4605.

[27] G. E. Johnson et al. “Hydrogen cyanide produced from coal and ammonia”. In: *Industrial and Engineering Chemistry Process Design and Development* 7.1 (Jan. 1968), pp. 137–143. URL: `https://pubs.acs.org/doi/abs/10.1021/i260025a027`.

[28] Alexander Fridman. *Plasma chemistry.* Vol. 9780521847. Cambridge University Press, Jan. 2008, pp. 1–978. URL: `/core/books/plasma-chemistry/842EA140F5D8C59F15AB82544A3E44CC`.

[29] E. C. Neyts and A. Bogaerts. “Understanding plasma catalysis through modelling and simulation - A review”. In: *Journal of Physics D: Applied Physics* 47.22 (June 2014).

[30] J Christopher Whitehead. “Plasma–catalysis: the known knowns, the known unknowns and the unknown unknowns”. In: *Journal of Physics D: Applied Physics* 49.24 (2016), p. 243001. URL: `http://dx.doi.org/10.1088/0022-3727/49/24/243001`.

[31] L Zhang et al. “Synergistic catalytic removal NOX and the mechanism of plasma and hydrocarbon gas”. In: *AIP Adv.* 6 (2016), p. 75015.

[32] Danhua Mei et al. “Plasma-photocatalytic conversion of CO2 at low temperatures: Understanding the synergistic effect of plasma-catalysis”. In: *Applied Catalysis B: Environmental* 182 (Mar. 2016), pp. 525–532.

[33] J Kim, D B Go, and J C Hicks. “Synergistic effects of plasma-catalyst interactions for CH4 activation”. In: *Phys. Chem. Chem. Phys.* 19 (2017), p. 13010.

[34] Shaodong Zhou et al. *Bond Activation by Metal-Carbene Complexes in the Gas Phase.* Mar. 2016. URL: `https://pubs.acs.org/doi/abs/10.1021/acs.accounts.5b00023`.

[35] H.-H. Kim et al. “Oxygen Isotope (18O2) Evidence on the Role of Oxygen in the Plasma-Driven Catalysis of VOC Oxidation”. In: *Catal. Lett.* 141 (2011), p. 277.

[36] A Maciuca, C Batiot-Dupeyrat, and J.-M. Tatibouet. “Synergetic effect by coupling photocatalysis with plasma for low VOCs concentration removal from air”. In: *Appl. Catal., B* 125 (2012), p. 432.

[37] I Jõgi et al. “Oxidation of nitrogen oxide in hybrid plasma-catalytic reactors based on DBD and Fe2O3*”. In: *Eur. Phys. J.: Appl. Phys.* 61 (2013), p. 24305.

[38] A Mizuno. “Generation of non-thermal plasma combined with catalysts and their application in environmental technology”. In: *Catal. Today* 211 (2013), p. 2.

[39] E Tatarova et al. “Plasmas for environmental issues: from hydrogen production to 2D materials assembly”. In: *Plasma Sources Sci. Technol.* 23 (2014), p. 63002.

[40] H.-H. Kim et al. “Plasma Catalysis for Environmental Treatment and Energy Applications”. In: *Plasma Chem. Plasma Process.* 36 (2016), p. 45.

[41] H Lee and H Sekiguchi. “Plasma-catalytic hybrid system using spouted bed with a gliding arc discharge: CH4 reforming as a model reaction”. In: *J. Phys. D: Appl. Phys.* 44 (2011), p. 274008.

[42] Xin Tu et al. “Dry reforming of methane over a Ni/Al2O3 catalyst in a coaxial dielectric barrier discharge reactor”. In: *J. Phys. D: Appl. Phys.* 44.27 (July 2011), p. 274007.

[43] Erik C. Neyts. “Plasma-Surface Interactions in Plasma Catalysis”. In: *Plasma Chemistry and Plasma Processing* (2016).

[44] Annemie Bogaerts et al. *The 2020 plasma catalysis roadmap.* Oct. 2020. URL: `https://doi.org/10.1088/1361-6463/ab9048`.

[45] Erik C. Neyts et al. “Plasma Catalysis: Synergistic Effects at the Nanoscale”. In: *Chemical Reviews* 115.24 (Nov. 2015), pp. 13408–13446.

[46] Wesley Somers. “Atomic scale simulations of the interactions of plasma species on nickel catalyst surfaces”. In: *University of Antwerp* (2015). URL: `https://hdl.handle.net/10067/1279150151162165141`.

[47] Ruixing Li et al. “Plasma catalysis for CO2 decomposition by using different dielectric materials”. In: *Fuel Processing Technology* 87.7 (July 2006), pp. 617–622.

[48] Xin Tu, Helen J. Gallon, and J. Christopher Whitehead. “Electrical and spectroscopic diagnostics of a single-stage plasma-catalysis system: Effect of packing with TiO2”. In: *Journal of Physics D: Applied Physics* 44.48 (Dec. 2011).

[49] Richard Van Lent et al. “Site-specific reactivity of molecules with surface defects—the case of H 2 dissociation on Pt”. In: *Science* 363.6423 (Jan. 2019), pp. 155–157. URL: `http://science.sciencemag.org/`.

[50] L. B.F. Juurlink et al. “Eigenstate-resolved studies of gas-surface reactivity: CH4(ν3) Dissociation on Ni(100)”. In: *Physical Review Letters* 83.4 (Jan. 1999), pp. 868–871. URL: `https://journals.aps.org/prl/abstract/10.1103/PhysRevLett.83.868`.

[51] Jiamei Quan et al. “Vibration-driven reaction of CO2 on Cu surfaces via Eley–Rideal-type mechanism”. In: *Nature Chemistry* 11.8 (Aug. 2019), pp. 722–729. URL: `https://www.nature.com/articles/s41557-019-0282-1`.

[52] Marco Sacchi, David J. Wales, and Stephen J. Jenkins. “Mode-specificity and transition state-specific energy redistribution in the chemisorption of CH4 on Ni{100}”. In: *Physical Chemistry Chemical Physics* 14.45 (Dec. 2012), pp. 15879–15887. URL: `www.rsc.org/pccp`.

[53] M. Sacchi, D. J. Wales, and S. J. Jenkins. “Mode-specific chemisorption of CH4 on Pt{110}-(1 × 2) explored by first-principles molecular dynamics”. In: *Journal of Physical Chemistry C* 115.44 (Nov. 2011), pp. 21832–21842. URL: `https://pubs.acs.org/sharingguidelines`.

[54] F. Fleming Crim. “Chemical dynamics of vibrationally excited molecules: Controlling reactions in gases and on surfaces”. In: *Proceedings of the National Academy of Sciences of the United States of America* 105.35 (Sept. 2008), pp. 12654–12661.

[55] M. Sacchi, D. J. Wales, and S. J. Jenkins. “Bond-selective energy redistribution in the chemisorption of CH 3D and CD 3H on Pt{110}-(1×2): A first-principles molecular dynamics study”. In: *Computational and Theoretical Chemistry* 990 (June 2012), pp. 144–151.

[56] A. C. Luntz. “Simple model for associative desorption and dissociative chemisorption”. In: *Journal of Chemical Physics* 113.16 (Oct. 2000), pp. 6901–6905. URL: `http://aip.scitation.org/doi/10.1063/1.1311280`.

[57] Hsin Liang Chen et al. *Review of plasma catalysis on hydrocarbon reforming for hydrogen production-Interaction, integration, and prospects.* Dec. 2008.

[58] E. Schrödinger. “Quantisierung als Eigenwertproblem”. In: *Annalen der Physik* 384.4 (Jan. 1926), pp. 361–376.

[59] M. Born and R. Oppenheimer. “Zur Quantentheorie der Molekeln”. In: *Annalen der Physik* 389.20 (Jan. 1927), pp. 457–484.

[60] Feliciano Giustino. *Materials modelling using density functional theory: properties and predictions.* Oxford University Press, 2014.

[61] V. Fock. “Näherungsmethode zur Lösung des quantenmechanischen Mehrkörperproblems”. In: *Zeitschrift für Physik* 61.1-2 (Jan. 1930), pp. 126–148.

[62] D. R. Hartree. “The Wave Mechanics of an Atom with a Non-Coulomb Central Field Part I Theory and Methods”. In: *Mathematical Proceedings of the Cambridge Philosophical Society* 24.1 (1928), pp. 89–110.

[63] J. C. Slater. “A simplification of the Hartree-Fock method”. In: *Physical Review* 81.3 (Feb. 1951), pp. 385–390. URL: `https://journals.aps.org/pr/abstract/10.1103/PhysRev.81.385`.

[64] David S. Sholl and Janice A. Steckel. *Density Functional Theory.* Hoboken, NJ, USA: John Wiley & Sons, Inc., Mar. 2009, pp. 1–238. URL: `http://doi.wiley.com/10.1002/9780470447710`.

[65] P. Hohenberg and W. Kohn. “Inhomogeneous electron gas”. In: *Physical Review* 136.3B (Nov. 1964), B864. URL: `https://journals.aps.org/pr/abstract/10.1103/PhysRev.136.B864`.

[66] W. Kohn and L. J. Sham. “Self-consistent equations including exchange and correlation effects”. In: *Physical Review* 140.4A (Nov. 1965), A1133. URL: `https://journals.aps.org/pr/abstract/10.1103/PhysRev.140.A1133`.

[67] Stefan Grimme. “Semiempirical GGA-type density functional constructed with a long-range dispersion correction”. In: *Journal of Computational Chemistry* 27.15 (Nov. 2006), pp. 1787–1799.

[68] Stefan Grimme et al. “A consistent and accurate ab initio parametrization of density functional dispersion correction (DFT-D) for the 94 elements H-Pu”. In: *Journal of Chemical Physics* 132.15 (Apr. 2010).

[69] Stefan Grimme, Stephan Ehrlich, and Lars Goerigk. “Effect of the damping function in dispersion corrected density functional theory”. In: *Journal of Computational Chemistry* 32.7 (May 2011), pp. 1456–1465.

[70] A. D. Becke. “Density-functional exchange-energy approximation with correct asymptotic behavior”. In: *Physical Review A* 38.6 (Sept. 1988), pp. 3098–3100. URL: `https://journals.aps.org/pra/abstract/10.1103/PhysRevA.38.3098`.

[71] Chengteh Lee, Weitao Yang, and Robert G. Parr. “Development of the Colle-Salvetti correlation-energy formula into a functional of the electron density”. In: *Physical Review B* 37.2 (Jan. 1988), pp. 785–789. URL: `https://journals.aps.org/prb/abstract/10.1103/PhysRevB.37.785`.

[72] Kieron Burke, John P. Perdew, and Yue Wang. “Derivation of a Generalized Gradient Approximation: The PW91 Density Functional”. In: *Electronic Density Functional Theory*. Springer US, 1998, pp. 81–111. URL: `https://link.springer.com/chapter/10.1007/978-1-4899-0316-7_7`.

[73] John P. Perdew, Kieron Burke, and Matthias Ernzerhof. “Generalized Gradient Approximation Made Simple”. In: *Physical Review Letters* 77.18 (Oct. 1996), pp. 3865–3868. URL: `https://link.aps.org/doi/10.1103/PhysRevLett.77.3865`.

[74] B. Hammer, L. B. Hansen, and J. K. Nørskov. “Improved adsorption energetics within density-functional theory using revised Perdew-Burke-Ernzerhof functionals”. In: *Physical Review B - Condensed Matter and Materials Physics* 59.11 (Mar. 1999), pp. 7413–7421.

[75] John P. Perdew et al. “Restoring the density-gradient expansion for exchange in solids and surfaces”. In: *Physical Review Letters* 100.13 (Apr. 2008), p. 136406. URL: `https://journals.aps.org/prl/abstract/10.1103/PhysRevLett.100.136406`.

[76] H Hellmann. “Einführung in die Quantenchemie”. In: *Leipzig: Franz Deuticke. p. 285. OL 21481721M* (1937).

[77] R. P. Feynman. “Forces in molecules”. In: *Physical Review* 56.4 (Aug. 1939), pp. 340–343. URL: `https://journals.aps.org/pr/abstract/10.1103/PhysRev.56.340`.

[78] P. Pulay. “Ab initio calculation of force constants and equilibrium geometries in polyatomic molecules”. In: *Molecular Physics* 17.2 (1969), pp. 197–204. URL: `https://www.tandfonline.com/doi/abs/10.1080/00268976900100941`.

[79] Zijing Lin. “Pulay forces in density functional theory for periodic and molecular systems”. In: *Physics Letters, Section A: General, Atomic and Solid State Physics* 299.4 (July 2002), pp. 413–417.

[80] Felix Bloch. “Über die Quantenmechanik der Elektronen in Kristallgittern”. In: *Zeitschrift für Physik* 52.7-8 (July 1929), pp. 555–600. URL: `https://link.springer.com/article/10.1007/BF01339455`.

[81] M. C. Payne et al. “Iterative minimization techniques for ab initio total-energy calculations: Molecular dynamics and conjugate gradients”. In: *Reviews of Modern Physics* 64.4 (Oct. 1992), pp. 1045–1097. URL: `https://journals.aps.org/rmp/abstract/10.1103/RevModPhys.64.1045`.

[82] HANNES JÓNSSON, GREG MILLS, and KARSTEN W. JACOBSEN. “Nudged elastic band method for finding minimum energy paths of transitions”. In: World Scientific Pub Co Pte Lt, June 1998, pp. 385–404.

[83] Graeme Henkelman, Blas P. Uberuaga, and Hannes Jónsson. "Climbing image nudged elastic band method for finding saddle points and minimum energy paths". In: *Journal of Chemical Physics* 113.22 (Dec. 2000), pp. 9901–9904. URL: `http://aip.scitation.org/doi/10.1063/1.1329672`.

[84] Henkelman. *Nudged Elastic Band (NEB) method - Date Accessed: 2020-10-12*. URL: `https://theory.cm.utexas.edu/henkelman/research/saddle/`.

[85] Kristof M. Bal et al. "Effect of plasma-induced surface charging on catalytic processes: application to CO2 activation". In: *Plasma Sources Sci. Technol.* 27.2 (Feb. 2018), p. 24001.

[86] Glenn J Martyna and Mark E Tuckerman. "A reciprocal space based method for treating long range interactions in ab initio and force-field-based calculations in clusters". In: *The Journal of Chemical Physics* 110.6 (Jan. 1999), pp. 2810–2821. URL: `https://doi.org/10.1063/1.477923`.

[87] Kristof M. Bal and Erik C. Neyts. "Modelling molecular adsorption on charged or polarized surfaces: A critical flaw in common approaches". In: *Physical Chemistry Chemical Physics* 20.13 (2018), pp. 8456–8459.

[88] Mohammad Hossein Bani-Hashemian et al. "A generalized Poisson solver for first-principles device simulations". In: *The Journal of Chemical Physics* 144.4 (Jan. 2016), p. 044113. URL: `http://aip.scitation.org/doi/10.1063/1.4940796`.

[89] Amin Jafarzadeh et al. "Activation of CO2 on Copper Surfaces: The Synergy between Electric Field, Surface Morphology, and Excess Electrons". In: *Journal of Physical Chemistry C* 124.12 (Mar. 2020), pp. 6747–6755.

[90] J Nørskov. "Electronic factors in catalysis". In: *Prog. Surf. Sci.* 38 (1991), p. 103.

[91] F Holzer, U Roland, and F.-D. Kopinke. "Combination of non-thermal plasma and heterogeneous catalysis for oxidation of volatile organic compounds: Part 1. Accessibility of the intra-particle volume". In: *Appl. Catal., B* 38 (2002), p. 163.

[92] J V Durme et al. “Efficient toluene abatement in indoor air by a plasma catalytic hybrid system”. In: *Appl. Catal., B* 74 (2007), p. 161.

[93] M Shirazi, A Bogaerts, and E C Neyts. “A DFT study of H-dissolution into the bulk of a crystalline Ni(111) surface: a chemical identifier for the reaction kinetics”. In: *Phys. Chem. Chem. Phys.* 19 (2017), p. 19150.

[94] Mahdi Shirazi, Erik C. Neyts, and Annemie Bogaerts. “DFT study of Ni-catalyzed plasma dry reforming of methane”. In: *Applied Catalysis B: Environmental* 205 (2017), pp. 605–614.

[95] H.-Y. T Chen, S Tosoni, and G Pacchioni. “Adsorption of Ruthenium Atoms and Clusters on Anatase TiO2 and Tetragonal ZrO2(101) Surfaces: A Comparative DFT Study”. In: *J. Phys. Chem. C* 119 (2015), p. 10856.

[96] A R Puigdollers, P Schlexer, and G Pacchioni. “Gold and Silver Clusters on TiO2 and ZrO2 (101) Surfaces: Role of Dispersion Forces”. In: *J. Phys. Chem. C* 119 (2015), p. 15381.

[97] S Tosoni, H.-Y. T Chen, and G Pacchioni. “A DFT study of Ni clusters deposition on titania and zirconia (101) surfaces”. In: *Surf. Sci.* 646 (2016), p. 230.

[98] C Liu et al. “Carbon Dioxide Conversion to Methanol over Size-Selected Cu4 Clusters at Low Pressures”. In: *J. Am. Chem. Soc.* 137 (2015), p. 8676.

[99] Z Fuzhen et al. “Atomic Layer Deposition of Ni on Cu Nanoparticles for Methanol Synthesis from CO2 Hydrogenation”. In: *ChemCatChem* 9 (2017), p. 3772.

[100] U Diebold et al. “One step towards bridging the materials gap: surface studies of TiO2 anatase”. In: *Catal. Today* 85 (2003), p. 93.

[101] Y.-F. Li and A Selloni. “Theoretical Study of Interfacial Electron Transfer from Reduced Anatase TiO2(101) to Adsorbed O2”. In: *J. Am. Chem. Soc.* 135 (2013), p. 9195.

[102] Joost Vandevondele et al. “Quickstep: Fast and accurate density functional calculations using a mixed Gaussian and plane waves approach”. In: *Computer Physics Communications* 167.2 (Apr. 2005), pp. 103–128.

[103] Jürg Hutter et al. "cp2k: atomistic simulations of condensed matter systems". In: *Wiley Interdisciplinary Reviews: Computational Molecular Science* 4.1 (Jan. 2014), pp. 15–25. URL: `https://doi.org/10.1002/wcms.1159`.

[104] Joost VandeVondele and Jürg Hutter. "Gaussian basis sets for accurate calculations on molecular systems in gas and condensed phases". In: *Journal of Chemical Physics* 127.11 (2007).

[105] S. Goedecker, M. Teter, and J. Hutter. "Separable dual-space Gaussian pseudopotentials". In: *Physical Review B* 54.3 (July 1996), pp. 1703–1710. URL: `https://link.aps.org/doi/10.1103/PhysRevB.54.1703`.

[106] M Krack. "Pseudopotentials for H to Kr optimized for gradient-corrected exchange-correlation functionals". In: *Theor Chem Acc* 114 (2005), pp. 145–152.

[107] Patrick Bultinck et al. "Critical analysis and extension of the Hirshfeld atoms in molecules." In: *The Journal of chemical physics* 126.14 (Apr. 2007), p. 144111. URL: `http://www.ncbi.nlm.nih.gov/pubmed/17444705`.

[108] C J Howard, T M Sabine, and F Dickson. "Structural and thermal parameters for rutile and anatase". In: *Acta Crystallogr., Sect. B: Struct. Sci.* 47 (1991), p. 462.

[109] V I Anisimov, J Zaanen, and O K Andersen. "Band theory and Mott insulators: Hubbard U instead of Stoner I". In: *Phys. Rev. B* 44 (1991), p. 943.

[110] S L Dudarev et al. "Electron-energy-loss spectra and the structural stability of nickel oxide: An LSDA + U study". In: *Phys. Rev. B* 57 (1998), p. 1505.

[111] Benjamin J. Morgan and Graeme W. Watson. "A DFT + U description of oxygen vacancies at the TiO2 rutile (1 1 0) surface". In: *Surface Science* 601.21 (Nov. 2007), pp. 5034–5041.

[112] Carmen J. Calzado, Norge Cruz Hernández, and Javier Fdez Sanz. “Effect of on-site Coulomb repulsion term U on the band-gap states of the reduced rutile (110) Ti O2 surface”. In: *Physical Review B - Condensed Matter and Materials Physics* 77.4 (Jan. 2008), p. 045118.

[113] N. Aaron Deskins, Roger Rousseau, and Michel Dupuis. “Defining the role of excess electrons in the surface chemistry of TiO 2”. In: *Journal of Physical Chemistry C* 114.13 (Apr. 2010), pp. 5891–5897. URL: `https://pubs.acs.org/sharingguidelines`.

[114] Konstanze R. Hahn et al. “Functionalization of CeO2(1 1 1) by Deposition of Small Ni Clusters: Effects on CO2 Adsorption and O Vacancy Formation”. In: *ChemCatChem* 7.4 (Feb. 2015), pp. 625–634. URL: `http://doi.wiley.com/10.1002/cctc.201402906`.

[115] S K Iyemperumal and N A Deskins. “Activation of CO2 by supported Cu clusters”. In: *Phys. Chem. Chem. Phys.* 19 (2017), p. 28788.

[116] F J J Peeters, R F Rumphorst, and M C M van de Sanden. “Dielectric barrier discharges revisited: the case for mobile surface charge”. In: *Plasma Sources Science and Technology* 25.3 (May 2016), 03LT03.

[117] Q.-Z. Zhang, W.-Z. Wang, and A Bogaerts. “Importance of surface charging during plasma streamer propagation in catalyst pores”. In: *Plasma Sources Sci. Technol.* 27 (2018), p. 65009.

[118] D C Sorescu, W A Al-Saidi, and K D Jordan. “CO2 adsorption on TiO2(101) anatase: A dispersion-corrected density functional theory study”. In: *J. Chem. Phys.* 135 (2011), p. 124701.

[119] N A Deskins et al. “Photocatalytic CO2 reduction by highly dispersed Cu sites on TiO2”. In: *J. Photonics Energy* 7 (2016), p. 12004.

[120] S Huygh, A Bogaerts, and E C Neyts. “How Oxygen Vacancies Activate CO2 Dissociation on TiO2 Anatase (001)”. In: *J. Phys. Chem. C* 120 (2016), p. 21659.

[121] Jeffrey Heyes, Marco Dunwell, and Bingjun Xu. “CO2 Reduction on Cu at Low Overpotentials with Surface-Enhanced in Situ Spectroscopy”. In: *Journal of Physical Chemistry C* 120.31 (Aug. 2016), pp. 17334–17341. URL: `https://pubs.acs.org/sharingguidelines`.

[122] Meredith Fields et al. “Role of Subsurface Oxygen on Cu Surfaces for CO2 Electrochemical Reduction”. In: *Journal of Physical Chemistry C* 122.28 (July 2018), pp. 16209–16215. URL: `https://pubs.acs.org/sharingguidelines`.

[123] Aya K. Buckley et al. “Electrocatalysis at organic-metal interfaces: Identification of structure-reactivity relationships for CO2 reduction at modified cu surfaces”. In: *Journal of the American Chemical Society* 141.18 (Mar. 2019), pp. 7355–7364. URL: `https://pubs.acs.org/sharingguidelines`.

[124] Zhonglong Zhao et al. “Generalized Surface Coordination Number as an Activity Descriptor for CO2 Reduction on Cu Surfaces”. In: *Journal of Physical Chemistry C* 120.49 (Dec. 2016), pp. 28125–28130. URL: `https://pubs.acs.org/sharingguidelines`.

[125] Irina V Chernyshova, Ponisseril Somasundaran, and Sathish Ponnurangam. “On the origin of the elusive first intermediate of CO2 electroreduction.” In: *Proceedings of the National Academy of Sciences of the United States of America* 115.40 (Oct. 2018), E9261–E9270.

[126] Alejandro J Garza, Alexis T Bell, and Martin Head-Gordon. “Is Subsurface Oxygen Necessary for the Electrochemical Reduction of CO2 on Copper?” In: *The Journal of Physical Chemistry Letters* 9.3 (Feb. 2018), pp. 601–606. URL: `https://doi.org/10.1021/acs.jpclett.7b03180`.

[127] Fanglin Che et al. “Elucidating the Roles of Electric Fields in Catalysis: A Perspective”. In: *ACS Catalysis* 8.6 (June 2018), pp. 5153–5174. URL: `https://doi.org/10.1021/acscatal.7b02899`.

[128] H. J. Kreuzer. “Physics and chemistry in high electric fields”. In: *Surface and Interface Analysis* 36.56 (May 2004), pp. 372–379. URL: `http://doi.wiley.com/10.1002/sia.1895`.

[129] Stephan N. Steinmann and Philippe Sautet. “Assessing a First-Principles Model of an Electrochemical Interface by Comparison with Experiment”. In: *The Journal of Physical Chemistry C* 120.10 (Mar. 2016), pp. 5619–5623. URL: `https://pubs.acs.org/doi/10.1021/acs.jpcc.6b01938`.

[130] Joseph A. Gauthier et al. “Challenges in Modeling Electrochemical Reaction Energetics with Polarizable Continuum Models”. In: *ACS Catalysis* 9.2 (Feb. 2019), pp. 920–931. URL: `https://pubs.acs.org/doi/10.1021/acscatal.8b02793`.

[131] Annemie Bogaerts et al. “Burning questions of plasma catalysis: Answers by modeling”. In: *Catalysis Today* (2019).

[132] A. Jafarzadeh et al. “CO2 Activation on TiO2-Supported Cu5 and Ni5 Nanoclusters: Effect of Plasma-Induced Surface Charging”. In: *The Journal of Physical Chemistry C* 123.11 (Feb. 2019), pp. 6516–6525.

[133] Catherine F. Smura et al. “High-Spin cobalt(II) ions in square planar coordination: Structures and magnetism of the oxysulfides Sr2CoO2Cu2S 2 and Ba2CoO2Cu2S2 and their solid solution”. In: *Journal of the American Chemical Society* 133.8 (Mar. 2011), pp. 2691–2705.

[134] Hendrik J. Monkhorst and James D. Pack. “Special points for Brillouin-zone integrations”. In: *Physical Review B* 13.12 (1976), pp. 5188–5192.

[135] P Deshlahra, E E Wolf, and W F Schneider. “A Periodic Density Functional Theory Analysis of CO Chemisorption on Pt(111) in the Presence of Uniform Electric Fields”. In: *The Journal of Physical Chemistry A* 113.16 (Apr. 2009), pp. 4125–4133. URL: `https://doi.org/10.1021/jp810518x`.

[136] Richard G. Forbes. “Field evaporation theory: a review of basic ideas”. In: *Applied Surface Science* 87-88.C (Mar. 1995), pp. 1–11.

[137] C. G. Sánchez, A. Y. Lozovoi, and A. Alavi. “Field-evaporation from first-principles”. In: *Molecular Physics* 102.9-10 (May 2004), pp. 1045–1055.

[138] Fahdzi Muttaqien et al. “Dissociative adsorption of CO2 on flat, stepped, and kinked Cu surfaces”. In: *The Journal of Chemical Physics* 141.3 (July 2014), p. 34702. URL: `https://doi.org/10.1063/1.4887362`.

[139] Nakamura et al. “Does CO 2 dissociatively adsorb on Cu surfaces ?” In: *J of Phys, condensed matter* 100 (1989).

[140] Lihui Ou. “Chemical and electrochemical hydrogenation of CO2 to hydrocarbons on Cu single crystal surfaces: insights into the mechanism and selectivity from DFT calculations”. In: *RSC Advances* 5.71 (2015), pp. 57361–57371. URL: `http://dx.doi.org/10.1039/C5RA09294A`.

[141] Kristof M. Bal and Erik C. Neyts. “Overcoming Old Scaling Relations and Establishing New Correlations in Catalytic Surface Chemistry: Combined Effect of Charging and Doping”. In: *Journal of Physical Chemistry C* 123.10 (Mar. 2019), pp. 6141–6147.

[142] Konrad Koszinowski, Detlef Schröder, and Helmut Schwarz. “Probing cooperative effects in bimetallic clusters: Indications of C-N coupling of CH4 and NH3 mediated by the cluster ion PtAu+ in the gas phase”. In: *Journal of the American Chemical Society* 125.13 (Apr. 2003), pp. 3676–3677. URL: `https://pubs.acs.org/doi/abs/10.1021/ja029791q`.

[143] A. S. Bodke, D. A. Olschki, and L. D. Schmidt. “Hydrogen addition to the Andrussow process for HCN synthesis”. In: *Applied Catalysis A: General* 201.1 (June 2000), pp. 13–22.

[144] V. A. Kondratenko. “Mechanistic analysis of oxygen-assisted coupling of methane and ammonia to hydrogen cyanide over polycrystalline Pt and Rh”. In: *Catalysis Science and Technology* 5.3 (Mar. 2015), pp. 1598–1605.

[145] Massimiliano Aschi et al. “A gas phase model for the Pt+-catalyzed coupling of methane and ammonia”. In: *Angewandte Chemie - International Edition* 37.6 (Apr. 1998), pp. 829–832. URL: `ht`.

[146] R Zhou et al. “Synergistic Effect of Atmospheric-pressure Plasma and TiO2 Photocatalysis on Inactivation of Escherichia coli Cells in Aqueous Media”. In: *Sci. Rep.* 6 (2016), p. 39552.

[147] Eldad Herceg and Michael Trenary. “Formation of Surface CN from the Coupling of C and N Atoms on Pt(111)”. In: *Journal of the American Chemical Society* 125.51 (Dec. 2003), pp. 15758–15759. URL: `https://pubs.acs.org/doi/abs/10.1021/ja037612e`.

[148] Martin Diefenbach et al. “HCN synthesis from methane and ammonia: Mechanisms of Pt+-mediated C-N coupling”. In: *Journal of the American Chemical Society* 121.45 (Nov. 1999), pp. 10614–10625. URL: `https://pubs.acs.org/doi/abs/10.1021/ja992642w`.

[149] Shaojun Xu et al. “Sustaining metal–organic frameworks for water–gas shift catalysis by non-thermal plasma”. In: *Nature Catalysis* 2.2 (Feb.

2019), pp. 142–148. URL: https://www.nature.com/articles/s41929-018-0206-2.

[150] Prateek Mehta et al. “Overcoming ammonia synthesis scaling relations with plasma-enabled catalysis”. In: *Nature Catalysis* 1.4 (Apr. 2018), pp. 269–275. URL: https://www.nature.com/articles/s41929-018-0045-1.

[151] Zhifang Guo et al. “Pt/TS-1 Catalyst Promoted C-N Coupling Reaction in CH4-NH3 Plasma for HCN Synthesis at Low Temperature”. In: *ACS Catalysis* 8.11 (Nov. 2018), pp. 10219–10224. URL: https://pubs.acs.org/doi/abs/10.1021/acscatal.8b02950.

[152] Gerhard Ertl. “Reactions at Surfaces: From Atoms to Complexity (Nobel Lecture)”. In: *Angewandte Chemie International Edition* 47.19 (Apr. 2008), pp. 3524–3535. URL: http://doi.wiley.com/10.1002/anie.200800480.

[153] R C et al. Woods. “Microwave spectroscopy of molecular ions in the laboratory and in space”. In: *Philosophical Transactions of the Royal Society of London. Series A, Mathematical and Physical Sciences* 324.1578 (Jan. 1988), pp. 141–146. URL: https://royalsocietypublishing.org/doi/10.1098/rsta.1988.0007.

[154] Lu T Xu and Thom H Dunning. “Variations in the Nature of Triple Bonds: The N 2 , HCN, and HC 2 H Series”. In: (2016). URL: https://pubs.acs.org/sharingguidelines.

[155] Pierre André Maitre, Matthew S. Bieniek, and Panagiotis N. Kechagiopoulos. *Plasma-enhanced catalysis for the upgrading of methane: A review of modelling and simulation methods.* May 2020.

[156] Tomàš Kozàk and Annemie Bogaerts. “Splitting of CO2 by vibrational excitation in non-equilibrium plasmas: A reaction kinetics model”. In: *Plasma Sources Science and Technology* 23.4 (June 2014), p. 045004. URL: https://iopscience.iop.org/article/10.1088/0963-0252/23/4/045004.

[157] Kevin van ’t Veer et al. “Plasma-Catalytic Ammonia Synthesis in a DBD Plasma: Role of the Micro-Discharges and Their Afterglows”. In: *The*

Journal of Physical Chemistry C (Sept. 2020). URL: `https://pubs.acs.org/doi/abs/10.1021/acs.jpcc.0c05110`.

[158] Denis J. Evans and Brad Lee Holian. "The Nose-Hoover thermostat". In: *The Journal of Chemical Physics* 83.8 (Oct. 1985), pp. 4069–4074. URL: `http://aip.scitation.org/doi/10.1063/1.449071`.

[159] William G. Hoover. "Canonical dynamics: Equilibrium phase-space distributions". In: *Physical Review A* 31.3 (Mar. 1985), pp. 1695–1697. URL: `https://journals.aps.org/pra/abstract/10.1103/PhysRevA.31.1695`.

[160] Shuichi Nosé. "A unified formulation of the constant temperature molecular dynamics methods". In: *The Journal of Chemical Physics* 81.1 (July 1984), pp. 511–519. URL: `http://aip.scitation.org/doi/10.1063/1.447334`.

[161] Shüichi Nosé. "A molecular dynamics method for simulations in the canonical ensemble". In: *Molecular Physics* 52.2 (1984), pp. 255–268. URL: `https://www.tandfonline.com/doi/abs/10.1080/00268978400101201`.

[162] Riccardo Dettori et al. "Simulating Energy Relaxation in Pump-Probe Vibrational Spectroscopy of Hydrogen-Bonded Liquids". In: *Journal of Chemical Theory and Computation* 13.3 (Mar. 2017), pp. 1284–1292.

[163] Alessandro Laio and Michele Parrinello. "Escaping free-energy minima". In: *Proceedings of the National Academy of Sciences of the United States of America* 99.20 (Oct. 2002), pp. 12562–12566. URL: `www.pnas.orgcgidoi10.1073pnas.202427399`.

[164] Alessandro Laio and Francesco L. Gervasio. "Metadynamics: A method to simulate rare events and reconstruct the free energy in biophysics, chemistry and material science". In: *Reports on Progress in Physics* 71.12 (Dec. 2008), p. 126601. URL: `https://iopscience.iop.org/article/10.1088/0034-4885/71/12/126601`.

[165] Philip M. Morse. "Diatomic molecules according to the wave mechanics. II. Vibrational levels". In: *Physical Review* 34.1 (July 1929), pp. 57–64. URL: `https://journals.aps.org/pr/abstract/10.1103/PhysRev.34.57`.

[166] P. Calaminici et al. "A density functional study of small copper clusters: Cun (n5)". In: *Journal of Chemical Physics* 105.21 (1996), pp. 9546–9556. URL: `https://scite.ai/reports/a-density-functional-study-of-jK1Nvl`.

[167] Zexing Cao et al. "Static polarizabilities of copper cluster monocarbonyls CunCO (n = 2-13) and selectivity of CO adsorption on copper clusters". In: *Journal of Physical Chemistry B* 106.37 (Sept. 2002), pp. 9649–9654. URL: `https://pubs.acs.org/doi/abs/10.1021/jp0258098`.

[168] Mingli Yang and Koblar A. Jackson. "First-principles investigations of the polarizability of small-sized and intermediate-sized copper clusters". In: *Journal of Chemical Physics* 122.18 (May 2005), p. 184317. URL: `http://aip.scitation.org/doi/10.1063/1.1891705`.

[169] Albert Poater et al. "Molecular structure and bonding of copper cluster monocarbonyls Cu nCO (n = 1-9)". In: *Journal of Physical Chemistry B* 110.13 (May 2006), pp. 6526–6536. URL: `https://pubs.acs.org/doi/abs/10.1021/jp054690a`.

[170] K R Hahn et al. "Functionalization of CeO2(111) by Deposition of Small Ni Clusters: Effects on CO2 Adsorption and O Vacancy Formation". In: *ChemCatChem* 7 (2015), p. 625.

[171] M. C. Michelini, R. Pis Diez, and A. H. Jubert. "A density functional study of small nickel clusters". In: *International Journal of Quantum Chemistry* 70.4-5 (Jan. 1998), pp. 693–701. URL: `https://on`.

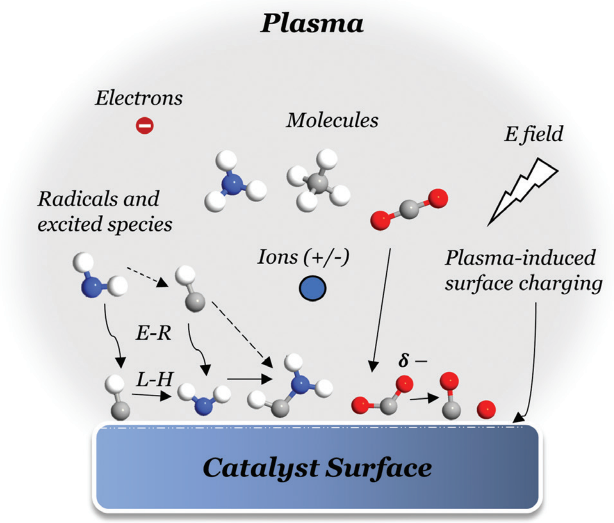

First-Principle Studies of Plasma-Catalyst Interactions for Greenhouse Gas Conversion

Amin Jafarzadeh

The interest in utilizing plasma catalysis for environmental applications continues to grow. In order to maximize the synergistic effects seen in plasma-catalytic experiments, it is crucial to understand the reciprocal interactions between plasma species and catalyst at a fundamental level. Because of the highly complex network of processes happening simultaneously, revealing the entire mechanism is not straightforward, and employing computer simulations, we have to narrow down the complexity of the system by considering each factor separately and obtain detailed information about their effect on the whole reaction network.

In that context, as part of an integrated multi-scale simulation scheme for understanding plasma catalysis, this thesis aims to provide an atomistic description of the plasma-induced changes in the electronic structure of catalysts and reactants that can steer the plasma-catalytic reactions aiming for the conversion of greenhouse gases like CO_2 and CH_4 into value-added chemicals.